Magnetite in Organisms and the Biophysics Underlying Magnetoreception

Stephan Eder

München 2012

Magnetite in Organisms and the Biophysics Underlying Magnetoreception

Stephan Eder

Dissertation
zur Erlangung des Doktorgrades
an der Fakultät für Geowissenschaften der
Ludwig–Maximilians–Universität München

vorgelegt von
Stephan Eder
aus München

München, den 10. Dezember 2012

1. Gutachter: Prof. Dr. Michael Winklhofer
2. Gutachter: Prof. Dr. Hervé Cadiou
Tag der mündlichen Prüfung: 04.02.2013

Zusammenfassung

Magnetit (Fe_3O_4) wird in verschiedenen Organismen durch Biomineralisation gebildet, wobei er unterschiedliche Zwecke erfüllt. Wegen seiner Härte dient er Käferschnecken (Polyplacophora), den Zahnschmelz widerstandsfähiger zu machen (Lowenstam, 1962). Aufgrund seiner ausgezeichneten ferrimagnetischen Eigenschaften eignet sich Magnetit aber vor allem als Substrat für die Wechselwirkung von Zellen mit dem Erdmagnetfeld. Dies kommt besonders eindrucksvoll in der Magnetosomenkette magnetischer Bakterien zum Tragen, die dem Zellkörper ein magnetisches Dipolmoment verleiht und ihn so am Magnetfeld der Erde ausrichtet (Frankel *et al.*, 1979). Dass Magnetit auch eine grundlegende Rolle im magnetischen Sinn von Tieren spielt, ist physikalisch plausibel, biologisch aber noch nicht bewiesen, trotz diverser Hinweise.

Eine Vielzahl von Tieren kann das Magnetfeld der Erde wahrnehmen und daraus Richtungsinformationen für die Orientierung gewinnen, sei es, um über große Distanzen hinweg zu migrieren, sei es, um sich in Umgebungen zurechtfinden, in welchen andere Sinne, wie beispielsweise der visuelle, an ihre Grenzen geraten. Ein magnetischer Orientierungssinn konnte in vielen Spezies aus verschiedenen Phyla nachgewiesen werden, beispielsweise bei Knorpel- und Knochenfische, Amphibien, Vögeln, Säugern und bei Arthropoden (Wiltschko und Wiltschko, 1972; Walker *et al.*, 1984; Němec *et al.*, 2001; Boles und Lohmann, 2003; Begall *et al.*, 2008; Cadiou und McNaughton, 2010; Hart *et al.*, 2012). Eine Zusammenfassung findet sich in Wiltschko und Wiltschko (1995, 2005) wie auch in Lohmann (2010). Es wird auch vermutet, dass Tiere aus der Ortsabhängigkeit der magnetischen Vektorkomponenten (z.B. das Tripel Deklination, Inklination und Totalfeldintensität) Positionsinformationen extrahieren und somit das Erdmagnetfeld gewissermaßen als Navigationssystem benutzen.

Für die Evolution eines Sinnessystems ist es erforderlich, dass der Reiz dauerhaft existiert, und dass es für das Lebewesen von Vorteil ist, den

Reiz wahrzunehmen. Beide Voraussetzungen sind beim Magnetsinn erfüllt: Dank paläomagnetischer Untersuchungen weiß man, dass das Erdmagnetfeld seit dem Archaikum als evolutionsbegleitender Faktor existiert (Tarduno *et al.*, 2010). Gleichzeitig ist es als zuverlässiges Referenzsystem für die Orientierung von großem Nutzen. Selbst während globaler Umpolungen verschwindet das Feld nicht einfach, sondern schwächt sich nur ab und zeigt nach wie vor systematische ortsabhängige Variationen. Da eine Feldumkehr mehrere tausend Jahre benötigt (Leonhardt und Fabian, 2007), bleibt den Tieren genügend Zeit, ihre Migrationskarten an die sich – relativ zum Lebensrhythmus – äußerst langsam verändernden magnetischen Gegebenheiten anzupassen.

40 Jahre nach dem experimentellen Nachweis des magnetischen Orientierungssinnes (Wiltschko und Wiltschko, 1972) ist noch immer wenig bekannt über die zugrundeliegenden biophysikalischen Mechanismen der Magnetfeldaufnahme (Magnetorezeption) und der anschließenden Umwandlung (Transduktion) in einen Nervenreiz. Theoretisch eignet sich hierfür jedes der drei folgenden Substrate: (i) Elektrorezeptoren (Brown und Ilyinsky, 1978; Kalmijn, 1981), (ii) Radikalpaare (Schulten *et al.*, 1978), (iii) biogener Magnetit (Kirschvink und Gould, 1981), welcher im Hauptfokus dieser Arbeit liegt.

Elektrosensitive Organe (i) finden sich in zahlreichen aquatischen Vertebraten, wie z.B. Amphibien, Knorpelfischen, und einigen Knochenfischen wie Welsen (aber nicht in den Lachsfischen, siehe Albert und Crampton, 2005), bei denen Magnetorezeption durch elektromagnetische Induktion prinzipiell möglich wäre, doch noch nicht nachgewiesen wurde. Die Radikal-Paar-Hypothese (ii) geht davon aus, dass eine bestimmte biochemische Reaktion durch ein magnetisch-sensitives Radikal-Paar moduliert wird, daß also das Magnetfeld in Form eines chemischen Signals kodiert wird (siehe Rodgers und Hore, 2009; Schulten *et al.*, 1978; Ritz *et al.*, 2000). Die Magnetit-Hypothese (iii) schließlich geht davon aus, dass das äußere Magnetfeld durch Wecheselwirkung mit einem magnetischen Festkörper eingekoppelt wird und z.B. ein mechanisches Drehmoment oder Verformung erzeugt (Walker *et al.*, 2002; Kirschvink, 1992b). Dies kann im nächsten Schritt durch eine mechanosensitive Struktur in ein neuronales Signal umgewandelt werden. Innerhalb einer Nervenzelle könnte das laut gängigen Modellvorstellungen so realisiert sein, dass ein intrazellulärer magnetischer Einschluss über Zytoskelett-Filamente an die Zellmembran gekoppelt ist, in der mechanosensitive Transmembran-Ionenkanäle enthalten sind. Das magneto-mechanische Moment kann dann über die Filamente

den Ionenfluss durch die Zellmembran steuern. Dadurch ändert sich das elektrische Membranpotential der Zelle, und der magnetische Reiz ist in einen elektrischen Reiz umgewandelt.

Durch elektrophysiologische Techniken (Ableitung der Aktionspotentiale durch eingeführte Elektroden) kann festgestellt werden, ob das neuronale Aktivitiätsmuster mit Magnetfeldänderungen korreliert. Findet man damit einen Nerven, der magnetische Signale leitet, kann man diese zu deren Quelle zurückverfolgen und damit die anatomische Region eingrenzen, in der sich die magnetischen Sinneszellen befinden. Folgende Regionen konnten bereits identifiziert werden: der Schnabel (Heyers *et al.*, 2010) und die Lagena im Innenohr der Brieftaube (Wu und Dickman, 2011, 2012) sowie das olfaktorische Organ der Regenbogenforelle (Walker *et al.*, 1997).

Magnetorezeptorzellen in Lachsfischen:

Mutmaßliche Magnetorezeptoren wurden im olfaktorischen Epithel der Regenbogenforelle *Oncorhynchus mykiss* zwar beschrieben (Walker *et al.*, 1997; Diebel *et al.*, 2000), doch existiert bislang keine einfache Technik, diese reproduzierbar zu identifizieren. Bislang wurde das Epithel eingebettet und Dünnschnitte davon unter dem konfokalen Laserscanning-Mikroskop auf stark reflektierende Objekte hin untersucht. Da nicht klar ist, ob es sich bei diesen Objekten um Magnetit-Kristalle handelt, wurde Energie-dispersive Röntgenanalyse (EDX) zum Nachweis von Eisen benutzt. Da Eisen nicht immer in Form stark magnetischer Verbindungen vorliegen muss, ist der Ansatz nicht überzeugend. In dieser Arbeit stellen wir nun eine Methode vor, mit der es möglich ist, Kandidaten-Magnetorezeptor-Zellen direkt anhand ihres Magnetismus identifizieren:

Zuerst wird das Epithel dissoziiert, bis einzelne Zellen in der Pufferlösung schwimmen. Unter einem Lichtmikroskop wird ein rotierendes Magnetfeld angelegt. Zellen, die einen magnetischen Einschluss in sich tragen, richten sich an dem angelegten Magnetfeld aus und rotieren somit. Anhand der Rotation heben sich die potentiellen Magnetorezeptorzellen von anderen Zellen ab und werden somit eindeutig identifiziert. Des weitern wurde mit dieser Methode das zelluläre magnetische Dipolmoment (μ) gemessen, indem man die kritische Rotationsfrequenz bestimmt, oberhalb derer die Zellen nicht mehr synchron mitrotieren.

Die gefundenen Werte (4 bis 100 fAm^2) sind deutlich größer als zuvor vermutet (0.5 fAm^2). Das magnetische Moment μ wurde zudem in Abhängigkeit von der angelegten Magnetfeldstärke (B)

gemessen, und es stellte sich heraus, dass μ unabhängig von B ist. Das deutet darauf hin, dass magnetische Einbereichsteilchen für den Magnetismus der Zellen verantwortlich sind. Weitere Untersuchungen am Rasterelektronenmikroskop und am konfokalen Lichtmikroskop zeigten, dass sich die magnetischen Kristalle eindeutig innerhalb der Zelle befinden, und so durch Biomineralisation in der Zelle gewachsen sein müssen. Der magnetische Einschluss zeigte am konfokalen Lichtmikroskop einen definierten Kontrast (hell im Reflektions-Modus; und dunkel im Durchlicht-Weitfeld-Modus) von der Größe 1 bis 2 μm. Aus der Größe des Einschlusses und aus den Messungen des magnetischen Moments kann gefolgert werden, dass der magnetische Einschluss aus vielen einzelnen Einbereichsteilchen (typischerweise 50 nm groß) besteht, vermutlich in der Anordnung mehrerer dicht gepackter mehr-läufiger Ketten, ähnlich wie sie im magnetischen Bakterium *Candidatus Magnetobacterium bavaricum* (M.Bav) zu finden sind (Hanzlik *et al.*, 2002). Darüber hinaus zeigte sich der Einschluss mit der Plasmamembran fest verkoppelt, was bedeutet, dass das Drehmoment durch mechanischen Stress unmittelbar auf die Membran übertragen wird, und nicht durch eine Drehbewegung des Einschlusses wie früher angenommen. Aus der direkten Ankopplung und dem starken magnetischen Moment kann gefolgert werden, dass die gefundenen Zellen die biophysikalischen Voraussetzungen für Magnetorezeptor-Zellen erfüllen, mit denen kleine Magnetfeldänderungen hochsensibel und direkt registriert werden können. Das würde auch die Störung des magnetischen Sinns durch Hochspannungsleitungen (50/60Hz) erklären, wie es bei Paarhufern beobachtet wurde (siehe Begall *et al.*, 2008; Burda *et al.*, 2009).

Magnetit in Bakterien:

Der Nachweis von Magnetit in Magnetorezeptorzellen wurde bisher durch indirekte Beweise (anhand nicht-spezifischer Materialeigenschaften von Magnetit) erbracht. Beispielsweise wird angenommen, dass Magnetit (Fe_3O_4) und Greigit (Fe_3S_4) die einzig relativ stark magnetischen Minerale sind, die durch Biomineralistation gebildet werden (Frankel *et al.*, 1979; Farina *et al.*, 1990; Mann *et al.*, 1990; Posfai *et al.*, 1998). Einen direkten Beweis für Magnetit kann man beispielsweise durch Elektronenbeugung im Transmissions-Elektronenmikroskop (TEM) oder Raman-Spektroskopie erbringen. Die Präparation der Probe für TEM-Untersuchungen ist wesentlich aufwendiger als für konfokale Raman-Mikroskopie. Als Modell untersuchten wir magnetotaktische Bakterien aus Binnensee-Sedimenten

(Chiemsee), von denen bekannt ist, dass sie Magnetosomenketten aus Magnetit bestehen, wie z.B. M.Bav.

Ein Problem der Raman-Spektroskopie an Magnetit (Fe_3O_4) ist, dass er sich wegen seiner hohen Lichtabsorption unter dem Laser stark aufheizt und so leicht zu Maghaemit ($\gamma-Fe_2O_3$) und schließlich zu Hämatit ($\alpha-Fe_2O_3$) oxidiert (Faria und Vena, 1997; Shebanova und Lazor, 2003b,a; Hanesch, 2009; Lübbe *et al.*, 2010; Li *et al.*, 2012). Um dies zu verhindern wurde die Laserleistung auf ein Minimum von 0,25mW justiert und im Ausgleich dafür die Integrationszeit erhöht. Mit diesen Einstellungen gelang es, eine klare Signatur der charakteristischen Raman-Linien von Magnetit aus den Bakterien zu extrahieren. Durch Abrastern der Probe und anschließender Wellenzahl-Filterung wurde die Verteilung des Magnetits kartiert. Die Magnetitkarte zeigt eindeutig längliche Strukturen, oder sogar mehrere längliche Strukturen pro Bakterium (M.Bav). Das ist konsistent mit elektronenmikroskopischen Beobachtungen, die bis zu fünf mehr-adrige Magnetosomenketten zeigen (Hanzlik *et al.*, 2002). Obwohl die Magnetosomengröße (ca. 50-100nm) deutlich unter der optischen Auflößungsgrenze liegt, können die Magnetosomenketten hier dargestellt werden. Diese erhöhte Auflösung gegenüber der normalen konfokalen Mikroskopie wird durch wellenlängen-dispersive Aufzeichnung des inelastisch gestreuten Lichtes erreicht. Gleichzeitig hilft die niedrige Laserleistung, sekundäre Streueffekte zu verringern.

In den Spektren der Bakterien lassen sich weitere charakteristische Raman-Linien identifizieren, wie z.B. die von elementarem Schwefel in Form des Allotrops S_8, der auf der Verteilungskarte in Form runder Einschlüsse auftritt. Bislang war nicht bekannt, in welcher Oxidationsstufe und molekularen Struktur EDX-identifizierter Schwefel in M.Bav. vorliegt. Es ist anzunehmen, dass die S_8 Einlagerungen als Nährstoffdepots dienen, da bei der Oxidation von S_8 zu Sulfat Energie gewonnen wird (Spring *et al.*, 1993).

Das gleichzeitige Auftreten von Schwefel und eisenhaltigem, magnetischem Material kann prinzipiell bedeuten, dass der ferrimagnetische Thiospinel Greigit (Fe_3S_4) vorliegt, sowie er auch in magnetischen Bakterien aus anoxischen (sulfidischen) Habitaten auftritt (Farina *et al.*, 1990; Mann *et al.*, 1990). In den hier untersuchten Magnetosomen konnte keine Übereinstimmung mit dem charakteristischen Ramanspektrum eines synthetisch hergestellten Greigits gefunden werden, was die Anwesenheit von Greigit ausschließt. Das Greigit-Spektrum unterscheidet sich signifikant von dem Magnetit-Spektrum und weist oberhalb von 400 cm^{-1} keine

weiteren Linien auf, was aus Literaturdaten (nach unserem Kenntnisstand) nicht hervorgeht.

Des weiteren konnte Raman-spektroskopisch gezeigt werden, dass magnetotaktische Vibrios ihren Phosphor nicht als Pyro- oder Polyphosphat, sondern in Form von Orthophosphat einlagern. Das charakteristische resonante Raman-Signal eines Häm-komplexes (vermutlich von Cytochrom c, einem Elektrontransporter in der Atmungskette), eignet sich gut zur Darstellung des periplasmatischen Raumes zwischen innerer und äusserer Membran.

Die Ergebnisse zeigen, dass die konfokale Raman Spektroskopie eine Methode ist, die nicht-invasiv und durch relativ einfache Präparation und ohne zusätzliche Fluoreszenzmarker die intrazelluläre Verteilung von Molekülen und Kristallen darstellen kann. Speziell wenn die Laserleistung sehr gering eingestellt ist, kann die konfokale Raman Mikroskopie dazu benutzt werden: (i) zelluläre Komponent äußerst selektiv darzustellen, und durch Energiefilterung sogar unterhalb der optischen Auflösungsrenze nachzuweisen; (ii) durch die Autofluoreszenz der Häm-Gruppe in Cytochrom Molekülen die Umrandungen von lebenden prokaryotischen Zellen (wie auch Mitochrondrien in eukaryotischen Zellen) darzustellen, ohne diese durch potentiell toxische Fluoreszenz-Marker zu beeinflussen; (iii) zwischen dem oxidierten und reduzierten Zustand der Häm-Gruppe zu unterscheiden, und so Redoxprozesse der Atmungskette zu titrieren; (iv) intrazelluläre magnetische Minerale zu identifizieren, wobei es sich sogar als sensitivere Methode als EDX am Rasterelektronenmikroskop zeigt. Schließlich ist es vorstellbar, bei der mikrobiellen Klärung von Sulfat-sauren Abwässern durch Raman-Messungen die Bakterienarten zu identifizieren, die einen hohen Anreicherungsgrad von Schwefel aufweisen und so für die Wasserreinigung besonders nützlich sein können.

Der Magnetsinn von Fledermäusen:

Vor kurzem wurde durch Verhaltensexperimente gezeigt, dass Fledermäuse mit Hilfe des Magnetfeldes navigieren (Holland *et al.*, 2010) und dass sie - ähnlich wie Zugvögel - ihren Magnetkompass an der untergehenden Sonne kalibrieren (Muheim *et al.*, 2006a). Dabei wurde eine Gruppe von Fledermäusen einem gedrehten Magnetfeld während der Kalibrierung ihres Kompasses ausgesetzt. Diese Gruppe zeigte nach der Auflassung eine mit der Magnetfeld-Drehung korrelierte Abflugrichtung.

Noch ist unklar, ob der Magnetsinn der Fledermäuse auf Magnetit oder Radikal-Paaren basiert. Der Radikalpaar-Mechanismus kann kurzzeitig durch ein schwaches RF-Magnetfeld (Radio-Frequenz; im MHz-Bereich) deaktiviert werden (Ritz *et al.*, 2009). Um dies zu testen, wurden Fledermäuse während der Kalibrierung des Kompasses einem RF-Feld exponiert, wobei ein neues Protokoll für die doppel-blind Durchführung der Verhaltensexperimente entwickelt wurde. In diesen Experimenten zeigten diese Fledermäuse allerdings keine statistisch signifikante Orientierung, weder in der Kontroll- noch in der Testgruppe. Dies wurde auf die labilen Wetterbedingungen zurückgeführt, welche die Motivation der Tiere beeinflusste. Hier wird deutlich, dass die Motivation ein entscheidender, doch kaum kontrollierbarer Faktor in Verhaltensexperimenten ist.

Ein weiteres Experiment sollte die Kalibrierung des Kompasses an der Sonne testen, ohne dass das Magnetfeld gedreht wurde, also komplementär zu dem ursprünglichen Experiment, bei dem die Tiere während des Sonnenuntergang einem gedrehten Magnetfeld exponiert waren. Mit Hilfe eines Spiegels wurde der Sonnenuntergang in eine andere Himmelsrichtung gedreht, ähnlich wie von Kramer (1953) oder Phillips und Waldvogel (1982) an Zugvögeln getestet. Hier zeigten sowohl Test- als auch Kontrollgruppen jeweils signifikante Orientierung, doch unterschieden sich die mittleren Abflugrichtungen von Test- und Kontrollgruppe nur unwesentlich voneinander. Würde der Kompass der Tiere an der Position der Sonne am Horizont kalibriert, so hätte man bei der benutzen Spiegelanordnung eine Abweichung von 90 Grad erwartet.

Die Experimente warfen unter anderem die Frage auf, ob Fledermäuse die Polarisation des Lichtes wahrnehmen können, was für Säugetiere noch nicht gezeigt werden konnte. Es ist auch möglich, dass die Kunstoffbehälter, von denen die Tiere aus den Sonnenuntergang betrachteten, unnatürliche Polarisationseffekte hervorgerufen haben. Das Material der Gefäßwände zeigte Pleochroismus, bei dem vor-polarisiertes Licht je nach Wellenlänge unterschiedlich absorbiert und re-polarisiert wird. Da das natürliche Polarisationsband am Himmel im Bereich von 90° zur Sonne während des Spiegel-Experiments großzügig abgedeckt war, konnte kein vor-polarisiertes Licht auf die Gefäße treffen und somit auch kein Licht re-polarisieren. Selbst wenn Fledermäuse die Fähigkeit haben, die Polarisation wahrzunehmen, wären beim Spiegel-Experiment kein re-polarisiertes Licht als möglicher Störfaktor aufgetreten.

Magnetorezeption bei Ameisen

Ameisen, insbesondere die migrierende Art *Pachycondyla marginata*, können Magnetfelder wahrnehmen und sich daran orientieren (Acosta-Avalos *et al.*, 2001). Bei der Frage, wie der Magnetorezeptor funktioniert und in welcher Körperregion er sitzt, ist man auf das Johnston's Organ an den Antennen der Ameisen gestoßen (Acosta-Avalos *et al.*, 1999; Wajnberg *et al.*, 2000, 2004). Bislang wurde diesem Organ aufgrund seiner mechanosensitiven Eigenschaften die Funktion eine Gravirezeptors (Schwere-Sensor bzw. Beschleunigungssensor) zugeordnet. Da in dem Organ auch eisenhaltige Partikel gefunden wurden, welche man durch Elektronenbeugung am Transmissionselektronenmikroskop (TEM) punktuell als Magnetit und Maghaemit identifizierte, wurde vorgeschlagen, dass das Organ auch der Magnetorezeption dienen könnte (Oliveira *et al.*, 2010). Allerdings blieb unklar, welche typischen magnetischen Eigenschaften die Einlagerungen in ihrer Gesamtheit haben, insbesondere, ob sie eine Magnetisierung in ausreichender Stärke für die Magnetorezeption erzeugen. Dieser Frage sollte hier mit magnetischer Raseter-Kraftmikroskopie (MFM) an TEM-Schnitten von Oliveira *et al.* (2010) nachgegangen werden.

Die Dünnschnitte zeigten eine unerwartet starke Topographie, welche die Empfindlichkeit der Methode für magnetische Kräfte beeinträchtigt. So konnten keine magnetischen Kräfte identifiziert werden, die eindeutig auf das Vorhandensein Remanenz-tragender Partikel hinweisen würden. In den TEM-Abbildungen erscheinen die Einlagerungen ungeordnet, was darauf hindeuten kann, dass sich die einzelnen magnetischen Momente der potentiell magnetischen Körner gegenseitig aufheben und somit vom MFM nicht detektiert werden. Prinzipiell eignen sich die relativ schweren eisenhaltigen Einlagerungen auch gut dazu, kraft ihrer Masse die Sensibilität eines Schwere-Sensors zu verstärken. Das läßt die Funktion eines Gravirezeptors vorerst plausibler erscheinen.

Contents

1 Introduction

Various organisms are known to biomineralize the magnetic mineral magnetite Fe_3O_4, but use it for different purposes. For example, in the form of finely dispersed crystals in dental cappings of chiton teeth, it serves as a hardening agent (Lowenstam, 1962), while in the form of magnetosome chains in magnetic bacteria, it enables magnetotactic behavior (Frankel *et al.*, 1979). In a number of vertebrate groups, most notably salmonid fish, magnetite has been detected and suggested to form the basis of a magnetic sensory system (Kirschvink *et al.*, 1985b). In fact, a magnetic sense has been demonstrated in a number of animal phyla, including arthropods, teleost fish, amphibians, mammals and birds (Wiltschko and Wiltschko, 1972; Walker *et al.*, 1984; Němec *et al.*, 2001; Boles and Lohmann, 2003; Begall *et al.*, 2008; Cadiou and McNaughton, 2010; Hart *et al.*, 2012). For a review see Wiltschko and Wiltschko (1995, 2005) and Lohmann (2010). The ability to sense the Earth's magnetic field is called magnetoreception and may be used to extract directional information from the Earth's magnetic field for orientation and navigation.

Importantly, the magnetic field has been present since at least 3.5 billion years ago (Tarduno *et al.*, 2010), and therefore a permanent condition under which life has evolved. This fact in combination with the advantage that spatial orientation gives to organisms, are the basic requirements for the evolution of magnetoreception. Even during periods of geomagnetic polarity

reversals, the Earth's magnetic field does not vanish altogether and continues to provide a reference frame for orientation. With a typically duration of a few thousand years (Leonhardt and Fabian, 2007), a global magnetic field reversal is long enough for individuals to slowly adjust to the changing conditions.

The magnetic field provides not only directional, but also positional information and hence can be used for navigation. From a single inclination (I) measurement, the geomagnetic latitude λ_{m} of the current position can be determined using the well known relation $\tan I = 2 \tan \lambda_m$ (see figure 1.1. This is possible because of the essentially dipolar character of the field, producing systematic spatial variations. At other extreme, rather irregular contributions to the field offer useful information as well: On the basis of highly sensitive absolute measurements of total magnetic field intensity, regional or local magnetic anomalies can be detected, which however need to be tied to magnetic anomaly charts to determine the position in geographic space. For navigation it is necessary to know both the current position and the direction of the target position, which requires a mental representation of the magnetic landscape between start and end position. The big question is whether animals have such a mental magnetic map to recognize regions by their characteristic magnetic fingerprints (e.g. Dennis *et al.*, 2007).

In this study we focus on the question how animals are able to sense magnetic field in the first place and how they integrate this information with other cues. Exactly 40 years after magnetoreception was rigorously demonstrated in behavioral experiments on caged migratory songbirds by Wiltschko and Wiltschko (1972), surprisingly little is known about the underlying physical mechanisms and biological pathways. There are three viable hypothesis about the physical mechanism which are (i) based on magnetite in mechanosensitive structures (Kirschvink and Gould, 1981), (ii) based on a radical pair mechanism (Schulten *et al.*, 1978), or (iii) based on induction (Brown and Ilyinsky, 1978; Kalmijn, 1981). It is suggested that candidate sites where magnetoreception could take place are the beak (Beason and Semm, 1996), the nose (Walker *et al.*, 1997), the eye (Phillips and Borland, 1992; Zapka *et al.*, 2009), and the inner ear lagena (Wu and Dickman, 2011, 2012).

In the last 15 years, the problem of magnetoreception has been approached from a number of different directions:

In order to identify candidate sites for magnetoreception, sensory nerves innervating these were severed to stop flow of magnetic information to the brain. For example, Mora *et al.* (2004) showed that pigeons with bilaterally

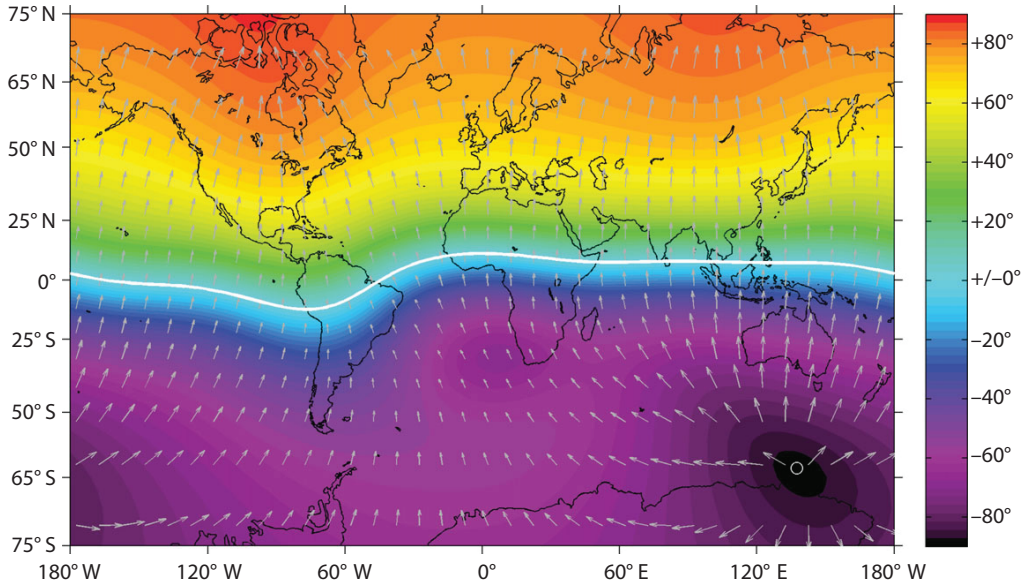

Figure 1.1: from Winklhofer (2010) fig. 1: Earth's magnetic field at the surface of the globe. White arrows show local magnetic North direction, with arrow length being proportional to the total intensity. The color represents the inclination of the field, which varies systematically with geographic latitude. The white line is the magnetic equator, where the inclination is zero. Magnetic North and geographic North direction approximately coincide in most regions. Large scale anomalies occur in the South Atlantic and Northern Siberia.

sectioned ophthalmic branch of the trigeminal nerve were no longer able to discriminate a magnetic anomaly. The same treatment applied to European robins did not affect magnetic compass orientation, while lesion of a light-processing forebrain region (cluster N) did (Zapka *et al.*, 2009).

Particularly interesting insights into magnetoreception were obtained with neuroscience approaches. Electrophysiological techniques were used to record the firing rate of candidate nerves conveying magnetic field information (Walker *et al.*, 1997; Wu and Dickman, 2012). After electrophysiological recording Walker *et al.* (1997) used anterograde fluorescent labeling to trace the neuronal pathway. Neuronal activity mapping through molecular proxies like c-fos or ZENK show enhanced neural activity in specific regions of the brain after magnetic field stimulation (for example Němec *et al.*, 2001; Zapka *et al.*, 2009; Heyers *et al.*, 2010; Wu and Dickman, 2011, 2012).

Studies involving transgenic animals so far have been conducted only in insects (Gegear *et al.*, 2010). The results point to an involvement of the cryptochrome protein in magnetoreception through the radical-pair mechanism, at least in magnetic fields ten times stronger than the natural ambient field.

1.1 Behavioral experiments: Do animals respond to magnetic fields at all?

Before magnetoreception can be studied at the structural level, an animal model is needed that has been shown be capable of sensing the magnetic field in at least two independently conducted studies. The first step therefore are behavioral assays testing for orientational preferences as a function of the applied magnetic field direction, or alternatively, conditioning experiments in which animals learn to discriminate different kinds of magnetic field stimulus by differential reinforcement (e.g. Walker, 1984). Behavioral experiments are taking advantage of a certain natural behavior of the animal under a certain condition. To test for compass orientation, for example, the direction of the magnetic field vector can be changed. If the animal changes its behavior (i.e. its migration direction) in a certain way, as it was predicted for the specific change in condition, then the animal can sense the magnetic field.

While the basic test for compass responses described above captures a natural behavioral component under controlled conditions, conditioning experiments study learned ("artificial") responses of test animals to the magnetic stimuli, such as the presence of a strong magnetic anomaly (Mora *et al.*, 2004). As opposed to compass responses, which can only be studied when the test animal is motivated to perform the desired behavior (e.g., during migration restlessness or *Zugunruhe*), conditioning experiments reinforce or punish certain actions and thus exert control on motivation. These kinds of experiments have been successful on various kinds of fish (Walker, 1984; Shcherbakov *et al.*, 2005; Hellinger and Hoffmann, 2009), but not so in birds. For example, while Mora *et al.* (2004) managed to condition pigeons to stationary local magnetic anomaly, Kishkinev *et al.* (2012) failed to replicate that experiment on European robins.

The geomagnetic field and its spatial variations are not the only useful cues for orientation and navigation. Depending on the situation, other cues (visual, olfactory, gustatory, thermal, auditory, humidity, barometric) may

be more important. For example the polarization pattern of skylight has been suggested to be important for migratory songbirds when calibrating their magnetic compass (Muheim *et al.*, 2006a), as is the direction of the setting sun in night migratory songbirds (Cochran *et al.*, 2004).

Behavioral experiments should be designed in a way to remove all cues other than the cue being tested (see Wiltschko and Wiltschko, 1972; Quinn and Brannon, 1982), or the cue of interest may be overridden by a cue that has a higher position in the hierarchy of cues. Therefore, each behavioral test must be accompanied by a control experiment which shows that untreated animals in the experimental setup can be expected to behave in a predictable way. It is particularly important to show that only the change in conditions but not the experimental situation itself affects the behavior. Experiments conducted with a rigorous double-blind design are considered most convincing (Kirschvink *et al.*, 2010). Those experiments run by a certain protocol, where the person handling the animals, running the experiment and acquiring the data does not know which treatment the animal has been given. This removes possible biases of unconscious behavior of the persons. If technically feasible, the experiment should run as automated as possible, and with random sampling order in the protocol. We implemented these measures in a field experiment on greater mouse-ear bats (*Myotis myotis*), designed to identify what kind of sunset cue bats may use for calibrating their magnetic compass (see chapter 4).

Our main focus in this study is on the rainbow trout (*Oncorhynchus mykiss*, or formerly *Salmo gairdneri*). In rainbow trout and closely related salmonid species, a magnetic sense has been demonstrated experimentally in a number of independent studies using different techniques (Quinn, 1980; Quinn and Brannon, 1982; Taylor, 1986; Chew and Brown, 1989; Walker *et al.*, 1997; Shcherbakov *et al.*, 2005; Hellinger and Hoffmann, 2009; Phillips and Borland, 1992; Takebe *et al.*, 2012; Hellinger and Hoffmann, 2012).

One of the first behavioral experiment on salmonids was by Quinn and Brannon (1982) who showed on the example of sockeye salmon that salmonids use the magnetic field for orientation. Sockeye salmon smolts, which were just about to leave their natal lake system towards the Pacific Ocean, were caught and placed in an open circular arena with eight exits evenly spaced over the unit circle. The exits dead-ended into buckets. The smolts in the arena had to orient and to make a decision in which direction to swim. At the end of the experiment the number of fish in each bucked were counted. The statistical mean of direction potentially represents the migratory direction of the smolts. The control experiment showed that

the fish decided to travel about 327° to geographic north, which coincides with the direction they would have taken in the wild to leave the lake system through its outlet. In a second experiment, the magnetic field was shifted horizontally by 90° ccw, using a pair of Helmholtz coils. The result was that the mean travel direction did not change significantly (342° to geographic north). Both experiments were repeated with a non-translucent cover over the arena, removing the daylight and blocking visual cues. The results of that experiment now was a bimodal orientation behavior. One mode was statistically indistinguishable from the control direction (341° vs 327°) but the second mode represented the opposite direction (161°). Most significantly, after shifting the field by 90°, the axis of bimodality shifted to 286°/106°. Within statistical confidence levels, the shift in preferential axis corresponds to the shift in field axis, showing that the smolts use the magnetic field for orientation. The bimodal behavior indicates that the magnetic sensor might be bimodal, encoding the axis of the magnetic vector, but not the polarity. Further cues must be involved to distinguish between the direction and anti-direction.

Walker *et al.* (1997) found evidence that the rainbow trout is able to detect a magnetic field anomaly in a conditioning experiment. His trout were trained to go for food at a target when a magnetic field anomaly was switched on. After a few training cycles the fish went to the feeder for food more often when the anomaly was switched on than when it was turned off. This shows that the rainbow trout can sense the magnetic field, and can learn to associate a magnetic anomaly with a food source. This further suggests that if the information can be used for a complex process such as learning, then it can potentially also be used for the process of orientation and navigation.

1.2 Specifically perturbing magnetoreception: Which type of mechanism is involved in magnetic sensing?

There are mainly two different physical hypothesis of how a magnetoreceptor may work, plus one hypothesis for animals that are equipped with highly sensitive electroreceptors. Such electroreceptors theoretically could be used for sensing the field through elecromagnetic induction (Brown and Ilyinsky, 1978; Kalmijn, 1981). The species equipped with electroreception

are mainly of the group of amphibians and mormyrid fish (catfish) (Albert and Crampton, 2005). Since we will focus on animals without electroreception, the following two hypothesis are most viable: (i) The magnetite hypothesis assumes neurons containing magnetite crystals connected to mechanosensitive structures. After the model of Walker *et al.* (2002) and Kirschvink (1992b), the crystals tend to align with the external magnetic field (Earth's magnetic field), and thereby generate torque. The torque tries to rotate the magnetic inclusion which is mechanically linked by cytoskeletal filament structures to mechanically gated ion channels in the plasma membrane of the nerve cell. The torque causes ion-channels to open, ions to exchange through the membrane, and finally produces a signal (for example, a change in the spontaneous firing rate), which can be interpreted by the brain and then used for decisions in behavior or navigation. Magnetite-based magnetoreception can temporally be disabled with a strong magnetic pulse that is short enough to remagnetize magnetite crystals without rotating or moving them (strength 0.5 T, pulselength 0.5 ms; Kirschvink and Kobayashi-Kirschvink, 1991; Walker and Bittermann, 1989).

(ii) The radical-pair hypothesis (see Rodgers and Hore, 2009; Schulten *et al.*, 1978; Ritz *et al.*, 2000, for a review) posits certain biochemical reactions that are sensitive to weak magnetic fields, such as the Earth's magnetic field. Two radicals forming a spin-correlated pair, where each radical has an unpaired electron whose spin is either parallel or anti-parallel with respect to the other unpaired electron of the radical pair. Since each electron-spin has its own magnetic moment, the radical pair reaction can be influenced by magnetic fields. A radical pair can be generated by short-wavelength light in the candidate molecule cryptochrome (Ritz *et al.*, 2000), which has been found to be expressed in great concentrations in retinal ganglion cells of night-migratory songbirds (Mouritsen *et al.*, 2004).

In behavioral experiments we can test for the radical pair magnetoreceptor, using an alternating magnetic field oscillating at the Larmor frequency of the free electron spin (Ritz *et al.*, 2009). This frequency f_{L} is proportional to the total intensity F of the ambient magnetic field, with

$$f_{\mathrm{L}}[\mathrm{MHz}] = 2.8F[\mathrm{Oe}]\,.$$

For a present-day earth strength magnetic field [0.25 to 0.65 Oe], f_{L} ranges between 0.7 and 1.82 MHz, i.e. in the medium frequency radiowave band. The Larmor frequency has a resonance effect on the free electron spin, therefore should perturb magnetoreception based on a radical pair mechanism in which one spin is not coupled to a hyperfine field (Rodgers

and Hore, 2009; Ritz *et al.*, 2004; Thalau *et al.*, 2005, 2006; Cintolesi *et al.*, 2003; Ritz *et al.*, 2010).

Ritz *et al.* (2004, 2009) and Thalau *et al.* (2005, 2006) have shown that migratory birds are magnetically disoriented when exposed to a low-amplitude radiofrequency (RF) magnetic fields in the lower MHz range. These kind of experiments so far have only been conducted in laboratory, but not in the field. Here we designed low-power consumption RF equipment suitable for experiments in the field to study magnetic orientation behavior in bats exposed to RF magnetic fields (see chapter 4.3)

1.3 Magnetoreception-organ: Where is the magnetoreceptor located?

Once an animal has shown sensitivity to magnetic fields, there must be a signal generated in some magnetoreceptor cells, and there must be one or several nerves associated with these cells, that carry a "magnetic signal" as information to the brain. Such a signal can be detected with electrophysiological recording techniques. An electrode is inserted into the corresponding neuronal branch in the living animal. If there is a change in firing rate upon magnetic field stimulation, the nerve carrying this information must be connected with the magnetoreceptor cells, either directly or at a higher order. With this type of experiment the signal can be systematically traced back into the sensory region where the signal originated. This is the most promising technique to find the tissue in which the magnetoreceptor cells are located. For our model animal, the trout, electrophysiological experiments have been successfully conducted by Walker *et al.* (1997). In the rosV branch of the trigeminal nerve [1] they identified some units whose firing rate changed in response to a magnetic field change, and traced the responding units back to the olfactory organ.

The olfactory organ is formed as a rosette consisting of a dozen or so lamellae, which is an arrangement of maximized surface in contact with water percolating through the nostrils (figure 1.2). It is located within a bony pit at the skull, and is covered by skin, in which are two valve like holes. Through one of them fresh water can flow in, the other valve is to release the water. The smell can be sensed by the olfactory neurons located at the surface of the lamellae. The I. cranial nerve, which transmits the olfactory

[1] rosV = ramus opthalmicus superficialis of the Vth brain nerve.

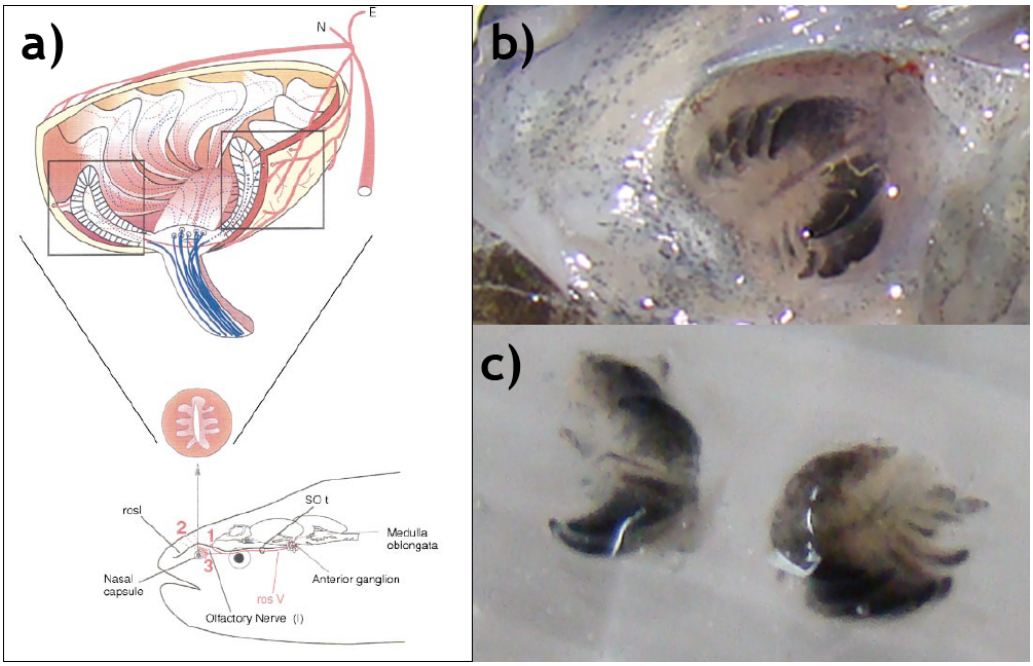

Figure 1.2: (a) adapted from Walker *et al.* (1997). Lower: schematic view of a rainbow trout head with its neuronal anatomy. The nerve carrying the "magnetic" signal is labeled as "rosV". Top: the schematic view of an olfactory rosette. Note that the "rosV" is innervating laterally. (b) Photograph of an olfactory rosette of rainbow trout sitting in a pit at the forehead (skin removed). (c) Dissected olfactory rosettes of the same trout immersed in a buffer solution.

information, exits the rosette at the bottom towards the olfactory bulb, located at the front of the brain. The olfactory neurons have their axons connected to the bulb, and the entity of these axons makes up the olfactory nerve (nerve I). However, the nerve carrying the "magnetic information" innervates the olfactory rosette laterally. These nerves do not link to the olfactory bulb but via the rosV branch of the trigeminal nerve directly to the brain (Walker *et al.*, 1997).

Using DiI, a lipophilic fluoresecent dye, (which has been placed on the electrophysiological recording site) to trace the neural activity back to its origin, Walker *et al.* (1997) were able to pinpoint the origin of the magnetic response in the tip of a lamella. Further, they reported a cell type in the lamella that is associated with crystalline particles rich in iron (using energy dispersive X-ray analysis) producing a strong contrast feature in confocal light reflectance. In a follow up study, Diebel *et al.* (2000) detected magnetic remanence carried by a few single-domain magnetic

particles (50 nm particle size) associated with a reflective object in a section of an olfactory lamellae. These findings showed that there are candidate magnetoreceptor cells located in the olfactory organ, which we target here in our work. The key questions are:

1. Is it possible to reproducibly find the candidate cells described by Walker *et al.* (1997) and Diebel *et al.* (2000)?

2. How strong is the cellular magnetic moment of the candidate magnetoreceptor cells? In Diebel *et al.* (2000), only one magnetic measurement was reported, which however was not consistent with the size of the observed reflective structures.

3. How is the cellular magnetic moment connected to the plasma membrane of the cell?

The answers to questions (2) and (3) provide important constraints in biophysical models on the possible function of a magnetite-based magnetoreceptor cell.

As opposed to classical senses where receptor cells are concentrated in a distinct sensory epithelium (vision - retina, hearing - organ of Corti, balance - inner ear maculae, smell - olfactory eptihelium), magnetoreceptor cells may be dispersed and found in different tissue (Kirschvink *et al.*, 2010). Magnetite-based magnetoreceptors have been suggested to be also in the inner ear of birds (Wu and Dickman, 2011, 2012), or in the lateral line of fish (Moore *et al.*, 1990). In invertebrates, there are less hints where to search. Recently, a TEM study (Oliveira *et al.*, 2010) on ant antennae found magnetite/maghemite (among hematite and goethite) in the Johnston's organ, which in some insects is involved in hearing and in others in graviception (Sandeman, 1976). Since these iron oxide minerals all have a high density, they may also serve to better the sensitivity of a gravity receptor (Winklhofer and Kirschvink, 2010). Using magnetic-force scans, it should be possible to find out whether or not magnetite/maghemite occur in significant concentrations in the Johnston's organ to mediate a magnetic sensory function. (see chapter 5).

1.4 Structure of magnetoreception sensors: How does a magnetoreception sensor work in particular, and how is it built?

To answer this question we need to face a number of sub-question:

a. Magnetic discrimination: How to identify potential magnetoreceptor

Based on the magnetite theory a magnetoreceptor cell must contain a magnetic object. Most likely for a magnetic material in biological structures are iron based magnetic minerals, magnetite Fe_3O_4 and its oxidized form, maghaemite, ($\gamma-Fe_2O_3$), because these are strongest magnetic of all naturally occurring minerals and are known to occur as biomineralization products in magnetic bacteria (Frankel *et al.*, 1979) and in a number of animals (Lowenstam, 1962; Walcott *et al.*, 1979). Crystalline structures, if larger than half a micron, can be identified at the light microscope, in transmitted light as dark spots, and in reflected light as bright spots. If an object appears in only one of the two techniques, it can also be an artifact i.e. from the lens effect of the curved cell membrane, from other objects from out of focal plane (with wide field microscopes), or from a dark pigment. With this identification test we find non-transparent reflective particles in the tissue or in cells. However, the mere presence of such an object does not automatically imply magnetism. To specifically test for magnetic material we need to show a magnetic force feedback of the particles or cells in question. Therefore we apply a technique that effectively discriminates magnetic cells, by observing the mechanical response of cells to a magnetic field change. Since cells embedded in sensory epithelium are mechanically too strongly blocked to align with an external field, the cells need to be freed from the epithelium and suspended in buffer solution, similar to a unicellular magnetotactic organism (see chapter 2.3.1).

b. Imaging: How is a magnetoreceptor cell built?

To understand how a magnetoreceptor cell is built, imaging with high resolution techniques helps to identify intracellular structures. After showing the magnetic response (chapter 1.4a), one can use reflected and transmitted light to visually identify the magnetic inclusion and its relation to other

cellular structures. Using fluorescent dyes that stain the cell membrane or the nucleus, allows one to identify these structures and, importantly, to prove that this specific magnetically responding object is an (intact) biological cell.

An important criterion is whether the magnetic particles is inside or outside the cell. If it is intracellular, the magnetic particles have been synthesized in a controlled biomineralization process (Kirschvink and Hagadorn, 2000), as in magnetic bacteria (Frankel *et al.*, 1979) or in chiton teeth (Lowenstam, 1962). Biological control on mineralization implies in particular the presence of dedicated structural elements like membrane vesicles to control the crystal size and proteins to arrange the minerals (e.g. Mann, 2001).

If magnetic particles are found outside the cell, they are most likely to have accumulated by some other process, or could in the worst case represent contamination. To resolve the structure of a magnetoreceptor cell, and to confirm the intracellular nature of minerals, we use confocal imaging and scanning electron microscopy. Scanning electron microscopy can be used to distinguish between an object at the surface, and an object underneath a cover of cell membrane (see chapter 2.3.2).

c. Intracellular structure: How is the association between the magnetic object and the cell?

For the magnetite based theory it is crucial that the magnetic object is somehow mechanically linked to the cell membrane, or to transmembrane ion channels, in order to transmit the mechanical force for generating a neuronal signal. There are several ideas of how this could be built, for example, by tethering the magnetic inclusion to the cytoskeleton on one end, and to the membrane (or directly to ion channels) on the other end. Here the cytoskeleton is considered as a mechanical transmitter to open channels (Walker *et al.*, 2002). Without mechanical connection to the membrane, the magnetic particle can transmit field changes only by viscous drag. However, this implies that part of the magnetomechanical torque would be lost to set the cytosol in rotation and therefore that mechanism would be rather inefficient and result in a low-sensitivity sensor.

Further, the question rises whether there is a preferential direction for magnetic field stimulation of a cell, and if we look at the olfactory organ as a whole magnetoreception sensory organ, what is the distribution of preferential directions across the epithelium? Is it such that the sense organ would be sensitive to any vector orientation of the external field?

We designed experiments to answer some of the key questions mentioned here (see chapter 2).

d. Magnetic properties and structure of the magnetic object: What is the nature of the magnetic object?

So far we know that there are cells in the olfactory sensory epithelium that contain reflective objects, as shown with laser-scanning microscopy in reflectance mode (Walker *et al.*, 1997; Diebel *et al.*, 2000). Further, EDX (energy-dispersive X-ray) analysis under the TEM (Walker *et al.*, 1997) showed the reflective object to be associated with iron. While it has not been demonstrated directly that the iron-rich crystalline object is magnetic, it was shown in one instance to be remanence bearing with coercivity similar to bacterial single-domain magnetite (Diebel *et al.*, 2000).

Thus far, there are a number of indirect observations that hint toward the mineralogic nature of the reflective inclusions, but a firm proof for magnetite has not been delivered yet. A direct proof for magnetite/maghemite would be by electron-diffraction under the TEM (transmission electron microscope). Due to the elusiveness of the magnetoreceptor cells, and due to the TEM preparation procedures this is hard to achieve. Another method would be to identify the characteristic Raman lines of the specific magnetic mineral in the Raman spectra of the inclusion, using confocal Raman spectroscopy. Exposing the sample to a focused laser beam can easily oxidize magnetite crystals to hematite (Shebanova and Lazor, 2003b), and the precious information would be lost. This is in particular an issue for very small objects that oxidize easily due to their large surface to volume ratio, e.g. magnetosomes. In order not to burn precious trout samples, we will calibrate this method on magnetotactic bacteria, which are relatively easy to sample, and contain magnetite magnetosomes. (see chapter 3)

2

Magnetic characterization of isolated candidate vertebrate magnetoreceptor cells.

Magnetic characterization of isolated candidate vertebrate magnetoreceptor cells by Stephan H.K. Eder, Hervé Cadiou, Airina Muhamad, Peter A. McNaughton, Joseph L. Kirschvink, Michael Winklhofer. Published in Proceedings of the National Academy of Sciences, 2012, vol 109(30), pp. 12022-12027, doi: 10.1073/pnas.1205653109 .

2.1 Abstract

Over the past fifty years, behavioral experiments have produced a large body of evidence for the existence of a magnetic sense in a wide range of animals. However, the underlying sensory physiology remains poorly understood due to the elusiveness of the magnetosensory structures. Here we present an effective method for isolating and characterizing potential magnetite-based magnetoreceptor cells. In essence, a rotating magnetic field is employed to visually identify, within a dissociated tissue preparation, cells that contain magnetic material by their rotational behavior. As a tissue of choice, we

selected trout olfactory epithelium which has been previously suggested to host candidate magnetoreceptor cells. We were able to reproducibly detect magnetic cells and to determine, for the first time, their magnetic dipole moment. The obtained values (4 to 100 fAm^2) greatly exceed previous estimates (0.5 fAm^2). The magnetism of the cells is due to a μm-sized intracellular structure of iron-rich crystals, most likely single-domain magnetite. In confocal reflectance imaging, these produce bright reflective spots close to the cell membrane. The magnetic inclusions are found to be firmly coupled to the cell membrane, enabling a direct transduction of mechanical stress produced by magnetic torque acting on the cellular dipole in situ. Our results show that the magnetically identified cells clearly meet the physical requirements for a magnetoreceptor capable of rapidly detecting small changes in the external magnetic field. This would also explain interference of AC powerline magnetic fields with magnetoreception, as reported in cattle.

2.2 Introduction

Following the early idea that migrating animals might orient and navigate by the Earth's magnetic field, a large number of behavioral experiments have unequivocally established the existence of a magnetic sense in animals (see Wiltschko and Wiltschko, 2005, for a review). Nonetheless, so far only little is known about the biophysical principles that allow animals to detect the comparably weak geomagnetic field (Lohmann, 2010). Two working hypotheses for magnetoreception pathways are considered physically viable: i) biomineralized magnetite particles connected to mechanosensitive structures (Kirschvink and Gould, 1981; Kirschvink, 1992a; Winklhofer and Kirschvink, 2010) and ii) magnetically sensitive chemical reactions involving a short-lived radical pair intermediate state (Schulten *et al.*, 1978; Rodgers and Hore, 2009; Ritz *et al.*, 2010). Magnetoreception by electromagnetic induction is considered possible only in marine electrosensitive animals (Paulin, 1995; Peters *et al.*, 2007).

Salmonids, as well as zebra fish (Cypriniformes), yellowfin tuna and Mozambique tilapia (Perciformes), which all lack electroreceptors (Albert and Crampton, 2005), have been found to use the local magnetic field as a directional cue (Quinn, 1980; Taylor, 1986) or to respond to artificial magnetic field stimuli in conditioning experiments (Walker *et al.*, 1984, 1997; Shcherbakov *et al.*, 2005; Hellinger and Hoffmann, 2009). Most significantly,

Walker *et al.* (1997) were able to detect magnetically responding units in electrophysiological recordings from the superficial ophthalmic branch (rosV) of the trigeminal nerve of rainbow trout (Oncorhynchus mykiss) and to trace the origin of some of these units back to the olfactory epithelium. The candidate magnetoreceptor cells in the olfactory sensory epithelium were suggested to contain conspicuous iron-rich crystalline inclusions (Walker *et al.*, 1997) with magnetic properties consistent with single domain magnetite (Diebel *et al.*, 2000). Despite this progress towards identifying the structural basis of magnetite-based magnetoreception in vertebrates, a number of key problems remain to be solved.

First and foremost, a method to quickly identify candidate magnetoreceptor cells should be established. Once such cells can be reproducibly isolated, specific experiments can be designed to study the nature of the cells and to provide biophysical constraints on the functional behavior of the magnetic inclusions. Here we present an ex vivo approach to tackle the problem of identifying and characterizing magnetite-based candidate receptor cells. In essence, a magnetic-field rotating in the focal plane of a light microscope is used to specifically look for magnetic cells in a suspension of cells, obtained by gentle dissociation of a sensory epithelium tissue. Magnetic cells will rotate with a frequency equal to that of the external magnetic field if their magnetic inclusions are linked to the cell membrane or at a slower rate if the magnetic torque is transmitted by intracellular viscous drag. Studying the characteristic hydrodynamic response time of magnetic cells to a magnetic field, we can test if the magnetic inclusion has a mechanically strong connection to the cell membrane and at the same time determine the cellular dipole moment.

2.3 Results

2.3.1 Visual detection of candidate cells

In order to identify magnetic-material containing cells, we exposed a dissociated trout olfactory epithelium preparation to a moderately strong external magnetic field (2 mT) rotating slowly (0.33 Hz) in the focal plane of the microscope. Using these conditions, we observed the rotation of rare objects within the preparation. The dissociation of a pair of olfactory rosettes yielded, on average, 10^4 single cells in suspension, of which between one and four were found to rotate synchronously with the magnetic field.

This result was observed in more than 50 animals. The majority of the magnetic cells had an elongated shape with typical dimensions of 10 to 20 μm and aspect ratio of 1.6, as the one shown in figure 2.1A. Another interesting feature of these cells is that they all contained an opaque inclusion under transmitted light (figure 2.1A, red arrows), which was highly reflective when observed in reflective light dark field (figure 2.1B, red arrows). In order to confirm the cellular nature of these rotating objects, we used the lipophilic dye FM 1-43fx, a marker already implemented for magnetotactic bacteria (Keim *et al.*, 2004). A typical wide-field fluorescence image of a rotating cell stained with FM 1-43fx can be seen in figure 2.1B. (See movies MOV1 and MOV2 for the full sequences from which figure 2.1A-B were extracted). The intracellular nature of the reflective objects was confirmed by confocal microscopy (figure 2.2). The opaque inclusions seen in the wide-field transmitted-light image (figure 2.1A) appear in confocal reflectance mode as brilliant elongated objects, with typical sizes of 1 - 2 μm (figure 2.2B). Under close inspection, these objects can be resolved into a structure of several reflective spots (see inset in figure 2.2B). Significantly, the reflective objects are always found in the interior of the cell, well separated from the nucleus (see DAPI signal in figure 2.2D), but close to the cell membrane.

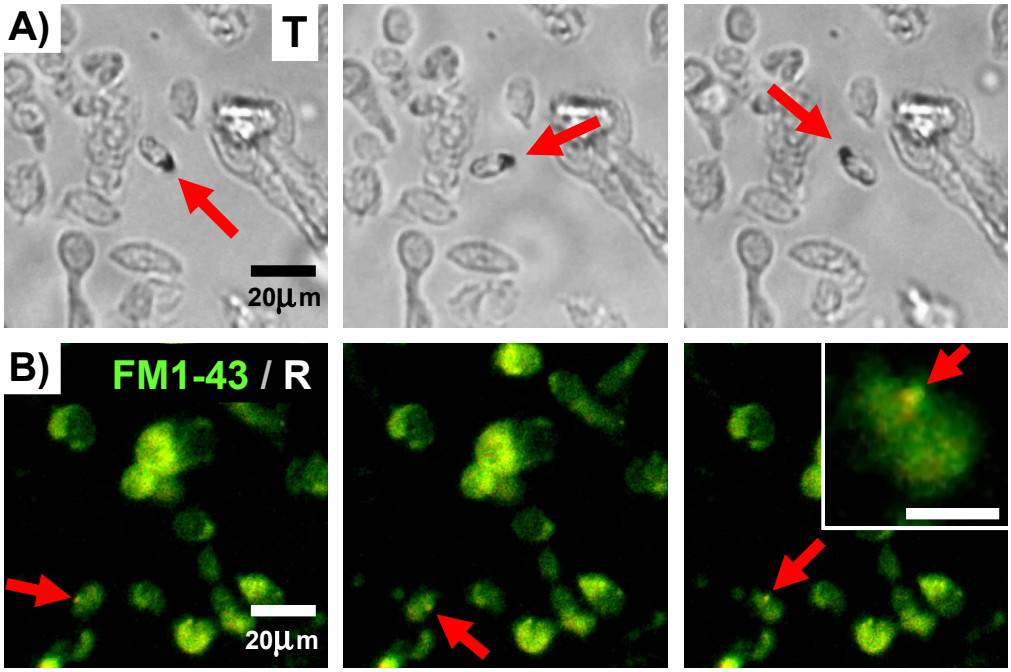

Figure 2.1: Time lapses of cell suspension from dissociated trout olfactory epithelium, showing individual cells rotating with magnetic field. (See movies MOV1 and MOV2 for the two full sequences from which time lapses were extracted). A) Transmitted light (T), showing an opaque inclusion (red arrow) in the rotating object. B) Simultaneously recorded dark-field reflection (R) and fluorescence (FM1-43, lipophilic dye), showing reflective objects (white) and cell membrane (green). The rotating cell contains a strongly reflective inclusion (red arrow), displayed as close-up (upper right corner, scale bar 10μm).

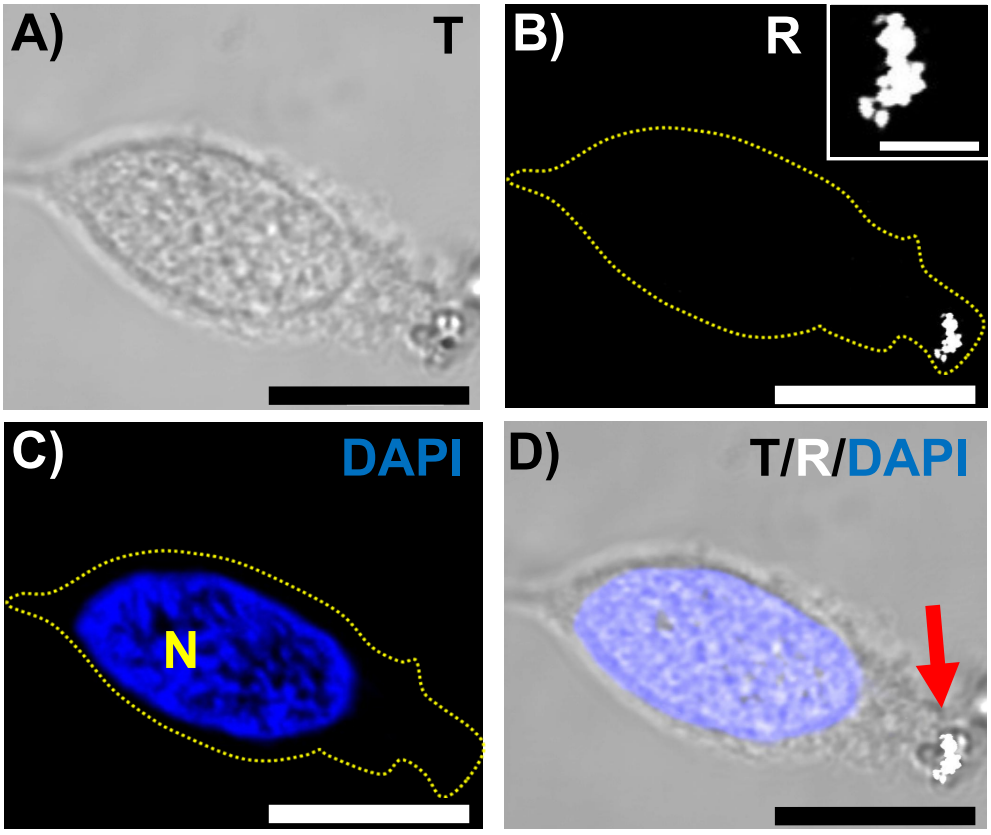

Figure 2.2: Confocal images of candidate magnetoreceptor cell. A) Transmitted light (T). B) Same cell viewed in confocal reflectance mode (R). Dashed yellow line indicates cell outline. Reflective inclusions inside the cell, with a close-up view (upper right window, scale bar: 2μm). C) Confocal fluorescence image showing DAPI labeling of the same cell. N: nucleus. Dashed yellow line: cell outline. D) Composite image showing the nucleus and the reflective inclusions (red arrow). Scale bar: 10μm.

2.3.2 Intracellular iron detection

Some of the rotating cells were transferred onto clean glass slides in order to study the nature of the reflective objects (figure 2.3A, red arrow). Our working hypothesis was that the reflective objects seen in light microscopy carry the magnetism of the cell. Therefore it must be an iron rich material since iron is the only element known to occur in biogenic magnetic minerals. The transferred cell shown in figure 2.3 suffered a loss in integrity, giving us the opportunity to test whether the reflective object is strongly associated with the membrane or contained within the cytoplasm. As can be seen by

comparing the reflected-light image (figure 2.11 A,B) with the backscattered-electron image (figure 2.3A), the reflective object corresponds to the bright spot that strongly backscatters electrons. In contrast, no high-contrast feature is observable at that position in the secondary-electron image (figure 2.3B), which shows the surface properties of the sample. Since secondary electrons do not originate from deeper than 10 nm in a solid material, we can tell from the secondary-electron image (figure 2.3B) that the reflective object is a cellular inclusion and not an external contaminant which would otherwise be clearly visible as a high-contrast secondary-electron feature. Elemental analysis of the region containing the high contrast backscattered-electron feature shows a strong iron peak (figure 2.3C), which was not seen outside that region. In contrast, the cytoplasm residue neither exhibited reflective objects nor had iron detectable by energy-dispersive X-ray analysis. The observation that the reflective object in the magnetically extracted cell corresponds to the iron rich, high-contrast backscattered-electron feature demonstrates that the reflective object is responsible for the magnetic properties of the cell. The magnetic inclusion most likely is mechanically anchored to the cell membrane rather than freely suspended in the cytoplasm, since it remained in the cell after disruption rather than having been expelled with the cytoplasm.

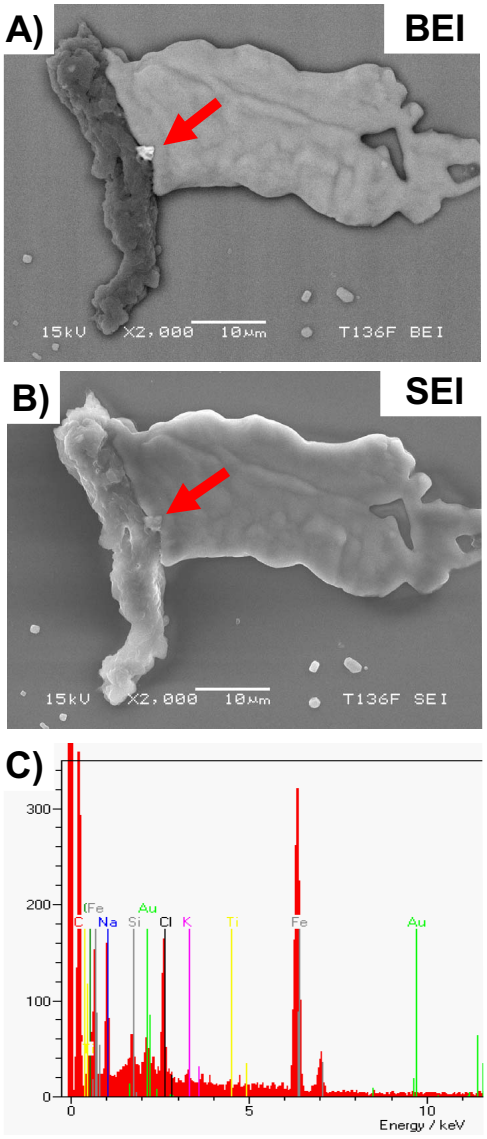

Figure 2.3: Scanning electron microscopy of a previously rotating cell. Scale bars: 10μm. A) Backscattered electron image of the magnetic cell (left/vertical structure), which has lost cytoplasm (expelled to the right) during osmotic disintegration. The magnetic inclusion was retained (red arrow) and strongly backscatters electrons due to its high material contrast. B) Secondary electron image does not reveal a contrast feature at the surface above the inclusion, demonstrating its intracellular nature. C) Energy dispersive X-ray spectrum of the inclusion, showing a strong iron peak.

2.3.3 Magnetic characterization

The hypothesis that the magnetic inclusion has a mechanical connection to the cell membrane implies that the magnetic cell rotates at the same frequency as the driving frequency of the external magnetic field. Conversely, if the magnetic inclusion is only freely suspended in the cell, then there will be differential rotation between the cell membrane and the magnetic inclusion, as a consequence of which the cell will rotate at a distinctly slower rate (see chapter 2.7 Supplementary text).

The cells were observed to rotate at the same frequency as the driving frequency of the external magnetic field. The time lapses displayed in figure 2.1A shows a 174±2° turn corresponding to 22 frames recorded at 15 fps, thus giving a frequency of 0.330±0.003 Hz, which agrees with the driving frequency of 0.330 Hz. We did not observe any significant deviation between the driving and the cellular spinning frequency in any cell. From the absence of a frequency lag, we can conclude that the magnetic inclusions are directly coupled to the cell membrane rather than just viscously. This allows us to determine the magnetic dipole moment of the cells using the rotating field method (see Chapter 2.5).

The magnetic dipole moment of N=13 cells derived from eight animals is plotted as a function of the external magnetic field intensity B in figure 2.4. Most importantly, one can see that the magnetic moment is largely independent of the magnetic field strength over the field range covered here, which indicates that the cellular dipole moment is due to remanence-bearing - most likely single-domain - particles as opposed to superparamagnetic or multi-domain particles, which would exhibit a pronounced dependency on B. Neither the fish nor the dissociated cells had been exposed to fields larger than 3 mT, which is below the switching fields required to remagnetize biogenic single-domain particles of magnetite in salmon (Kirschvink *et al.*, 1985a; Walker *et al.*, 1988; Moore *et al.*, 1990). Hence, the measured magnetic dipole moments most likely reflect their natural values. It is possible that the original internal structure of the magnetic inclusion might not always have been conserved during sample preparation, in which case the natural cellular magnetic moment would be somewhat larger than the observed one.

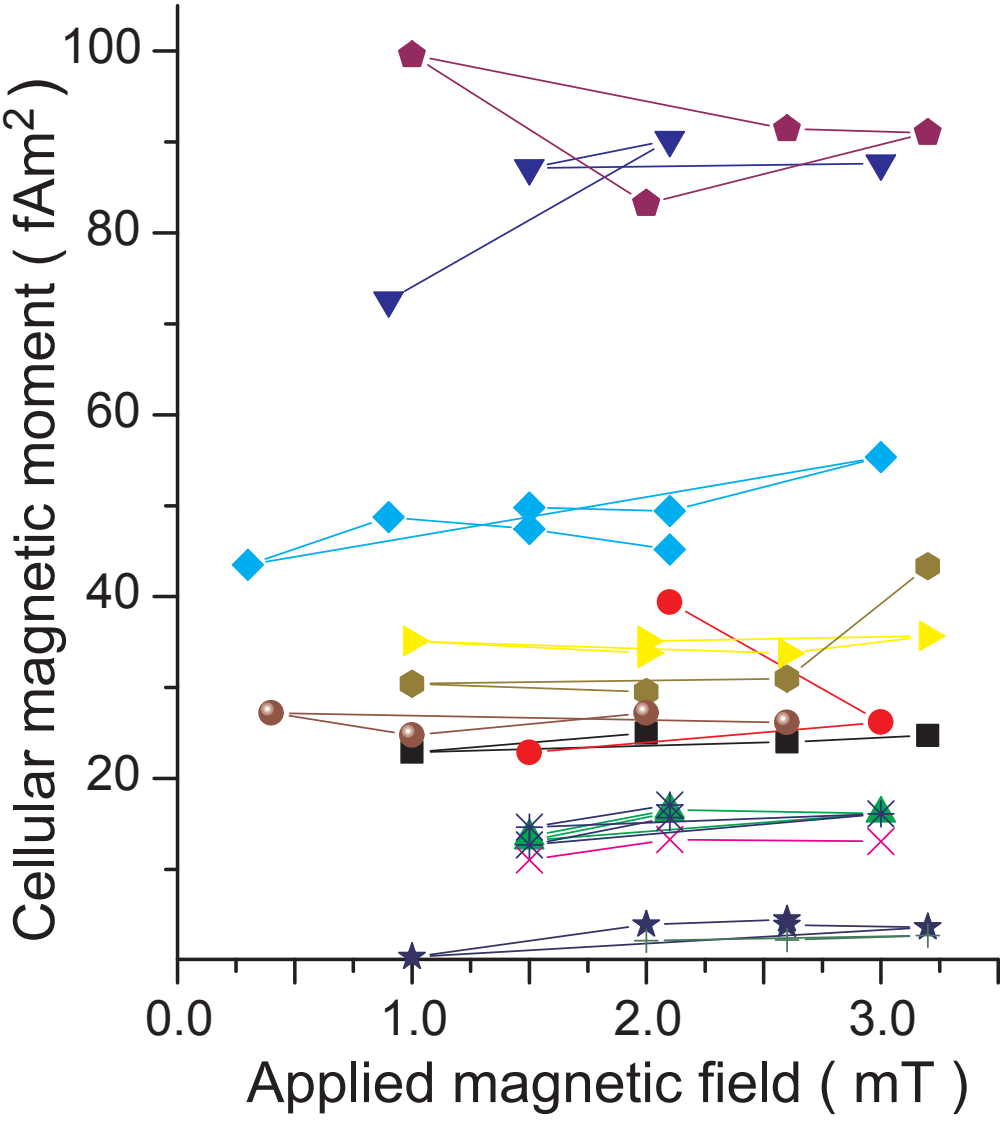

Figure 2.4: Measured magnetic dipole moment as a function of the rotating magnetic field amplitude B for 13 cells. The individual (B) measurements for a given cell are connected according to the measurement sequence. See Table 2.1 for numerical values.

2.3.4 Test for cytoskeletal connection of magnetic inclusion

The previous results have shown that the particle is located inside the cell (figures 2.2, 2.3) and has a firm mechanical connection to the cell membrane. To specifically test whether the magnetic inclusions have a connection to the cytoskeleton, we used pharmaceutical agents, Latrunculin B and Colchicine, to specifically disrupt the cytoskeletal filaments F-actin and microtubules, respectively. If connected through these filaments to the cell membrane, the magnetic inclusion will become detached upon disruption, which then will result in differential rotation. We tested six cells with both drugs and found no decrease in the rotation rate of the magnetic cells relative to the driving frequency. From this observation, we conclude that these cytoskeletal filaments are not necessary for maintaining the mechanical connection of the magnetic inclusion to the cell membrane.

2.4 Discussion

We are able to unambiguously identify a cell as magnetic by its dynamic response to a rotating field. The method has three advantages in the search for candidate magnetite-based magnetoreceptor cells:

1) Detection of magnetic cells is highly specific, whereas other techniques based on iron detection (e.g., Prussian Blue staining of tissue sections) may give false positives, because not all biological iron compounds are (ferri)magnetic. Having used moderate magnetic field amplitudes, we can rule out false positives in the form of cells with inclusions of antiferromagnetic compounds (e.g., macrophages containing ferritin-like granules, siderosomes, and hemosiderin (Treiber *et al.*, 2012), whose induced magnetization would become important only in much stronger magnetic fields. To achieve this goal, we accept false negatives represented by larger cells carrying a relatively low remanent magnetic moment, i.e., cells with magnetorotational mobility α much smaller than the f_B/B ratio we set when searching for spinning cells in suspension (see chapter 2.7 Supplementary Text). Usage of a stronger magnetic field (lower f_B / B ratio) is likely to increase the experimentally accessible range of magnetic cells towards low values of, but comes with the risk of obtaining false positives, which would then have to be sorted out using different methods. In such a case, a simple criterion for the presence or absence of magnetic remanence

would be a field-flip test on a magnetic object in the suspension. A cell carrying magnetic remanence would rotate by 180°, whereas objects with induced magnetization would not. Further, we suggest the absence of distinct reflective particles in the visible cellular structure as a criterion for identifying false positives.

2) The method allows for a very sensitive measurement of the magnetic dipole moment of the cell, which is a key parameter in theoretical models of the receptor sensitivity threshold. The cellular magnetic dipole moments determined range from 4 - 100 fAm^2 which in a typical present-day Earth-strength magnetic field of 0.05 mT corresponds to a magnetic-to-thermal energy ratio μB/kT of about 50:1 to 1200:1 at physiological temperatures. These figures, on average, are significantly larger than those reported for most magnetotactic bacteria, which have magnetic moments of 0.2 - 1.7 fAm^2 (Frankel *et al.*, 1979; Kalmijn, 1981; Esquivel and Lins de Barros, 1986; Winklhofer *et al.*, 2007; Erglis *et al.*, 2007; Pan *et al.*, 2010). There are notable exceptions, however, such as *Magnetobacterium bavaricum* (10 - 60 fAm^2) (Steinberger *et al.*, 1994; Hanzlik *et al.*, 2002) as well as some vibroid (8 fAm^2) (Hanzlik *et al.*, 2002) and some coccoid bacteria (2.4 - 54 fAm^2) (Esquivel and Lins de Barros, 1986). Diebel *et al.* (2000) used magnetic force microscopy (MFM) for detailed magnetic measurements on substructures of magnetic inclusions in an embedded trout olfactory epithelium. They obtained 0.5 fAm^2 (μB/kT ~ 6) for a group of crystals close to the scanned surface. The MFM technique is particularly sensitive to magnetic structures close to the surface of a tissue block, but may underestimate the total magnetic moment of an intracellular inclusion dipping steeply away from the surface and extending one or two micrometers into the depth coordinate. The physical reason is the fast decay ($1/r^3$) of the magnetic stray field with distance from the magnetic source region. The rotating-field method in contrast quantifies the total magnetic moment of an individual cell. Given that the cellular magnetic inclusions are made of single-domain magnetite (470kA/m saturation magnetization) and assuming that all crystals are magnetized along the direction of the cellular magnetic dipole moment, just like in a bacterial magnetosome chain, our cellular magnetic moment values of 4 -100 fAm^2 translate into a minimum magnetite volume of 0.01 - 0.2 μm^3 per cell. Taking typical crystal dimensions of about 50 nm (c.f. figure 2a in ref. Diebel *et al.*, 2000), we obtain a minimum of 70 - 1700 crystals per cell. It is clear that the crystals are not arranged in a linear chain, which would result in highly elongated inclusions exceeding the typically observed length of 1 - 2 μm, which also rules out a collapsed single-chain

structure, as sometimes observed as a preparation artifact of magnetotactic bacteria (Shcherbakov *et al.*, 1997). Rather, we suggest that the particles are arranged in the form of tightly packed bundles of chains, perhaps similar to the multi-stranded chains of magnetosomes described in *M. bavaricum* (Hanzlik *et al.*, 2002, 1996; Jogler *et al.*, 2011). It is important to note that crystals as small as 50 nm produce a pronounced reflection contrast under the confocal microscope, but the optical resolution limit of about 250 nm does not allow one to resolve the reflective spots seen in figure 2.2 into individual crystals. Each of these spots is likely to represent groups of crystals.

3) The method can be used to test whether magnetic inclusions are linked to the cell membrane, which is an important constraint when it comes to understanding the working principle and possible transduction pathway of magnetic signals in candidate magnetite-based magnetoreceptor cells (Winklhofer and Kirschvink, 2010). The fact that we observed an immediate mechanical reaction without differential rotation of candidate cells to a change in the external magnetic field implies that the magnetic torque acting on the magnetic inclusion is transmitted to the cell membrane through a mechanically strong connection rather than by mere viscous coupling across the cytoplasm. Actin filaments or microtubules do not appear to play a key role in the link because cells kept rotating after filament disruption. We hypothesize that the magnetic crystals are enclosed in a membrane structure contiguous with the cell membrane. This fits with our electron microscopy observations showing that inclusions are located close to the cell membrane.

A mechanically strong connection between magnetic dipole and cell membrane means transmission of stress without requiring motion of the magnetic inclusion, which avoids signal loss through viscous dissipation associated with motion. A number of theoretical models of magnetite-based magnetoreceptors assume rotational motion and conclude that viscous damping is too strong for the receptor to be susceptible to extremely low-frequency (50 - 60 Hz) magnetic fields due to AC powerlines (Kirschvink, 1992a; Adair, 2000; Vanderstraeten and Gillis, 2010). While this conclusion is theoretically sound, we find no evidence for rotational motion of the magnetic inclusion inside the cell, not even at 0.3 Hz. We therefore suggest that magnetic fields due to AC powerlines may well affect a magnetoreceptor with magnetic inclusions that are strongly mechanically coupled to the cell membrane. Interestingly, such fields have been reported to perturb the magnetic alignment behavior of artiodactyls and have been suggested to interfere with a magnetoreceptor (Begall *et al.*, 2008; Burda *et al.*, 2009). Direct measurements of threshold sensitivity vs. frequency in honeybees

(Kirschvink *et al.*, 1997) found a strong frequency drop-off and it is possible that magnetite-based Insect magnetoreceptors might have different cellular physiology. In our proof-of-principle study, we focused on the olfactory epithelium of trout, which has been previously suggested to host candidate magnetoreceptor cells (Walker *et al.*, 1997; Diebel *et al.*, 2000). Ethmoid tissue (Walker *et al.*, 1988; Mann *et al.*, 1988), lateral line (Moore *et al.*, 1990), inner ear lagena receptors (Harada *et al.*, 2001; Wu and Dickman, 2011, 2012), corneal epithelium (Wenger *et al.*, 2006), and trigeminally-innervated regions of the upper beak of birds (Heyers *et al.*, 2010) are other promising targets when searching for magnetic cells, which should be dispersed to avoid magnetostatic interactions.

In conclusion, we have introduced a new technique for isolating and characterizing candidate magnetite-based magnetoreceptor cells from dissociated tissue. We can reproducibly identify such cells under the microscope using a rotating magnetic field. By switching from transmitted light to reflected light in dark field, one can directly visualize highly reflective intracellular inclusions carrying the magnetism of the cell. Scanning electron microscopy demonstrated that iron-rich domains in magnetically isolated cells correspond to reflective objects under the light microscope. The measured magnetization curves of individual cells are consistent with single-domain magnetite. Surprisingly, the magnetic dipole moment of the candidate receptor cells is much larger than previously estimated and therefore not only sufficient to detect the direction of magnetic north, but also likely to form the basis of an accurate magnetic sensory system with which to extract positional information from small spatial variations of geomagnetic field intensity and directions (Lohmann *et al.*, 2008). The large magnetic moment also enables magnetoreception during times of low geomagnetic field strengths (Kirschvink *et al.*, 2010). Our observations indicate a firm connection between magnetic inclusion and cell membrane, which suggests an effective mechanism of transmitting the magnetic torque directly to stress-sensitive transducers without involving rotational motion and viscous damping. We believe that our technique has more control on the isolation of candidate cells than commercially available magnetic cell sorters and therefore sets the basis for a high-throughput method to collect cells for transcriptomic and proteomic analysis so as to study the molecular basis of magnetoreception and magnetite biomineralization.

2.5 Material and Methods

Theory.

Consider a magnetic cell free to rotate in a suspension of cells. When exposed to an external magnetic field $\vec{B(t)}$ rotating at constant frequency f_B in the focal plane, a magnetic cell with permanent magnetic dipole moment $\vec{\mu}$ stiffly connected to the cell body will experience a magnetic torque $\vec{N}_{mag} = \vec{\mu} \times \vec{B}$ and a viscous resistance, $\vec{N}_{vis} = -\eta \mathrm{C} \cdot \vec{\omega}$, where C is the tensor of frictional resistance coefficients for rotation in a viscous medium, η is the viscosity, and $\vec{\omega}$ is the instantaneous angular velocity of the cell. For a spherical cell with radius a, C is scalar and given by the well-known expression $C = 8\pi a^3$ (the components of C for ellipsoidal cells are treated in the Chapter 2.7: Supplementary text). Introducing the rotation angle of the magnetic moment, $\vartheta(t) = \omega t$, and the rotation angle of the magnetic field, $\varphi_s(t) = 2\pi_s t$, where both are measured from the same point of reference in the focal plane, the torque balance can be written as

$$\mu B sin(\varphi - \vartheta) = \eta C \frac{d\vartheta}{dt} \tag{2.1}$$

Stationary solutions to this differential equation exist for a constant lag angle $\psi = (\varphi - \vartheta)$ between the magnetic moment and the magnetic field vector. Stationary conditions imply: $0 = d\psi/dt$, i.e., $0 = d\varphi/dt - d\vartheta/dt = 2\pi f_s - \omega$, i.e. $\omega = 2\pi f_s$, and equation 2.1 simplifies to

$$\frac{\mu B}{2\pi\eta C} sin\psi = f_s \tag{2.2}$$

The maximum frequency f_s of the external field (of a given intensity B) up to which the cell can rotate synchronously with the field (i.e., at $\omega = 2\pi f_s$) is given for a phase lag of $\psi = 90°$, and can be used to measure the magnetic dipole moment:

$$\mu = 2\pi\eta C \frac{f_B^{max}}{B} \tag{2.3}$$

where f_B^{max} is also referred to as the boundary frequency (Steinberger *et al.*, 1994). It is convenient to introduce the magnetorotational mobility α of a cell, i.e., $\alpha = \mu/(2\pi\eta C) = f_B^{max}/B$, which is a constant for a cell dominated by remanent magnetization. If the ratio f_B^{max} to B increases with applied field strength, then the induced magnetization plays a role too, even

though it is not the total induced magnetization, but only its anisotropic part that contributes to the torque. In the supplementary text (Chapter 2.7), it is shown that this anisotropic part of the induced magnetization leads to a B^2 dependency of f_B^{max} once the induced magnetization becomes larger than the remanent magnetization. To determine whether magnetization is due to remanence or to anisotropic magnetic susceptibility, we experimentally determined f_B^{max} for a range of B values for each cell.

Magnetoscope.

To have precise control over the magnetic field in the focal plane, two orthogonal pairs of square coils were mounted around an inverted optical microscope (Zeiss ICM405 with Epiplan 40x, 0.85 N.A. HD, and 16x, 0.35 N.A. HD). The few magnetic parts of the microscope table were replaced by nonmagnetic ones to ensure a homogeneous magnetic field within the sample plane. To rotate the magnetic field in the sample plane, the two coil pairs are fed with sinusoidal currents that have a constant phase shift of 90 degrees relative to each other. The sinusoidal signals are generated by a two-channel arbitrary waveform generator (model M631, ETC, Slovak Rep.) and amplified with 400 Watt (50 V, 8 Amp) bipolar power supplies (Kepco Inc., NY, USA).

Animals and cell isolation procedure.

Rainbow trout (length ∼10 cm) were purchased from Mauka fish farm, Massenhausen, Germany and kept in a water circulating tank at 12°C. Animals were killed in accordance with the German Animal Welfare Act (TierSchG). For animal killing, dissection and cell isolation, iron-free nonmagnetic tools made of titanium, ceramics, and glass were used in order to avoid contamination with external iron present in standard labtools. All tools and labware, if not pre-sterilized, were cleaned in HCl or ethanol. Cell isolation was carried out as follows. After killing, olfactory rosettes were dissected out from both nasal cavities, using capsulotomy titanium scissors (Vannas), and placed in Ringer-1 solution on ice (containing in mM: NaCl (100), KCl (3), $CaCl_2$ (2), $MgCl_2$ (1), HEPES (5) as buffer, glucose (10) and adjusted to pH 7.4). All chemicals were of molecular biology grade (SigmaUltra) and buffers were made using Milli-Q water. For the dissociation of the olfactory epithelium, the rosettes were rinsed with Ringer-2 solution (without divalent cation salts, but otherwise identical to Ringer-1) and cut into mm size pieces, followed by an incubation of 10 min in Ringer-2

solution under the presence of Papain (Sigma; 0.25 mg/ml) activated with L-Cystein (Sigma; 1.25 mg/ml), under constant stirring. After 10 minutes, the enzyme solution was removed and cells were washed twice with Ringer 2. The olfactory rosettes were then triturated gently using a fire polished Pasteur pipette tip. The dissociated cells were then centrifuged and the pellet resuspended in Ringer-1. Cells were left at 4°C until use. The viscosity of Ringer-1 was measured with a concentric-cylinder viscometer (Brookfield Eng. Labs, MA, USA).

Identification and extraction of magnetic cells.

For detection of magnetic cells, a drop of the final cell suspension was placed on silanized coverslips (size 0, Menzelglaesser). Silanisation was achieved by adding chlorotributyl silane (Sigma-Aldrich) to glass coverslips and placing them in an oven at 150°C for 20 minutes. This step was crucial in preventing cells from attaching to the glass surface. When searching for magnetic cells under the magnetoscope, we continuously rotated the magnetic field vector in the focal plane at a rotation frequency of $f_B = 0.33Hz$ and field intensity B=2 mT (activating synchronous rotation of cells with $\alpha \geq 0.17$ mT^{-1} sec^{-1}, see chapter 2: Supplementary Text) and systematically examined the suspension by scanning the preparation until a rotating cell was found. A field of 2 mT is low enough to avoid irreversible switching of single-domain particles. To determine the characteristic orientation time of a magnetic cell at a given external field strength B, we increased the field frequency f_B up to the point where the cell stopped rotating synchronously with the external field. Detailed magnetic measurements were performed on 8 pairs of dissociated rosettes, which for this purpose were prepared in wet mounts with petroleum jelly seal to avoid desiccation-induced fluid motion (evaporation drift), which would otherwise produce additional force couples on the cells which are difficult to correct for in the theoretical treatment. In order to discriminate between cells and possible inorganic contaminants, we applied the lipophilic fluorescent dye FM 1-43fx (Invitrogen) at a final concentration of 5 μM in the sample solution. For extraction, magnetically identified cells in preparations without coverslip were collected by suction (CellTram® vario, Eppendorf) with a micro-capillary (FemoTips®, Eppendorf) positioned with a joystick-controlled micromanipulator (PatchMan NP2; Eppendorf).

Image processing.

The snapshots shown in figure 2.1 of the paper have been extracted from the movies MOV1 and MOV2 in the supplement, each recorded at 15 frames per second with a CCD camera (Chameleon, Point Grey, Canada). All snapshots were despeckled with Image J software (NIH, USA). In addition, the fluorescent images (figure 2.1B) were color-contrast balanced in Image J (NIH).

Confocal imaging.

Dissociated olfactory cells were fixed using PFA 4% in PBS with 0.2% glutaraldehyde, mounted with Vectashield hardmount mounting media containing DAPI, and sealed with coverslip. The settings of the confocal reflectance mode of the laser scanning microscope (Leica SP5 with DMI6000 B and x63 objective) were calibrated on magnetite chains in magnetotactic bacteria (Walker *et al.*, 1997; Green *et al.*, 2001), while *E. coli* was used as negative control. Further analysis and image presentation were performed using Image J software (NIH).

Disruption of cytoskeleton.

For cytoskeleton disruption, dissociates containing spinning cells were observed for at least 30 minutes after treatment with latrunculin-B (Sigma L5288, final concentration 100 μM against F-actin or colchicine (Sigma C9754, final concentration 500 μM) against microtubules, in concentrations high enough to disrupt the filaments (Woell *et al.*, 2005) rather than to just stop them from polymerizing.

Scanning electron microscopic analysis.

Single cells were extracted and transferred to a coverslip with a grid to locate the cell after drying of the sample. Cells were plasma coated with gold and observed at under a JSM5900LV (Jeol, Japan) at 15 kV. Elemental analysis was done with energy-dispersive X-ray spectroscopy at 15 kV (Röntec, Germany).

2.6 Acknowledgments

We thank Marianne Hanzlik, Valera Shcherbakov, Gil Westmeyer, and David Keays for discussions. This work was supported by the Human Frontier Science Organization (HFSP Grant RGP 28/2007 to J.L.K., P.A.M., M.W.), Deutsche Forschungsgemeinschaft (DFG Grant Wi 1828/4-1 to M.W.), and the University of Malaya and Ministry of Higher Education Malaysia (to A.M.).

2.7 Supplement material

2.7.1 Magnetic Field Settings

A magnetic cell in a suspension of cells has magneto-rotational mobility $\alpha = \mu/(2\pi\eta C)$, where μ is the permanent magnetic dipole moment of the cell, C is its hydrodynamic friction coefficient, and η is the viscosity of the liquid in which the cell is immersed. The population of magnetic cells in a dissociated tissue preparation is characterized by a distribution $n(\alpha)$ of magneto-rotational mobility and we ask which fraction of the population can be set in rotational motion by an external magnetic field of intensity B and rotational frequency f_B. Since the critical frequency for rotation in synchrony with an external magnetic field is given by $f_B^{max} = \alpha B$, the field setting (B, f_B) selects those cells in the population that meet the criterion:

$$\alpha \geq \frac{f_B}{B} \tag{2.4}$$

In other words, cells satisfying equation 2.4 can be easily recognized by their rotational motion when scanning the preparation for rotating cells. These cells are termed "experimentally well accessible" and their key parameters (μ, a) plot on the upper left in the rotational actuation nomogram (figure 2.5. If the frequency f_B is slightly increased beyond the critical frequency f_B^{max} of a given cell, then that cell stops rotating in synchrony with the field and starts to make clockwise and anti-clockwise quarter-turns in rapidly alternating sequence. This phenomenon is equivalent to apparently chaotic swimming trajectories displayed in magnetic bacteria when the driving frequency exceeds the critical frequency (Erglis *et al.*, 2007). With yet larger excess frequency, the amplitude of the oscillatory motion decreases fast and eventually (say at $f_B/f_B^{max} > 2$)

is hardly recognizable, that is, the cell appears to shiver slightly, which makes it difficult to discriminate magnetic actuation against Brownian motion. Therefore, although potentially still accessible with the rotating field method, cells with $f_B^{max} < f_B$ can in general not be considered "experimentally well accessible", hence our cut-off criterion (equation 2.4). It is obvious from equation (2.4) that a slowly rotating but strong magnetic field increases the chances of identifying magnetic cells by their rotational motion when visually screening a dissociated tissue preparation. We found $f_B = 0.33$ Hz to be an experimentally convenient rotation frequency, which is a good compromise between search speed and probability of finding a spinning cell. By limiting the magnetic field intensity to values well below 5 mT (e.g. 2.1 mT, as in figure 2.5, one can avoid remagnetization of biogenic single-domain magnetite, in which case their original magnetic state would be irreversibly lost. This restriction is of course relevant only if the aim is to measure the natural remanent magnetic dipole moment of identified cells. If harvesting of magnetic cells is the key task instead, then the magnetic field intensity should be set to larger values. When going from 2.1 to 8.4 mT, cells with 4 times smaller magnetic dipole moment become theoretically accessible (for a given cell size), or for a given magnetic moment, cells with $4^{1/3} \approx 1.6$ times larger diameter. However, upon further increasing the field strength, one runs risk of magnetizing cells containing higher amounts of biologically bound iron or waste, which need to be sorted out in a second stage process.

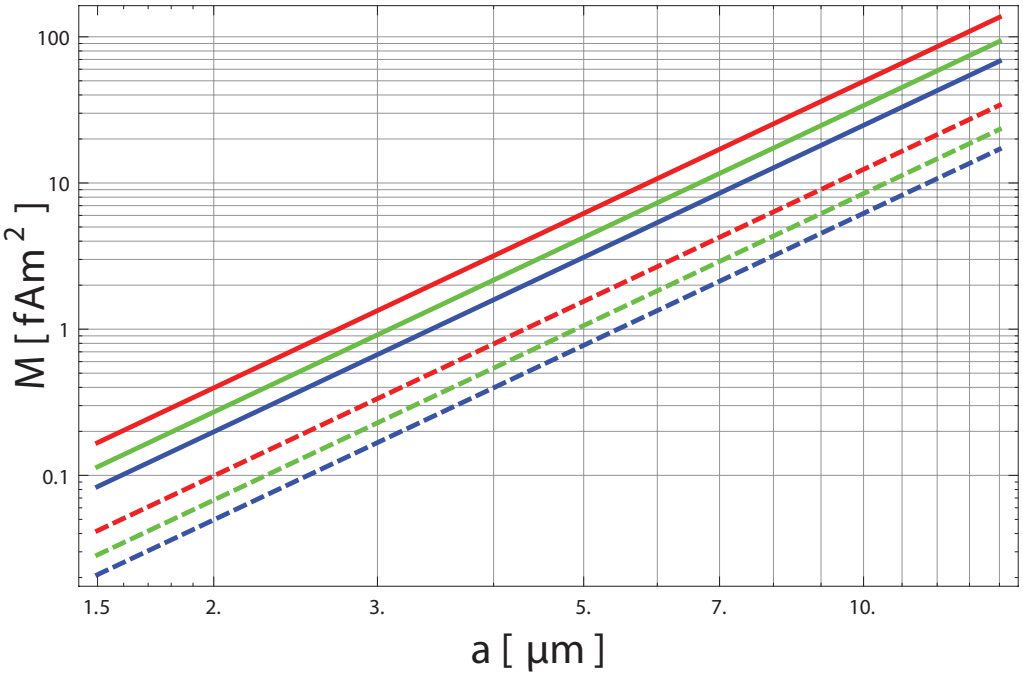

Figure 2.5: Nomogram for rotational actuation: Cut-off-values for synchronous rotation of a magnetic cell with permanent magnetic dipole moment μ and short half-axis a, for two different f_B/B ratios. Solid lines correspond to $f_B = 0.33Hz$ and B=2.1 mT (21 Oe), dashed lines correspond to $f_B = 0.33Hz$ and B=8.4 mT. Blue: spherical cells, with cell radius a; green: cells rotating about long axis, with axial ratio 1.6 and short half axis a; red: cells rotating about short axis, with axial ratio 1.6 and short half axis a. Experimentally well accessible μ values for a given cell dimension and a given experimental f_B/B ratio are above the corresponding line. In the calculations the viscosity of the medium was taken as 1 mPa sec (1 cPs).

2.7.2 Ellipsoidal Cells.

Elongated cells spinning about figure axis i are modeled using the frictional resistance coefficients C_i for the general ellipsoid, given by Jeffrey (1922),

$$C_i = \frac{16\pi}{3} \frac{a_j^2 + a_k^2}{a_j^2 P_j + a_k^2 P_k} \tag{2.5}$$

which depend on the geometry of the cell (semi-axes a_1, a_2, a_3), and the volume of the fluid in which the cell is immersed, through the upper limit s_{max} of the elliptic integrals

$$P_\lambda = \int_0^{s_{max}} \frac{ds}{(a_\lambda^2 + s)\sqrt{(a_1^2 + s)(a_2^2 + s)(a_3^2 + s)}} \tag{2.6}$$

where s is the algebraically largest root of the equation for an ellipsoidal surface in the liquid that is confocal with the immersed ellipsoidal cell,

$$\frac{x_1^2}{a_1^2 + s} + \frac{x_2^2}{a_2^2 + s} + \frac{x_3^2}{a_3^2 + s} = 1 \tag{2.7}$$

where the surface of the cell is given by $s = 0$. The rotation of an ellipsoidal cell produces a flow field of ellipsoidal symmetry with radially outward decreasing angular velocity, that is, adjacent fluid layers (ellipsoidal shells) are rotated differentially. For a fluid boundary located at s_{max}, the no-flow boundary condition implies enhanced shear stress (friction) so that the proximity of a fluid boundary to a rotating cell always increases C_i. This is mathematically obvious from equation (2.6), which has a monotonously decreasing, but always positive finite kernel, so that increasing s_{max} always increases the integral; since C_i has P_i in the denominator, C_i is minimum for $s_{max} \to \infty$. In the limit $s_{max} \to \infty$, P_i can be evaluated in terms of elliptic integrals of the first and second kind (MacMillan, 1958) and it is worth mentioning that P_i is mathematically equivalent to the demagnetization tensor of a homogeneously magnetized general ellipsoid (Stoner, 1945; Osborn, 1945).

2.7.3 Estimation of errors.

Since the magnetic cells may be floating only tens of microns above the microscope slide, the assumption of a distant fluid boundary is almost certainly violated and we have to ask by how much we underestimate the true C when using the limit case expression for $s_{max} \to \infty$. To begin with, we consider a cell of spherical geometry as this case can be treated algebraically. For a sphere with radius $a \equiv a_1 = a_2 = a_3$, expression (2.6) evaluates to

$$P(\sigma_{max}) = \frac{1}{a^3} \int_0^{\sigma_{max}} \frac{d\sigma}{(1+\sigma)^{5/2}} = \frac{2}{3a^3}\left[1 - \frac{1}{(1+\sigma_{max})^{3/2}}\right] \tag{2.8}$$

where $\sigma_{max} = s_{max}/a^2$. From equation (2.7) we can express b, the radius of the boundary shell related to the integration limit s_{max}, in terms of σ_{max}, i.e., $b^2 = a^2(1 + \sigma_{max})$, and recast equation (2.8) into

$$P(a,b) = \frac{2}{3}\left(\frac{1}{a^3} - \frac{1}{b^3}\right) \tag{2.9}$$

Putting equation (2.9) into equation (2.5), we finally have

$$C(a/b) = 8\pi \frac{a^3}{1-(a/b)^3} \tag{2.10}$$

For $b \to \infty$, expression (2.10) converges to $C_\infty = 8\pi a^3$, which is the rotational friction coefficient of an unbounded sphere. As can be seen in figure 2.6, $C(b/a)$ deviates from C_∞, by less than 10% when the clear distance d between cell surface and fluid boundary exceeds 0.6 times the cell diameter. The deviation drops below the 1% level for $d/2a \geq 1.8$. The fast convergence of $C(b/a)$ towards C_∞ is mathematically intuitive from the $(1-(a/b)^3)^{-1}$ dependency (see eq. 2.10). Figure 2.11 shows the proximity effect of a boundary layer on the rotational friction coefficient for a general ellipsoid with semi-axes $a_1 = 1.8, a_2 = 0.9, a_3 = 0.6$. For rotation about the long axis (i=1), the coefficient $C_1(b/a_1)$ deviates by less than 10% from its limit value $C_{1,\infty}$ once the long axis of the fluid boundary is at $b > 1.42a_1$. For rotation about the short axis (i=3), the relative deviation of $C_3(b/a_1)$ from $C_{3,\infty}$ is about twice as large at a given b/a_1 ratio compared to rotation about the short axis. This is due to the fact that rotation about a short axis means that the long axis is in the equatorial (rotation) plane and therefore is closer to the fluid boundary than the intermediate axis is during rotation about the long axis.

Because the estimated magnetic moment μ is proportional to C_i, a possible underestimation of the distance of the fluid boundary from the cell implies an underestimation of μ. Likewise, the viscosity measurement was done on the pure buffer solution before it was added to the suspension of cells, while debris from the dissociation procedure is likely to slightly enhance the actual viscosity of the fluid in which the isolated cells are immersed. Hence, both effects have the same tendency. Therefore, our estimates of μ are rather on the conservative side. The remaining source of error is the determination of the cell dimensions under the light microscope, which is diffraction limited. The optically determined uncertainty in the cell axis is estimated to be 0.5μm in the focal plane and 1μm in the focal depth, both of which is small compared to the typical cell dimensions of 10 μm.

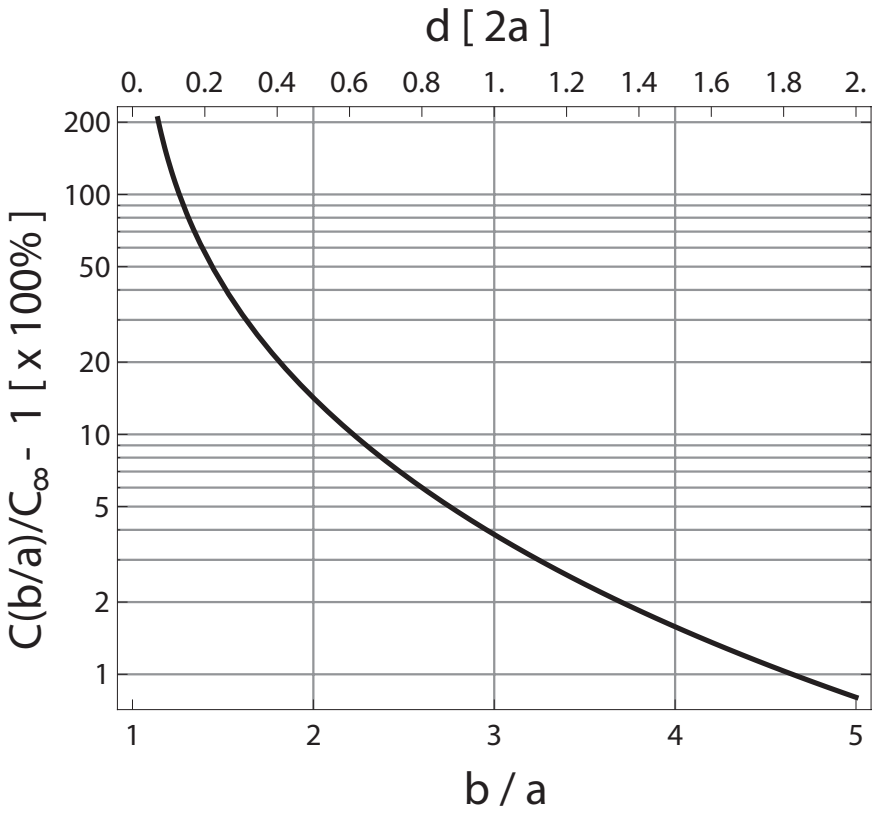

Figure 2.6: Influence of the distance of the fluid boundary from the surface of a spherical cell on the rotational friction coefficient C. The relative deviation (in percent) of C(b/a) from C_∞ is plotted as a function of the ratio of the fluid boundary radius, b to the radius of the sphere, a, (bottom axis) and in terms of the clear distance d between the sphere and fluid boundary, relative to the diameter $2a$ of the sphere (top axis).

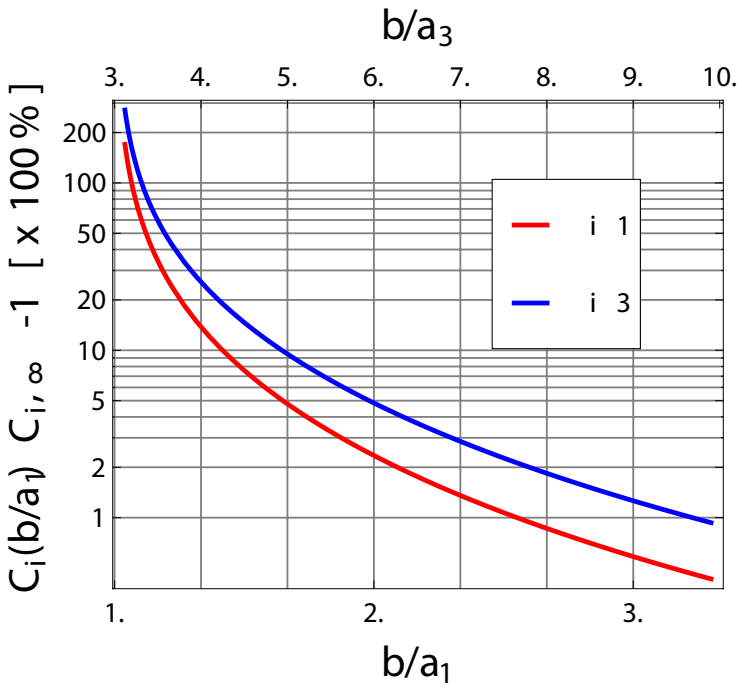

Figure 2.7: Influence of the distance of the fluid boundary from the surface of an ellipsoidal cell on the rotational friction coefficients C_1 and C_3. (C_2 is very close to C_3 and therefore omitted here). The relative deviation (in percent) of the $C_i(b/a_1)$ from the respective limit values $C_{\infty,i}$ is plotted as a function of the ratio of the fluid boundary radius, b, to the long semiaxis of the ellipsoid, a_1, (bottom axis) and to its short semi-axis, a_3 (with a_1=1.8, a_2=0.9, a_3=0.6).

2.7.4 Differential Rotation.

This scenario applies to the case of a magnetic inclusion that is not mechanically coupled to the cell membrane, but viscously suspended in the cytoplasm. When spinning at angular frequency ω_a due to a rotating external magnetic field, the magnetic inclusion transmits shear stress to the cell membrane through the viscosity of the cytoplasm. The shear stress in turn sets the cell membrane in rotation, albeit at a rate $\omega_b < \omega_a$. The differential rotation $\omega_a - \omega_b$ can be calculated algebraically for the geometrically simple case of a spherical inclusion of radius b, located in the center of a spherical cell membrane of radius b. The cell membrane now defines the fluid boundary for the inclusion, so that the viscous resistance

coefficient of the inclusion is given by equation (2.10). Since the fluid boundary rotates at rate ω_b, the couple acting on the inclusion by the fluid volume within $a < r < b$ is given by

$$N_a = -8\pi\eta_{cp}\frac{a^3b^3}{b^3 - a^3}(\omega_a - \omega_b) \tag{2.11}$$

where η_{cp} is the viscosity of the cytoplasm. The couple acting on the rotating cell membrane by the external fluid of viscosity η is

$$N_b = -8\pi\eta b^3\omega_b \tag{2.12}$$

and conversely, the couple needed to produce rotational motion of the cell membrane is $-N_b$, which is provided by the rotational motion of the inner fluid. By balancing the couples, we obtain the rotation rate of the cell relative to that of the inclusion as

$$\frac{\omega_b}{\omega_a} = \frac{\eta_{cp}/\eta}{\eta_{cp}/\eta + (b/a)^3 - 1} \tag{2.13}$$

The viscosity contrast η_{cp}/η can be regarded as coupling strength. As seen in figure 2.8, a cell membrane of diameter 10 μm enclosing a 1 μm sized magnetic inclusion ($b/a = 10$) rotates at a distinctly lower rate than the inclusion does, even for a viscosity contrast as high as 100.

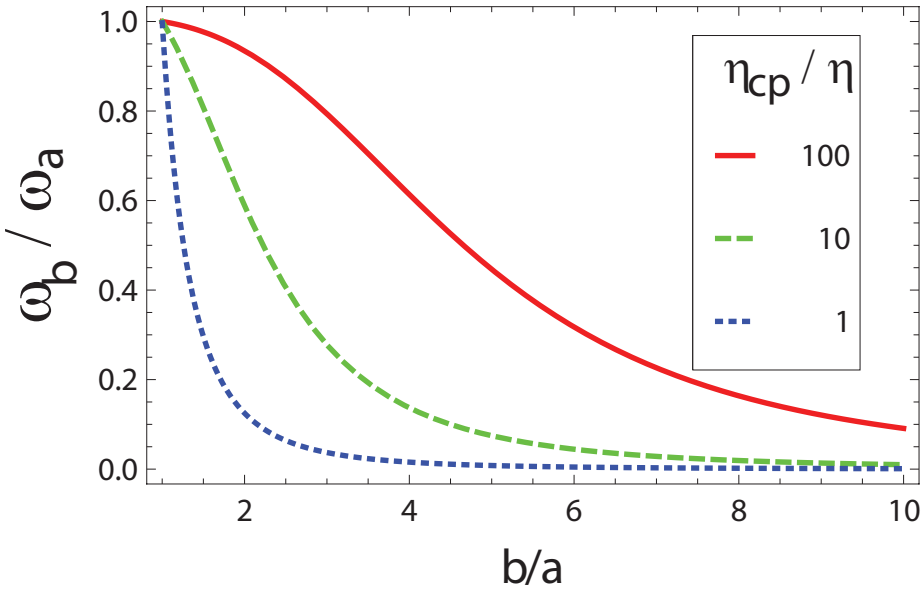

Figure 2.8: Differential rotation for a magnetic inclusion (radius a) in a cell of radius b, according to equation (2.13).

2.7.5 Induced Magnetization

A cell may have also induced magnetization in addition to remanent magnetization, in which case its magnetic susceptibility must be anisotropic in order for the external magnetic field to produce a torque on the induced magnetization. The torque due to anisotropic magnetic susceptibility is given by

$$N_{ind} = \frac{1}{2}\triangle\chi B^2 V sin(2\psi) \tag{2.14}$$

(in c.g.s, e.g., Shcherbakov and Winklhofer, 2004), where V is the volume containing the anisotropic induced magnetization and is the difference in magnetic susceptibility between maximum and minimum axis of the susceptibility tensor. Incorporation of expression (2.14) into the torque balance (c.f. equation 2.2), yields the following expression

$$\frac{\mu B}{2\pi\eta C}\sin\psi + \frac{1}{2}\frac{\triangle\chi \mathrm{B}^2\mathrm{V}}{2\pi\eta \mathrm{C}}\sin 2(\psi - \delta) = \mathrm{f_B} \tag{2.15}$$

where δ is the orientation of the axis of maximum susceptibility relative to the remanent magnetization axis. Introducing f_{rem}^{max} and f_{ind}^{max} as the critical frequency for the case of remanent-only or induced-only magnetization, respectively, equation (2.15) can be rewritten as

$$f_{rem}^{max} sin\psi + f_{ind}^{max} sin2(\psi - \delta) = f_B \tag{2.16}$$

Maximization of equation (2.16) yields $f_B^{max}(\rho, \delta)$, the maximum frequency of the external field up to which the cell can rotate synchronously with the field, where $\rho = f_{ind}^{max}/f_{rem}^{max}$. Mathematically speaking, the two most important solutions to equation 2.16 occur for $\delta = \pm\pi/4$:

i) $\delta = +\pi/4$, i.e., induced and remanent torque add up coherently at any field strength:

$$f_B^{max} = f_{rem}^{max} + f_{ind}^{max} \tag{2.17}$$

ii) $\delta = -\pi/4$, i.e, the remanent torque opposes the induced torque:

$$\frac{f_B^{max}}{f_{rem}^{max}} = \begin{cases} \text{for } \rho \leq \frac{1}{4}, & 1 - \rho \\ \text{for } \rho > \frac{1}{4}, & \frac{1}{4\rho} + \rho \sin\left[2\left(\frac{\pi}{4} + \arcsin\frac{1}{4\rho}\right)\right] \end{cases} \tag{2.18}$$

and the solution has the asymptote $f^{max} = f_{ind}^{max}$ (see also figure 2.9). All other solutions fall between these two boundary lines (see figure 2.9, 2.10). Specifically for $\delta = \pm\pi/2$ and $\delta = 0$, the solution is:

$$\frac{f_B^{max}}{f_{rem}^{max}} = \sqrt{1 - \alpha^2}(1 + 2\alpha\rho) \qquad \text{with} \qquad \alpha = \frac{-1 + \sqrt{1 + 32\rho^2}}{8\rho}$$

Importantly, all solutions have unit slope for large values of ρ, so that $f_B^{max}(\rho \gg 1)_\alpha B^2$, that is the maximum frequency increases quadratically with applied field intensity B.

Finally, the case $\delta = \pi/2$ deserves closer examination. Consider a magnetic inclusion whose dipole is dominated by magnetic remanence. On approaching the critical frequency f_{rem}^{max}, the lag angle $\psi = (\varphi - \vartheta)$ of the remanence vector with respect to the external magnetic field vector (see equation 2.4 approaches $\pi/2$. A Stoner-Wohlfarth particle (Stoner and Wohlfarth, 1948) has the maximum susceptibility axis perpendicular to the easy axis (easy axis is coaxial with the remanence vector), and therefore at lag angle $\pi/2$, the axis of maximum susceptibility is parallel

to the applied field. The susceptibility $\chi_\perp$ of a Stoner-Wohlfarth particle perpendicular to its remanence is given by $1/(N_a - N_b)$, where N_a and N_b are the demagnetizing factors along the hard and easy direction, respectively. From the Stoner-Wohlfarth expression for the switching field,

$$H_c = (N_a - N_b)M_s \quad \sim \quad M_s/\chi_\perp \tag{2.19}$$

we can estimate $\chi_\perp$ when the switching field is known. Assuming a typical switching field of H_c∼240 Oe (24 mT) for magnetite particles with saturation magnetization ∼480 G (480 kA/m), we obtain $\chi_\perp$∼2 [G/Oe], and find that the induced magnetization in a 20 Oe field is only ∼40 G compared to 480 G for the saturation magnetization (that is, its corresponding ρ value is 1/24). Even for $\chi_\perp$∼12 (H_c∼40 Oe), the induced magnetization magnetization in a 20 Oe field is less than half of the magnetic remanence (ρ∼1/4).

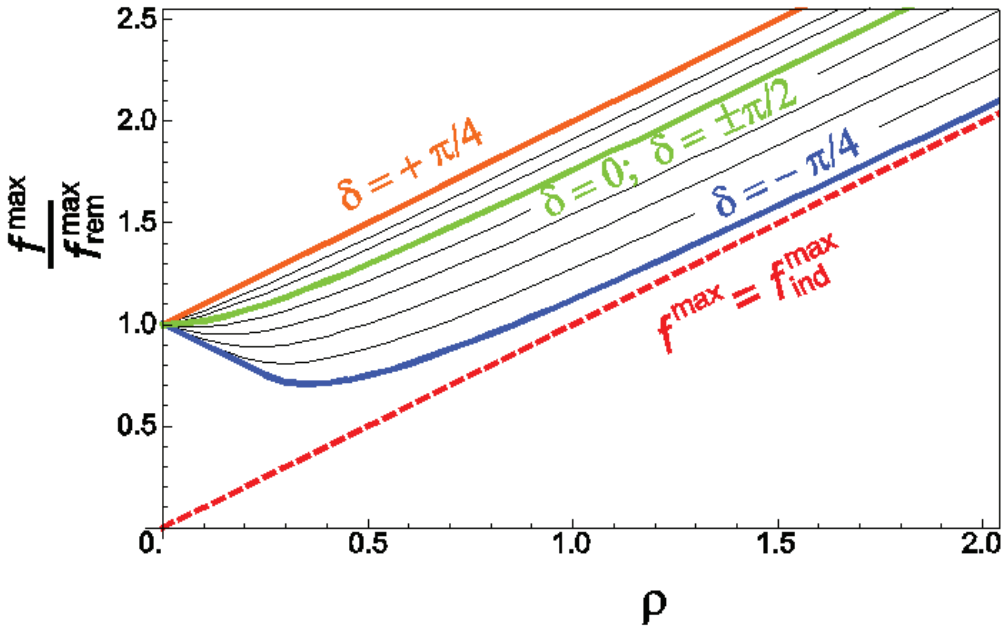

Figure 2.9: Maximum rotation frequency $f_B^{max}(\rho;\delta)$ in units of f_{rem}^{max} as a function of induced-to-remanent ratio $\rho = f_{ind}^{max}/f_{rem}^{max}$ for various angles δ between remanent magnetization and axis of maximum susceptibility. The curves for $\delta = \pi/4$ (orange) and $\delta = -\pi/4$ (blue) form an envelope to all other curves. For $0 \leq \delta \leq \pi/2$, the curves are monotonous, with the green curve demarcating the boundary to non-monotonous behavior. The dashed red line defines an asymptote to the blue curve.

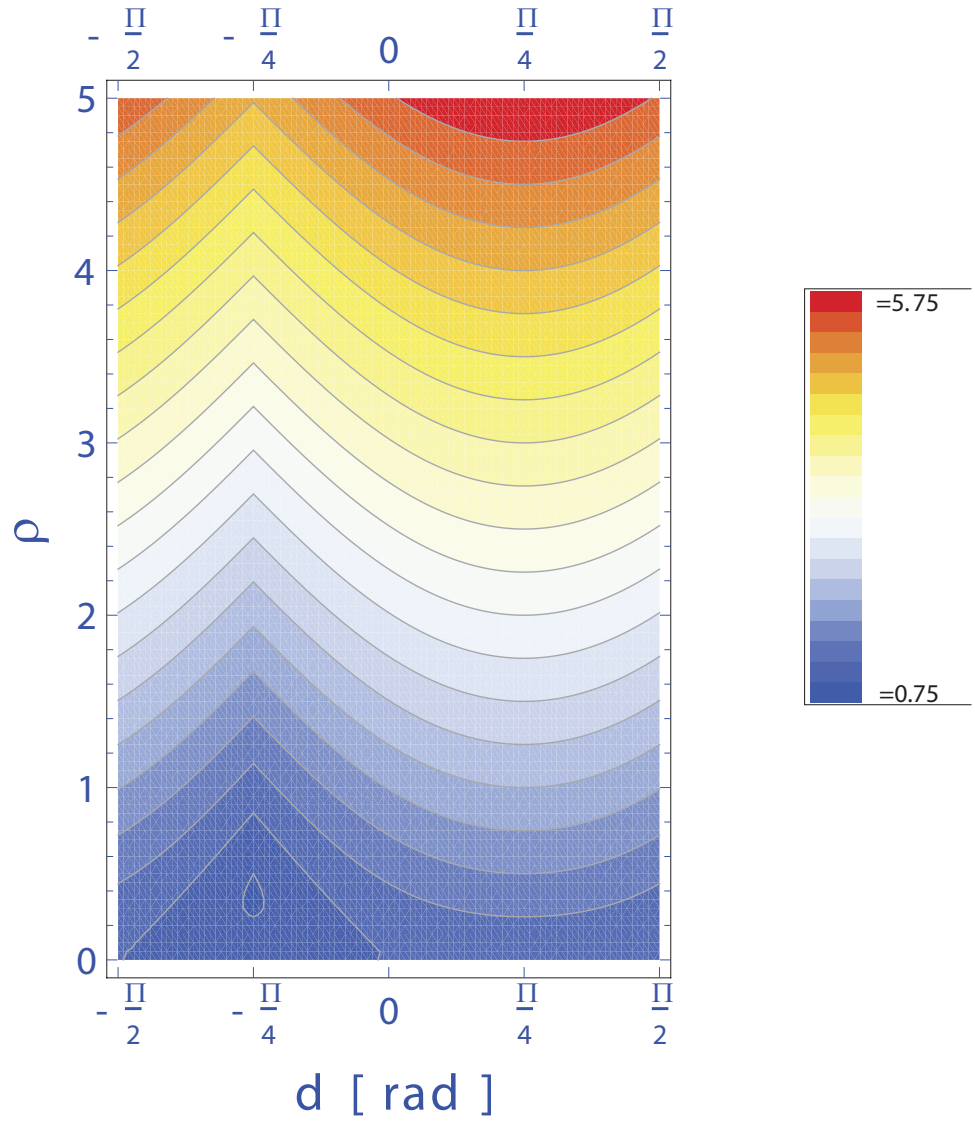

Figure 2.10: Maximum frequency $f_B^{max}(\rho;\delta)/f_{rem}^{max}$ as a function of both induced-to-remanent ratio $\rho = f_{ind}^{max}/f_{rem}^{max}$ and angle δ.

Figure 2.11: Reflected-light images and scanning-electron micrographs of the magnetic cell shown in figure 2.3.
A) Widefield reflectance, imaged with a Zeiss Epiplan 40x (0.85 NA) objective, with focus on the highly reflective object (arrow). The object extending vertically on the left hand side is a cell that was identified as magnetic by its rotational motion in a rotating magnetic field. After transfer of the cell to another cover slip, the cell membrane lost integrity and the cell lost most of its cytoplasm (light flat object to the right of the cell)
B) Wide-field reflectance, imaged with a Nikon 100x (0.9 NA) objective, with focus on the cell surface. The highly reflective object (red arrow) is visible too.
C) Scanning electron image produced with backscattered electrons (incident electron energy was 15 kV). Brightness depends strongly on atomic number. The brightest domain (red arrow) in this micrograph occurs exactly where the reflective objects are located in A, B and where elemental analysis (c.f. EDX in D) shows a strong iron peak. This is the only region in the sample that strongly backscatters electrons and has detectable iron. This comparison demonstrates that the light-reflecting objects are iron-rich and carry the magnetism of the cell.
D) Energy-dispersive X-ray (EDX) analysis of the region in C) that strongly backscatters electrons (15 keV incident electron energy). The two lines marked by arrows are diagnostic for iron. Bin size is 0.02 keV.
E) Scanning electron micrograph (incident electron energy 15 kV) produced with secondary electrons, emitted from very shallow depths (within 10 nm of the sample surface at most). The arrow points to the area that strongly backscatters electrons in C), but is rather inconspicuous in secondary electron imaging and therefore not a surface feature.
F) The region of interest in E) (blue box) was scanned at higher magnification at the same voltage as in E) and only shows topographic features but no material contrast. This demonstrates that the iron-rich regions are intracellular inclusions, not surface features.

Figure 2.11

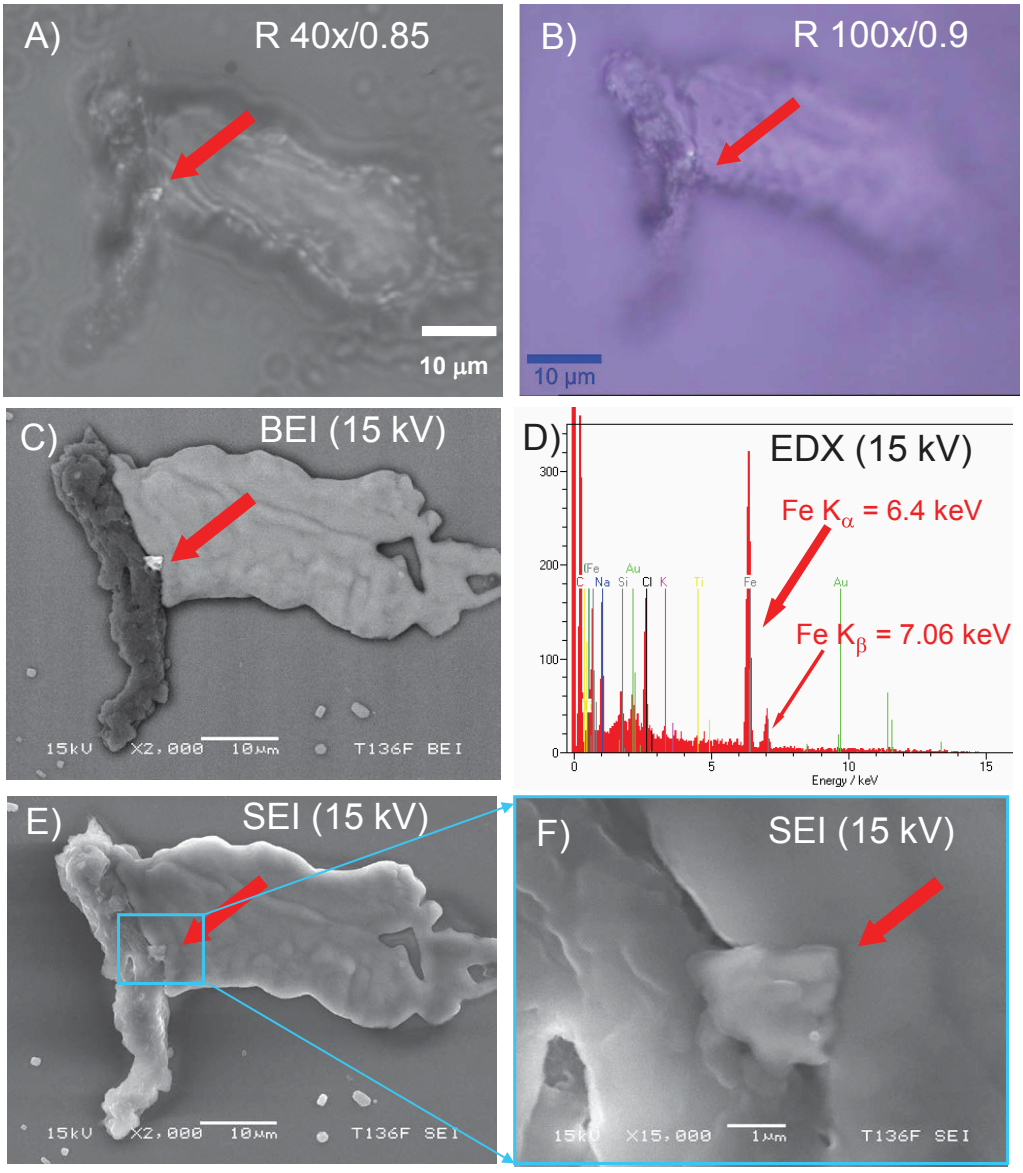
A)
R 40x/0.85
10 µm
B)
R 100x/0.9
10 µm
C)
BEI (15 kV)
15kV X2,000 10µm T136F BEI
D)
EDX (15 kV)
Fe Kα = 6.4 keV
Fe Kβ = 7.06 keV
Energy / keV
E)
SEI (15 kV)
15kV X2,000 10µm T136F SEI
F)
SEI (15 kV)
15kV X15,000 1µm T136F SEI

Table 2.1: Experimentally determined critical frequencies and cellular magnetic moments. Column #: number indicates the individual fish from which a given magnetic cell was derived; letters A, B, or C are used to distinguish among cells from the same individual. Column a, b, c: principal semi-axes of the cell; rotation is about the c-axis. Column C_c: frictional coefficient for rotation about semi-axis c. Columns f_j, H_j, μ_j: j-th measurement of critical frequency at a given rotating magnetic field setting (frequency f_j amplitude H_j [0.1 mT = 1 Oe]), and resulting dipole moment. The magnetic moment is given in 1 fAm^2 (10-15 Am^2), or 10^{-12} G cm^3 = 1 pemu (e.m.u. = electromagnetic units) in cgs units. The μ_j (H_j) for each cell are plotted in figure 2.4. Scatter in the μ_j (H_j) values for a given particle is due to the fact that the magnetic moment is not exactly parallel to one of the principal axes of the cell.

#	a; b; c [µm]	C_c [10^{-15} m^3]	f_1[Hz] H_1[mT] μ_1[fAm^2]	f_2[Hz] H_2[mT] μ_2[fAm^2]	f_3[Hz] H_3[mT] μ_3[fAm^2]	f_4[Hz] H_4[mT] μ_4[fAm^2]	f_5[Hz] H_5[mT] μ_5[fAm^2]	f_6[Hz] H_6[mT] μ_6[fAm^2]	f_7[Hz] H_7[mT] μ_7[fAm^2]
1A	6; 7; 6	6.6	1.2 2.0 25.0	0.55 1.0 22.9	1.5 2.6 24.0	1.9 3.2 24.7			
1B	9; 7.5; 8	14.0	0.77 2.0 33.8	0.4 1.0 35.1	1.0 2.6 33.8	1.3 3.2 35.7	0.8 2.0 35.1		
2A	10; 7; 7	14.2	0.66 2.0 29.5	0.34 1.0 30.4	0.9 2.6 31.0	1.55 3.2 43.4			
2B	6; 6; 7	6.0	0.31 2.6 4.5	0.21 2.0 3.9	0.01 1.0 0.4	0.31 3.2 3.6	0.27 2.6 3.9		
2C	11; 9.5; 8	23.7	1.12 2.0 83.2	0.67 1.0 99.6	1.6 2.6 91.5	1.96 3.2 91.0	1.12 2.0 83.2		
3	5; 4; 4	2.2	4.0 2.0 27.2	1.82 1.0 24.8	0.8 0.4 27.2	5 2.6 26.2			
4	7; 4.5; 5	4.6	0.2 2.6 2.2	0.3 3.2 2.7	0.15 2.0 2.2				
5	8.5; 8; 8	13.9	0.45 3.0 13.1	0.32 2.1 13.3	0.19 1.5 11.0				
6	10; 6; 6	11.7	0.45 2.1 15.7	0.26 1.5 12.7	0.66 3.0 16.1	0.3 1.5 14.6	0.49 2.1 17.1		
7A	14.5; 6.5; 6.5	25.8	0.51 2.1 39.4	1.03 3.0 26.2	0.45 1.5 22.9				
7B	9; 6.5; 6.5	10.9	0.5 2.1 16.2	0.29 1.5 13.2	0.71 3.0 16.1	0.51 2.1 16.6	0.3 1.5 13.6		
7C	3; 15; 8.5	26.0	1.61 3.0 87.7	0.8 1.5 87.1	1.16 2.1 90.2	0.4 0.9 72.6			
8	9.5; 5; 6	9.4	1.6 2.1 45.2	1.2 1.5 47.4	0.74 0.9 48.8	0.22 0.3 43.5	2.8 3.0 55.3	1.75 2.1 49.4	1.26 1.5 49.8

3

Sub-micrometer-scale mapping of magnetite crystals and sulfur globules in magnetic bacteria using confocal Raman micro-spectrometry.

by Stephan H.K. Eder, Alexander M. Gigler, Marianne Hanzlik and Michael Winklhofer

3.1 Abstract

The ferromagnetic mineral magnetite (Fe_3O_4) is found as biomineralization product in magnetotactic microorganisms and a diverse range of animals. Here we demonstrate that confocal laser scanning Raman microscopy can be used to image chains of magnetite crystals in magnetotactic bacteria, even though magnetite is a poor Raman scatterer and occurs in typical grain sizes of only 50-100 nm, well below the diffraction-limited optical resolution. When using low laser power (< 0.25 mW) to prevent laser induced damage of magnetite and long integration times (1 sec), we can identify and map magnetite by its characteristic Raman shifts (665, 535, 303

cm^{-1}) against a large autofluorescence background in our natural magnetic bacteria samples, consisting of uncultured vibrios and cells of *Candidatus Magnetobacterium bavaricum* (Nitrospira). Greigite, as it is produced in some magnetotactic bacteria, could be ruled out by its characteristic Raman shifts (key lines: 253 and 351 cm^{-1}). In the obtained spectra from the bacteria, cyclo-octasulfur (S_8: 467, 219, 151 cm^{-1}) can be identified as the predominant compound in intracellular sulfur globules. S_8 has not been reported in the Nitrospirae phylum, but is likely to be used as energy source. Phosphorous-rich intracellular accumulations in magnetic vibrios are found to be dominated by orthophosphate. The Raman spectral signature of cytochrome is well expressed and due its allocation to lippids it can be used for label-free live-cell imaging of plasma membranes.

3.2 Introduction

The ferrimagnetic mineral magnetite (stoichiometric formula Fe_3O_4) is found as biomineralization product in magnetotactic microorganisms such as bacteria (Frankel *et al.*, 1979), algae (Torres de Araujo *et al.*, 1986), protozoans (Bazylinski *et al.*, 2000), and a diverse range of animals, e.g., molluscs (Lowenstam, 1962), teleost fish (Walker *et al.*, 1984; Eder *et al.*, 2012), birds (Hanzlik *et al.*, 2000). In magnetotactic microorganisms, typically a dozen of intracellular magnetite crystals, with 35-100 nm particle size each, are arranged in the form of one or several chains, imparting a magnetic dipole moment to the cell body (for recent reviews, see Komeili, 2012; Faivre and Schüler, 2008). The chains are mechanically linked to the cytoplasmic membrane, so that the magnetic torque due to an external magnetic field acting on the chain can be directly transmitted to the cell body, thereby aligning the swimming cell with the external magnetic field. The advantage of swimming along magnetic field lines, a behavior referred to as magnetotaxis, is not fully understood yet, since key aspects of the ecology and metabolism of these microorganisms remain to be elucidated.

The role of magnetite in animals is only partly understood. It is likely to be involved in mediating a magnetic sense in animals, at least in salmon and homing pigeons, as indicated by the fact that magnetite found in various nerve tissues of these animals occurs in the magnetic single domain grain size range (Walcott *et al.*, 1979; Walker *et al.*, 1984; Eder *et al.*, 2012) just like in magnetic bacteria. In contrast, magnetite in chiton teeth serves as hardening agent (Lowenstam, 1962) and occurs in particles sizes of ~ 200 nm,

above the single domain threshold size (Kirschvink and Lowenstam, 1979). The origin and role of nanoparticulate magnetite (< 10nm) in pathological human brain tissue (Quintana *et al.*, 2004; Brem *et al.*, 2006) is unknown.

Since biomineralized magnetite always occurs in grain sizes well below the optical diffraction limit, electron microscopical techniques are the usual method of choice for detection and imaging of intracellular magnetite. Scanning transmission X-ray microscopy (STXM) with X-ray spot sizes down to 30 nm has been used to image bacterial magnetosome chains and map the magnetic polarity along the chain (Lam *et al.*, 2010). However, as a synchrotron-based method, STXM is far from becoming a routine technique. The magnetic dipole pattern due to a magnetosome chain can also be imaged with magnetic force microscopy (Proksch *et al.*, 1995; Suzuki *et al.*, 1998; Diebel *et al.*, 2000) provided that the chain is close to the surface of the sample, which should be sufficiently smooth to avoid topographic artifacts.

Here we demonstrate that confocal laser scanning Raman spectroscopy is an effective tool for both detecting and imaging intracellular magnetite crystals with grain sizes of typically 100 nm, well below the optical resolution limit. In essence, the effective resolution is enhanced by first acquiring Raman spectra on a grid with mesh width 100 nm and then by filtering the spectra for the specific Raman lines of magnetite. Laser Raman microscopy has been used to detect biomineralized magnetite *in situ* (Lee *et al.*, 1998; Watanabe *et al.*, 2009), but to our knowledge not for imaging the intracellular distribution of magnetite. Confocal laser scanning microscopy in reflectance mode (Walker *et al.*, 1997) or transmission mode (Lins and Farina, 2004) has been used to image chains of magnetosomes, without rendering compositional information, however. Since magnetosomes can also be made of the ferromagnetic thiospinel greigite (Fe_3S_4) (Farina *et al.*, 1990; Mann *et al.*, 1990; Posfai *et al.*, 1998), the compositional information matters, too. For our proof-of-principle study, we select two types of magnetic bacteria that contain magnetite crystals with typical length dimension 100 nm, *Candidatus M. bavaricum* (M.bav) and uncultured magnetic vibrios from lake sediments. In the *vibrios*, the magnetite crystals are arranged in the form of a single-strand magnetosome chain consisting of 10 to 20 crystals. In contrast, the large, rod-shaped cells of M.bav contain up to 1000 magnetite crystals (magnetosomes), arranged in multi-strand bundles of chains along the axis of the cell body (Vali *et al.*, 1987; Spring *et al.*, 1993; Hanzlik *et al.*, 1996, 2002; Pan *et al.*, 2005; Jogler *et al.*, 2010, 2011). M.bav with its peculiar chain morphology and phylogenetic affiliation to the Nitrospirae phylum has long been considered an exotic representative

of the group of magnetic bacteria, but meanwhile magnetic bacteria with chain morphologies similar to those in M.bav have been reported worldwide (Lam *et al.*, 2010; Isambert *et al.*, 2007; Li *et al.*, 2010; Lefevre *et al.*, 2011).

Apart from magnetosome chains, other intracellular accumulations of inorganic compounds in magnetic bacteria may be phosphorous containing granules and/or sulfur globules (Keim *et al.*, 2005). Bacteria in general accumulate inorganic phosphorous-compounds in the form of ortho-, poly-, or pyrophosphate in intracellular granules (Docampo, 2006). At least three different forms of sulfur - i.e., polysulfanes, cyclo-octasulfur S_8, and polythionates - have been revealed in bacterial sulfur globules using X-ray absorption near-edge spectroscopy (Pickering *et al.*, 2001; Prange *et al.*, 2002) or Raman spectroscopy (Pasteris *et al.*, 2001; Himmel *et al.*, 2009). S_8 so far has only been identified in the Proteobacteria (Dahl and Prange, 2006), but to our knowledge not in the Nitrospirae phylum. In M.bav, elemental sulfur has been suggested to be the main constituent of sulfur globules based on their solubility in methanol (Spring *et al.*, 1993), but the exact allotrope remains unknown. Using the Raman reference spectra of sulfur allotropes compiled by Eckert and Steudel (2003), we will here determine the nature of the sulfur allotrope in M.bav.

3.3 Materials and Methods

Magnetotactic bacteria were extracted from lake sediments collected from Lake Chiemsee. For purification, a drop of sediment is placed onto a microscope slide next to a drop of water. Applying an external magnetic field, one can guide the magnetic bacteria from the sediment to the clear water drop. The cells eventually collect at the edge of the water drop and stay firmly adhered to the microscope slide once the water has dried up. Cells were not prepared with biological fixatives in order to avoid additional fluorescence, which reduces the efficiency of Raman detection of inorganic intracellular compounds. The preparation of the samples was done immediately before the Raman analysis.

In order to obtain a clean Raman reference spectrum for greigite, we hydrothermally synthesized greigite from iron(III)-chloride, thiourea, and formic acid, closely following the protocol described in Chang *et al.* (2007), and recorded with the setup described below from a single greigite crystal with a laser power of 0.2 mW and 10 accumulations with 5 sec integration time each.

Confocal Raman microscopy was performed with an alpha 300R (WITec GmbH, Ulm, Germany). The excitation wavelength was 532 nm (2ω-Nd:YAG solid state laser). The laser power was adjusted to very low values (0.17 mW to 0.25 mW) in order to prevent oxidization of the magnetosomes from magnetite to hematite (e.g., Faria and Vena, 1997; Shebanova and Lazor, 2003b,a; Hanesch, 2009; Lübbe *et al.*, 2010; Li *et al.*, 2012) and to preserve the molecular structure of sulfur (Pasteris *et al.*, 2001). A high numerical aperture (NA=0.9, 100x) air objective was used in order to efficiently collect scattered light from the confocal points.

For confocal imaging and compositional mapping, the core of a multimode fibre served as a pinhole with diameter 50 μm, leading to an axial resolution of $\sim$ 1 μm and a voxel volume of 0.1 μm^3. The piezo-controlled scanning stage with the sample was stepped in intervals of 0.1 μm in both x- and y-direction in order to avoid spatial aliasing. At each confocal point, a Raman spectrum was acquired for 10 sec, spanning the wavenumber range 0 - 3800 cm^{-1}, with 600 mm^{-1} grating. With the low laser power used, such long acquisition times are necessary to identify characteristic peaks of inorganic inclusions against the highly fluorescent background due to the organic material. The Rayleigh peak region (0 - 50 cm^{-1}) was strongly suppressed with a low-pass filter. The spectrometer was calibrated using a Si-wafer (520 cm^{-1}). Spikes due to cosmic rays were removed using the de-spiking option in the software. From characteristic Raman lines (and combinations thereof) identified in measured spectra, we produced compositional maps showing the intensity of these lines at each pixel after background subtraction. On the basis of a threshold-intensity criterion, the intensity-encoded color brightness was adjusted in such a way that only meaningful occurrences of a particular compound are illustrated, while all non-meaningful occurrences remain black. Sum spectra were be obtained by first selecting a specific set of lines, and then by averaging the spectra over those regions that exclusively contain this set of lines.

For scanning-electron microscopy (performed after Raman analysis) with a JSM5900LV (JEOL, Japan), the sample was plasma coated with a few atomic layers of gold. The acceleration voltage was 12 kV so as to be able to excite iron K lines (6.40 keV and 7.06 keV for K_α and $K_{\beta 1}$, respectively). Elemental analysis was done by energy-dispersive X-ray (EDX) analysis at 12 kV (Röntec, Germany).

3.4 Results

Figure 3.1 shows five typical Raman spectra of our magnetic bacteria sample (figure 3.2), recorded at single voxels at 1 sec acquisition time each (figure 3.1A and B) or represented as sum spectra (figure 3.1E-F). While the background is dominated by autofluorescence from organic compounds, one can see a number of distinct lines superimposed. The triplet of lines at 303, 535, and 665 cm^{-1} corresponds to stoichiometric Fe_3O_4 (at 193, 306, 538, 668 cm^{-1}) (Shebanova and Lazor, 2003a). In most Raman studies on magnetite, the line at 193 cm^{-1} is not reported and in our spectra of vibrio and M.bav cells it is not clearly detectable. However, this line appears significantly in the single spectrum of the coccus cell (not mapped, see figure 3.4). The key lines of greigite (253 and 351 cm^{-1}, see figure 3.3) are not detectable in any of observed cells. On the compositional map for magnetite (figure 3.2G), one can clearly recognize linear structures of magnetite in all M.bav cells and also in a vibrio cell (compare figure 3.2G feature a with figure 3.2A). The vibrios in our sediment samples have a single-strand magnetosome chain composed of relatively thick (60-70 nm) magnetosomes (e.g., see figure 1 in Hanzlik *et al.*, 2002), which when in the focal plane generate a larger scatter volume in the voxel analysed compared to the smaller magnetosomes ($\sim$40 nm thin) of M.bav. However, magnetite chains cannot be seen in all vibroid cells in this particular preparation, which we ascribe to the narrow depth range of the confocal imaging technique, which would not resolve magnetite chains lying slightly above or below the focal plane. In contrast, M.bav contains between two and five multi-strand-chains of magnetosomes, so that the probability of having a scattering strand of magnetosomes in the focal plane is higher. Under the SEM, with an acceleration voltage of 12 keV, the Fe K_α line in the EDX spectra was barely, but not significantly detectable in those spots where we expected magnetosomes. At 12 keV, the X-ray emitting volume is of the order of 1 μm^3, while the sub-volume of magnetosomes is less than 10^{-2} μm^3 and therefore is at the EDX detection limit. To reduce the excitation volume, lower acceleration voltages (e.g. 2.2 kV) have to be used, in which case magnetite chains below the surface can be mapped by Fe L_α ($\sim$0.7 keV) (e.g. see Friedmann *et al.*, 2001; Jogler *et al.*, 2011).

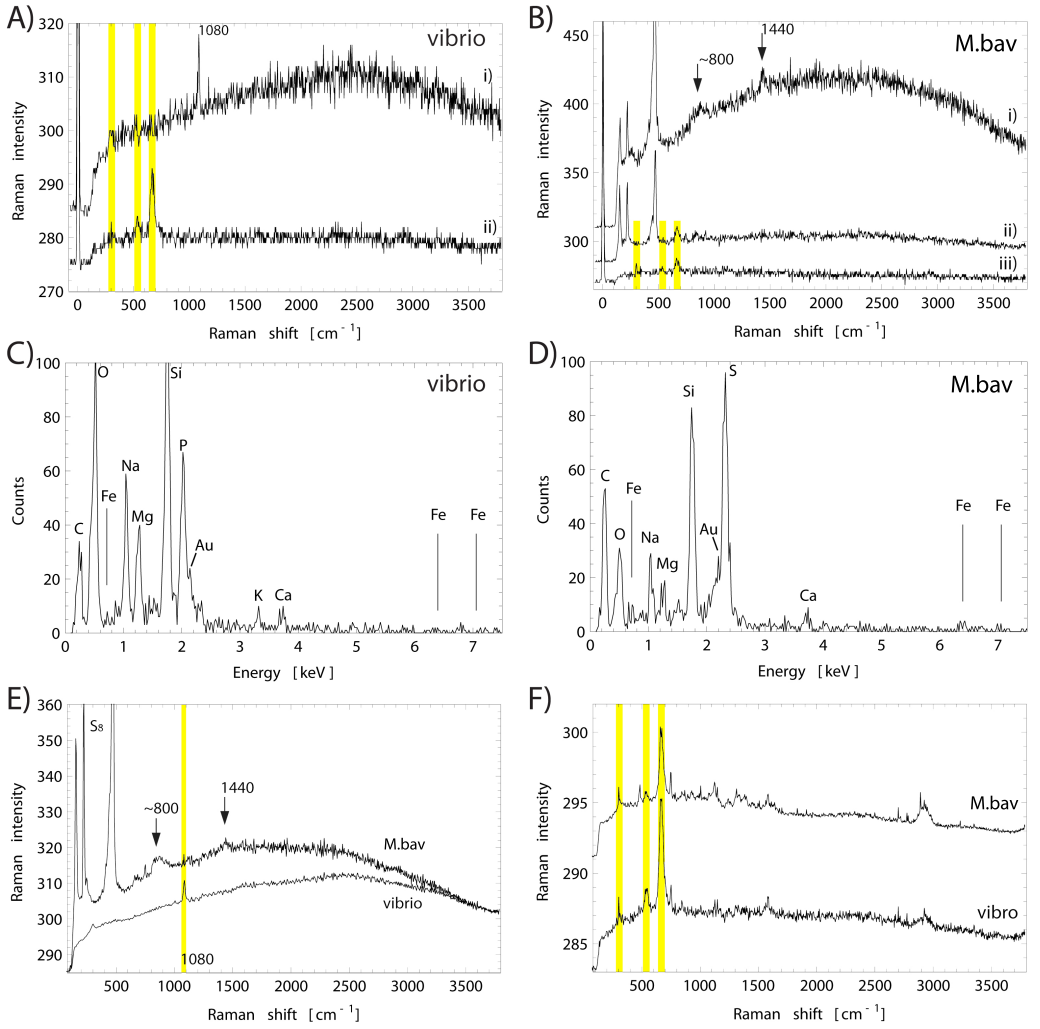

Figure 3.1: Typical Raman spectra of magnetic bacteria recorded at a single-pixel (∼400nm size), as marked in figure 3.2 (white open boxes). **A)** vibrio: (i) intracellular phosphorous reservoir (box in figure 3.2F) with a sharp line at 1080 cm^{-1}, characteristic of orthophosphate. (ii) Magnetosome chain (box *a* in figure 3.2G), with the three characteristic lines of magnetite at 665, 535, and 303 cm^{-1} (yellow bars). **B)** M.bav (i) intracellular sulfur globules (box *a* in figure 3.2C), dominated by S8 rings (467, 219, 151 cm^{-1}); arrow shows broad band (∼800 cm^{-1}) assigned to two-phonon peak of S_8. The line at 1440 cm^{-1} is typical of fatty acids. (ii) Magnetite (yellow bars) in cells with sulfur globules (box *b* in figure 3.2C). (iii) Magnetite in cells without sulfur globules (box *b* in figure 3.2G). **C)** EDX-spectrum of magnetic vibrio, dominated by phosphorous, while iron is not detectable. The Si line is due to the microscope slide. **D)** EDX-spectrum of M.bav. Sulfur is clearly present, while iron is only just detectable. **E, F)** 'Sum spectra' obtained by averaging over those regions that exclusively produce Raman lines of sulfur in M.bav (E, upper graph), of orthophosphate in vibrio (E, lower graph), and of magnetite in M.bav (F, upper graph) and in vibrio (F, lower graph).

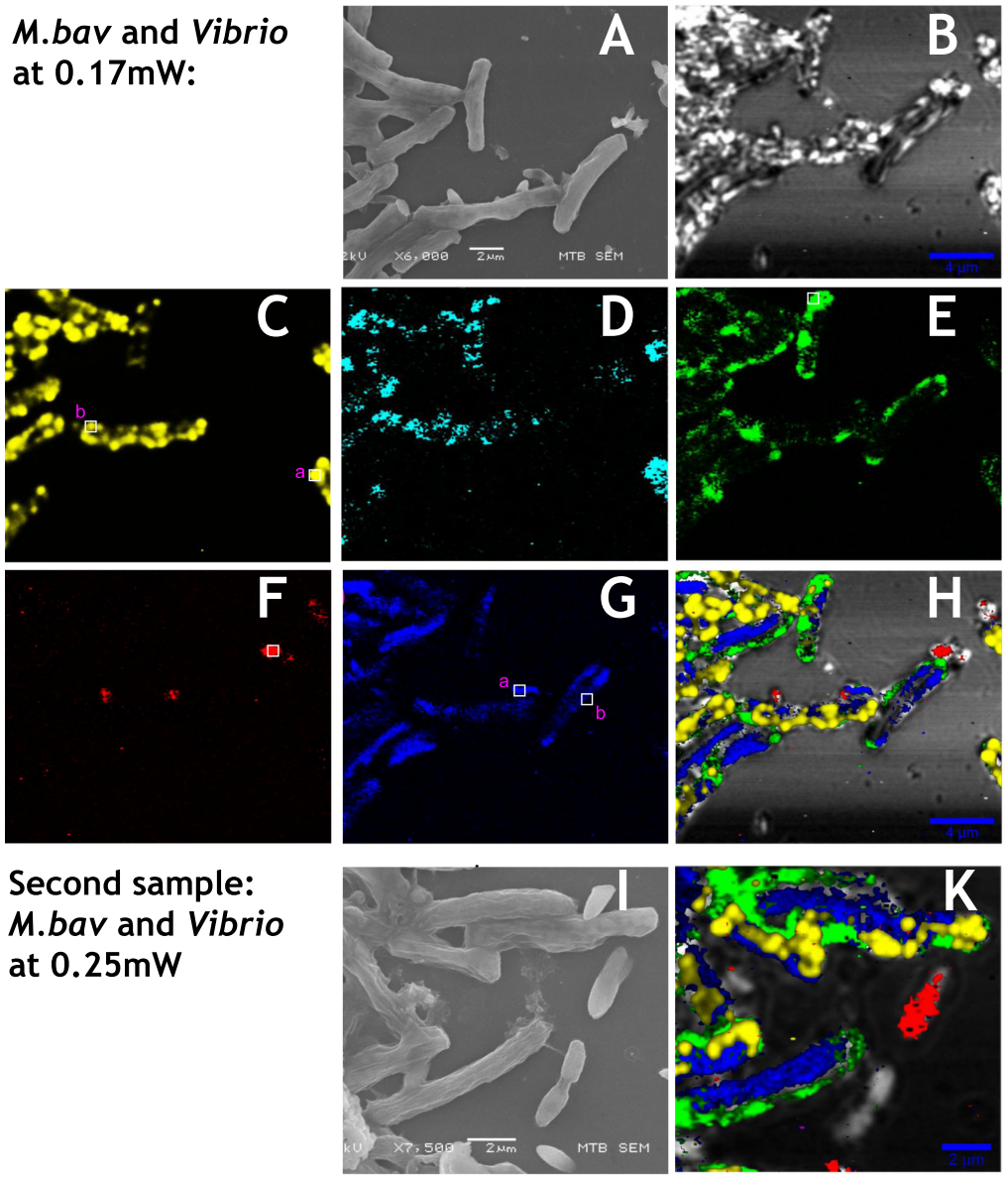

Figure 3.2: Bacteria sample excited with 532 nm laser 0.17 mW shows 6-10 μm long cylindrical rods (M.bav) and less elongated (1-3 μm) vibrios. Sulfur S_8 occurs in the form of globules, while magnetite forms linear structures (magnetosome chains).
A) SEM. **B)** Confocal reflectance, simulated from intensity at Rayleigh peak. **C)** S_8 map (467, 219, 151 cm^{-1}). **D)** map of 800 to 950 cm^{-1} band, see also figure 3.1Bi and 3.1E upper graph). **E)** map of 747 cm^{-1}, cytochrome c in resonance, allocated at the cell outlines. **F)** map of orthophosphate (1080 cm^{-1}, P-O stretching mode), **G)** map of magnetite (665, 535, 303 cm^{-1}). **H)** composite map of B, C, E, F, G.
The second sample is qualitatively similar to the first sample, excited with 532nm laser 0.25 mW: **I)** SEM. **K)** composite map as in H.

The EDX spectrum of the vibroid bacterium shows a pronounced phosphorous peak (at 2.0 keV). Phosphorous in bacteria is typically stored in acidocalcisomes in the form of orthophosphate (Pi), pyrophosphate (PPi), or polyphosphate (poly P) (Docampo, 2006). The characteristic Raman shifts of neither poly P ($\sim$700 and $\sim$1170 cm^{-1}, de Jager and Heyns, 1998; Majed and Gu, 2010) nor PPi (1022 cm^{-1} Majed *et al.*, 2009) ($\sim$ 1050 cm^{-1} Cornilsen, 1984; Chen *et al.*, 2009) are detectable in the Raman spectrum of the vibroid bacterium (figure 3.1C). However, we can identify a sharp peak at $\sim$1080 cm^{-1}, which we assign to the P=O symmetric stretching mode of PO_2 (Preston and Adams, 1979; Okabayashi *et al.*, 1982). The 874 cm^{-1} line due to symmetric stretching of $P(OH)_2$ is not detectable. Thus, the main constituent of the intracellular phosphorous reservoirs in the vibroid is orthophosphate, the most stable phosphate.

A distinct sulfur peak (2.3 keV) is seen in the EDX spectrum of M.bav, resulting from intracellular sulfur globules. We can identify the chemical nature of sulfur in these globules from the Raman spectrum (figure 3.1B), which shows a triplet of lines at 151, 219, and 465 cm^{-1} ($\pm$ 2 cm^{-1}). These can be uniquely attributed to elemental octatomic sulfur, S_8 (86, 152, 218, 475 cm^{-1}, e.g., Scott *et al.*, 1964), because the two lines at 151 and 219 cm^{-1} represent bending modes characteristic of the S_8 ring. Polymeric sulfur, observed in purple and green sulfur bacteria (Prange *et al.*, 2002) and also suggested to be the form of sulfur in M.bav (Hanzlik *et al.*, 1996), would have lines at 460, 425, 275, and 260 cm^{-1} (Eckert and Steudel, 2003), which however were not detectable in our samples. Characteristic lines of other elemental sulfur allotropes from S_6 to S_{20} (compiled in Eckert and Steudel, 2003) were not detectable either. The asymmetric line peaking at 465 cm^{-1} represents a merger of S-S stretching modes at different Raman shifts within the 410-480 cm^{-1} band. A small but distinct shoulder occurs at 415 cm^{-1}, corresponding to a stretching mode that is Raman inactive in molecular S_8 (Eckert and Steudel, 2003), but active in orthorhombic sufur crystals (α-S_8). This suggests that S_8 in M.bav occurs in condensed structures rather than in the form of isolated molecules. These structures have poor crystallinity as indicated by the width of the asymmetric 465 cm^{-1} line, which is typical of glassy S_8, while α-S_8 crystals would show a distinct line at 434 cm^{-1} of medium intensity (Pasteris *et al.*, 2001). On the S_8 map (figure 3.2C), one can see that some cells of M.bav contain up to 20 intracellular S_8 globules of $\sim$0.5 μm diameter, whereas other cells do not have detectable amounts of S_8. Round reflective features in the Rayleigh map (figure 3.2B, which simulates confocal reflectance qualitatively) are co-localized with S_8 inclusions, while

reflective features with irregular morphology do not correspond to sulfur inclusions but rather to unspecific surface features such as sediment or salt particles.

Besides the Raman active lines of S_8, the M.bav spectrum (figure 3.1C) shows a number of additional lines in the range 800 to 950 cm^{-1} (figure 3.1A, i), which have been reported for crystalline α-S_8 (Eckert and Steudel, 2003) and assigned to combinations of stretching vibrations (two-phonon processes). These are generally much weaker than the characteristic S_8 lines. The assignment of the two-phonon band to crystalline α-S8 is not unique because some organic groups have vibrational modes in this wavenumber range, too (e.g., Williams and Edwards, 1994; De Gelder *et al.*, 2007). Therefore, to find out if the broad band is associated with sulfur at all, we test for co-localization on the respective compositional maps (figure 3.2C and D). We find the broad band to be always associated with S_8, suggesting it is the two-phonon band of sulfur. In any case, the intensity of the two-phonon band is significantly weaker than that of S_8. Associated with the 465 cm^{-1} line and the two-phonon band (800 to 950 cm^{-1}), we find an additional line at 1440 cm^{-1} (figure 3.1A, i) which is more intense than the two-phonon band. It can be attributed to CH_2 scissoring ($\delta(CH_2)$, Schachtschneider and Snyder, 1963; Frank *et al.*, 1995), which is a very strong Raman mode in fatty acid chains (Gaber *et al.*, 1978; De Gelder *et al.*, 2007). Since fatty acids have hydrophobic tails and S_8 is not soluble in water, we tentatively ascribe the 1440 cm^{-1} line that is associated with the sulfur lines to the sulfur globule envelope.

A number of prominent lines (747, 1126, 1312 , 1586 cm^{-1}) are spatially associated with each other and concentrated near the cell envelope (figure 3.2E). These lines appear dominantly also in the single spectrum of a coccoidal cell (magnetotacticum) (figure 3.4).

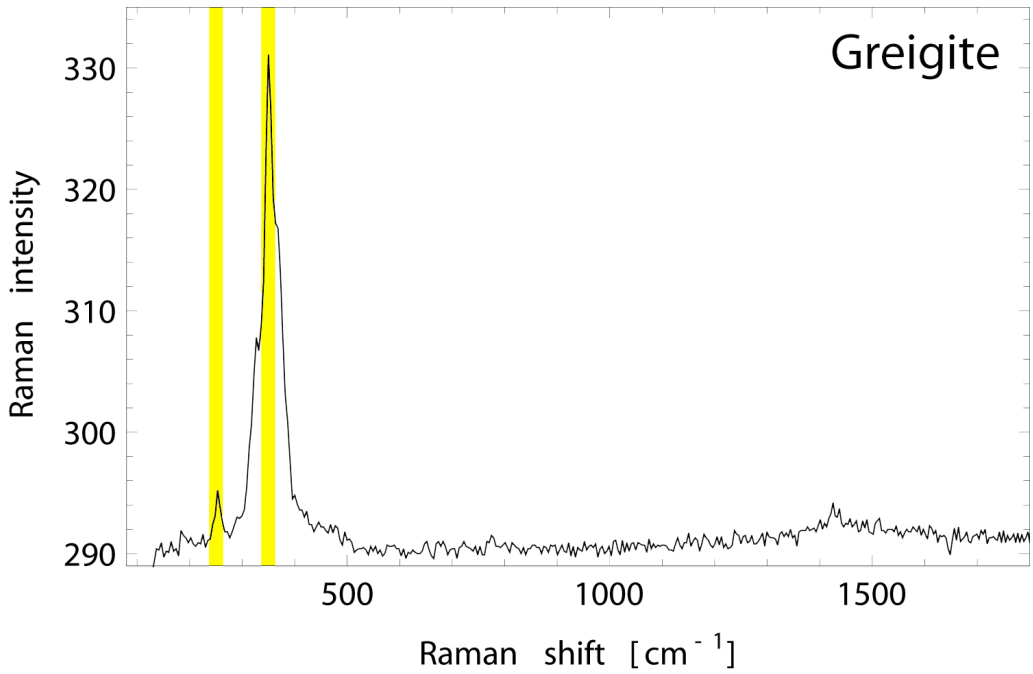

Figure 3.3: Raman spectrum of a single crystal of greigite (∼10 μm grain size). The band at 351 cm^{-1} has a satellite at 327 cm^{-1} and a shoulder at 367 cm^{-1}. Another line is at 253 cm^{-1}. Note the absence of lines at wavenumbers $>$ 500 cm^{-1}, particularly in the 660-670 cm^{-1} range, where magnetite and hematite are active. The 190 cm^{-1} line is just not detectable. The found spectra are consistent with observations from literature (Bourdoiseau *et al.*, 2011).

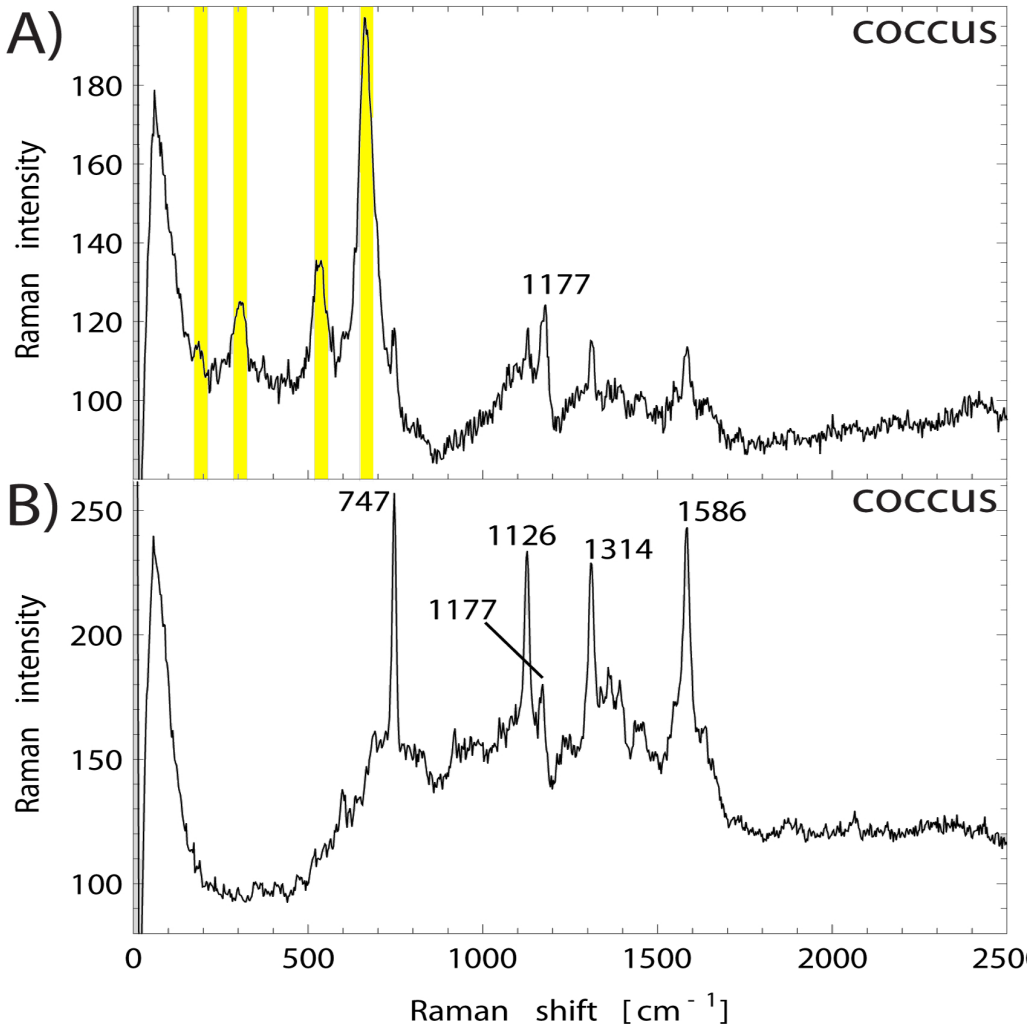

Figure 3.4: Raman single spectra on cocci.
A) Well expressed magnetite lines at 190, 303, 535, 665cm^{-1} (yellow bars).
B) lines of heme group (most likely of cytochrome c) with the lines 747, 1126, 1314, 1586 cm^{-1}.
The line 1177 cm^{-1} is present in A) and B) similarly strong, and therefore is not assigned to cytochrome c.

3.5 Discussion

Detecting a Raman signal from magnetite is an issue by itself. Laser-induced heating oxidizes magnetite to maghaemite and to haematite (Shebanova and Lazor, 2003b). In this study the laser power was adjusted to lowest possible

intensity level (170 - 250 μW), to prevent oxidation damage. The risk of oxidation is potentially higher for a high surface to volume ratio, which is especially the case for sub-100nm crystals as those in magnetotactic bacteria. In our samples of M.bav, vibrios and cocci the magnetosomes did not show Raman lines characteristic of oxidation products of magnetite. Therefore our settings prove adequate for studying the nature of intracellular and extracellular nano-particles made of iron-oxides, without damaging or affecting the initial composition.

It is notable that the magnetosomes in the chains can be detected in the Raman confocal map, even though their particle sizes (60 nm) are far below the optical detection limit (horizontally: $0.61\lambda/\mathrm{NA} = 0.36$ μm) and hence not resolvable in the reflectance confocal image (derived from the Rayleigh peak). This enhanced resolution can be achieved by wavelength-dispersive sampling of reflected light and subsequent energy filtering of the acquired spectra by selecting only those Raman lines that are characteristic of magnetite (303, 535, 665 cm^{-1}). This energy filter applied to all pixels scanned then acts as a spatial filter for magnetite. To take advantage of the enhanced resolution, the step size for scanning needs to be significantly smaller than the optical resolution limit and here was chosen as 0.1 μm. This allows one to locate the position within a resolvable voxel where a specific material occurs with the highest probability. Even though the exact shape and size of the related object cannot be reconstructed, one can assume that its horizontal dimensions are below the optical resolution limit. In contrast, with EDX in SEM, the iron signal of the magnetosomes was to weak to be detectable, because the excited volume by the incident electrons is too big in comparison with the small magnetosomes in this volume.

For the M.bav we observe the chain-structure in which magnetosomes are arranged. Sometimes even more than one distinct chain is visible. This is consistent with the transmission electron micrographs of Hanzlik *et al.* (1996), where M.bav cells show several multistrand chains of magnetosomes.

The presence of iron-oxide and sulfur at the same location includes the possibility that the biomineralized material in the bacteria could be greigite (Fe_3S_4). Greigite magnetosomes have first been found in magnetotactic bacteria from costal lagoons in Brazil (Mann *et al.*, 1990; Farina *et al.*, 1990). To entirely rule out this possibility the scanned spectra of the sample have to show no evidence for the specific spectrum of greigite at the position where sulfur and magnetite overlap. Our reference sample of greigite showed two distinct Raman lines at 253 and 351 cm^{-1}. Further notable is the absence of lines above 500 cm^{-1}, which is an important information that

has not been reported in the literature yet. The dominant line for iron oxides which usually is around 660 - 670 cm^{-1} (mode A1g, see Shebanova and Lazor, 2003b) is not present in the greigite spectrum. Lines of residual sulfur compounds from the synthesis or indications of a possible greigite decomposition into the nonmagnetic pyrite are not visible either. The absence of these lines is an indicator for the purity of the sample. The greigite lines (253 and 351 cm^{-1}) are right in between the characteristic lines of magnetite (303 cm^{-1} and 535 cm^{-1}) and therefore the two minerals are well distinguishable. However, we found no evidence for greigite in the bacteria samples studied here.

The sulfur globules in map 3.2C appear as round intracellular structures, and the magnetite in map 3.2G appears as longish structures in the cell. Both structures seem to overlay accidentally within the confocal thickness of the section. This also suggests that the sulfur and magnetite are separated structures, and therefore the presence of sulfur is no indicator for greigite.

It was known before that M.bav accumulates sulfur in intracellular globules (Spring *et al.*, 1993), but not in what chemical form. Here we have shown that the enriched sulfur species is elemental sulfur in an S_8-ring configuration. The two-phonon effect is co-localized with the sulfur globules (see map 3.2C and 3.2D), which indicates strong interactions between the atoms of different S_8-rings. This suggests a dense accumulation of the S_8-rings. Therefore, it is unlikely that material other than S_8 resides in the globules, which is why they can be considered as pure sulfur storages. It remains unclear by which kind of process the sulfur is enriched in the globules. Importantly, the cells can use the stored sulfur to gain energy for their metabolism (Spring *et al.*, 1993). Thus, the presence or absence of stored sulfur in individual M.bav could quantitatively identify the metabolic state of the cell (some individual cells of M.bav contain S_8, others do not; see map 3.2C).

As with magnetosomes, the intracellular nature of the sulfur inclusions can be clearly identified with confocal Raman microscopy. In contrast, on simple confocal reflectance images it is hard to distinguish between an arbitrary reflection on or in a cell, and the sulfur inclusion. For this reason, Raman spectroscopy is the tool of choice for non-invasive mapping and quantifying of sulfur accumulation in bacteria *in-situ*. It can be applied directly to test for the sulfur content in bacteria designed to reduce the sulfate or sulfite content of water, for example for water quality stabilization in inshore waters or sewage treatment plants. For the vibrio cells, where we identified phosphorous with EDX, the 1080 cm^{-1} indicates orthophosphate

to be the predominant species enriched in intracellular phosphorous granules, and not pyrophosphate nor polyphosphate, which in other bacteria often occur as well (see Docampo, 2006).

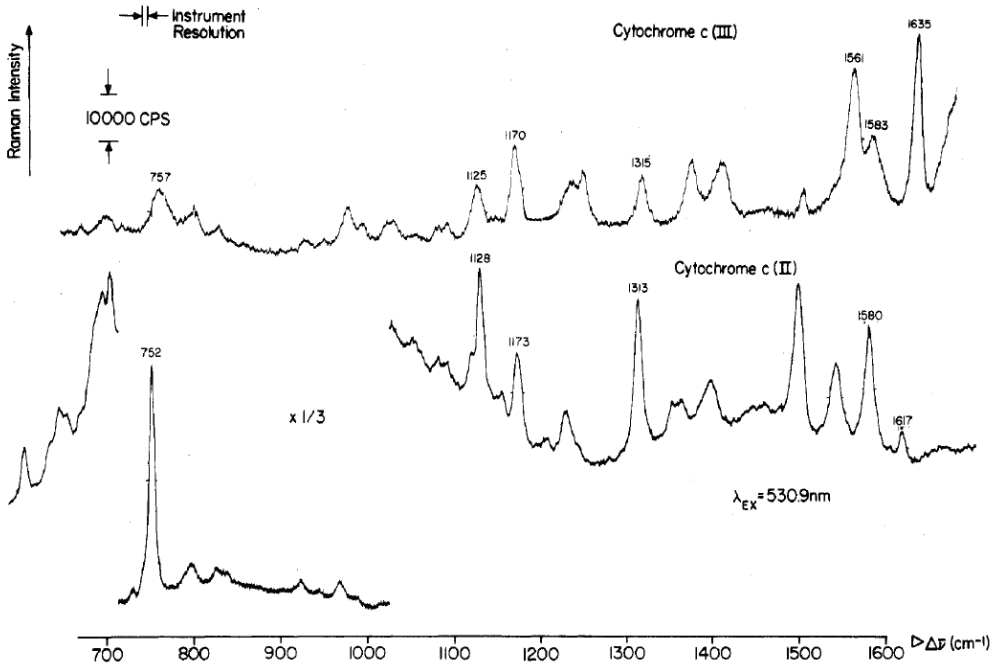

Figure 3.5: adapted from Adar (1978) figure 1: Raman spectra of ferric and ferrous cytochrome c excited with a 530.9 nm laser.

The lines 746, 1126, 1312 and 1586 cm^{-1} in our coccoid magnetic bacteria (figure 3.4) can be attributed the heme group of cytochromes, electron transporters involved in the respiratory chain of organisms. At the example of cytochrome c (figure 3.5), it can be observed that the heme group shows a variety of strong Raman lines, especially when excited with a green wavelength laser (Spiro and Streaks, 1972), in which case resonant Raman (RR) scattering occurs. In the oxidized state of the cytochrome c the following set of most dominant RR lines can be found: 752, 1128, 1313 and 1580 cm^{-1} (Adar, 1978). Of these, the most pronounced is the 752 cm^{-1} line, which is also consistent with our observations. Non-linear aberrations of a few wavelength numbers can be due to the maximum spectral resolution limit of 4-5cm^{-1} (Adar, 1978) and $\sim$3 cm^{-1} in our setup, or due to the different environmental conditions of the cytochrome c: intracellular

dispersed molecules versus synthesized in aqueous solution. The match of the set of 4 Raman lines, however, strongly suggests cytochrome. Cytochromes occur in the periplasmtic space between the two lipid bilayer membranes in prokaryotes, be it in bacteria, be it in mitochondria in eukaryotic cells. Therefore the Raman cytochrome signal defines the outlines of prokaryotes and can be used to specifically map mitochondria (Okada *et al.*, 2012), the only endosymbiotic prokaryotes in the eukaryotic cell with a (ferrous/ferric) heme group.

For excitation of cytochrome, lasers in the band of the fluorescence wavelength of the heme group can be used at very low laser power to still provide a sufficient signal from cytochromes due to RR scattering. This set up drastically reduces laser-induced heating damage and therefore is even suitable for examining living cells.

4

Behavioral experiment: bats use Earth magnetic field for homing.

4.1 Sunset calibration of internal compass

Animals can extract directional information for orientation from different environmental cues (Papi, 1992), such as the sun (Kramer, 1953), the stars (Emlen, 1967) or the Earth's magnetic field (Wiltschko and Wiltschko, 1972, 2006). It was shown that an absolute geographic reference derived by one cue can calibrate a reference of another cue (Bingman *et al.*, 2003). For animal using more than one cue for orientation it is not clear which cue represents the dominant geographical reference (magnetic field: Sandberg *et al.*, 2000; Wiltschko and Wiltschko, 1975) (or sun: Cochran *et al.*, 2004; Muheim *et al.*, 2006a,b).

Greater Mouse-eared bats (*Myotis myotis*) were found to have a magnetic compass for orientation during homing (Holland *et al.*, 2006), which is calibrated by the sun at sunset (Holland *et al.*, 2010). In these experiments the magnetic field was shifted by Helmholtz coils, while the animals were sitting in a jar to view the sunset. The treated bats homed in dark night in another direction than the untreated bats did, which indicates that bats use the magnetic compass at night for homing, and that they calibrate their

compass by the setting sun. Such calibration can be manipulated also by shifting the sun's position with mirrors (Kramer, 1953) or reflective surfaces (Phillips and Waldvogel, 1982).

For sunset calibration the animal observes the direction of sunset as a reference direction, to estimate the displacement with respect to the earth magnetic field direction. The angular displacement between sunset and magnetic North is indicated as the angle β in figure 4.1. The angle α is the angle between the sunset and homing direction. At night, when no other cue is available, the animal can recognize the homing direction by sensing the magnetic North and recognizing the calibrated angle β and the homing angle α. Therefore homing is magnetic North minus α minus β.

An experiment shifting the ambient magnetic field by 90°ccw during sunset-calibration will basically change the calibrated angle β by 90°ccw, and therefore change the homing direction of animals by 90°cw (see figure 4.1b, Chapter 4.3 and Holland *et al.*, 2010). Vice versa changing the sunset direction to 90°cw, by exposing the animal to an artificial sunset in a mirror, would affect the calibrated angle β by 90°cw, and therefore the homing direction by 90°ccw (see figure 4.1b and Chapter 4.2).

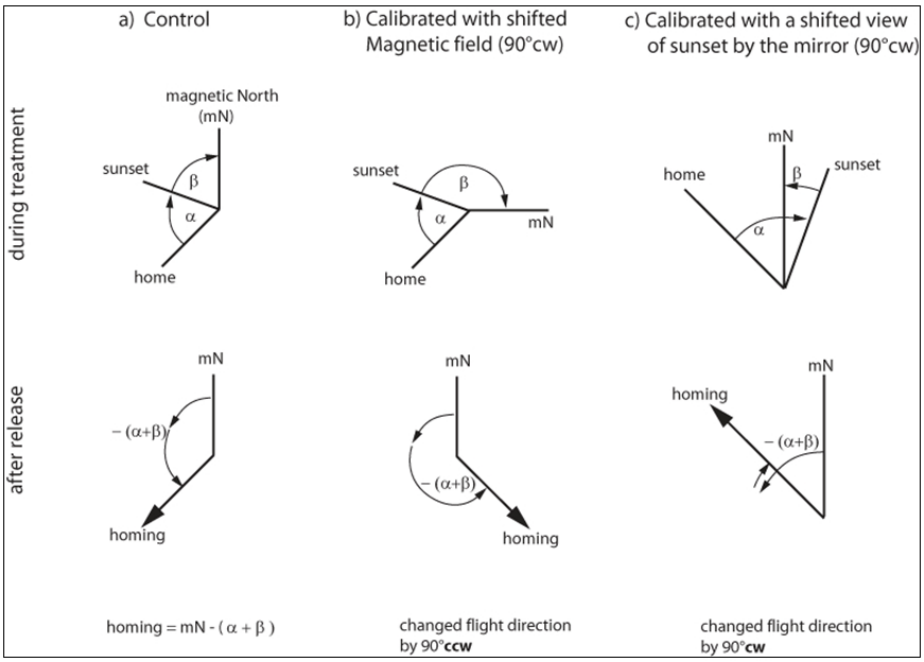

Figure 4.1: Sunset calibration and homing: a) without treatment. b) with a shifted magnetic field. c) with a shifted sunset in a mirror.

4.2 Shifting sunset position in relation to the magnetic field does not reorient homing of greater mouse-eared bats

This Chapter is adapted from a manuscript with allowance of the authors and experimetators: Holland R.A., Eder S. H. K., Borrisov I., Hubancheva A., Baier L., Winklhofer M. and B.M. Siemers.

4.2.1 Abstract

Background:

Bats have recently been shown to use a magnetic compass for homing after experimental displacement by exposing them to a shifted magnetic field at sunset. Unlike in birds it appears that they do not require the pattern of polarized light to calibrate this.

Findings:

To test whether the sun's position provided the crucial calibration reference we conducted a mirror experiment in which bats were exposed to an apparent shift of the setting sun's position before release. The homing performance of test animals and controls turned out to be statistically indistinguishable from one another, which suggests that the suns position did not provide a reference for calibration of magnetic information.

Conclusions:

The failure to find an effect of shifting sunset position suggests that simplest interpretation of the previous experiment i.e. bats use a magnetic compass calibrated by the suns position at sunset, required further evidence before it can be accepted with confidence.

4.2.2 Hypotheses

Recent evidence has indicated that bats use a magnetic compass for orientation during homing (Holland *et al.*, 2006), and that surprisingly for a nocturnal mammal, this appears to be calibrated by sunset cues (Holland *et al.*, 2010). An additional finding of this experiment was that the Perspex

containers in which the bats were exposed to sunset were birifringent, i.e. had a disrupted pattern of polarization. The pattern of polarization at sunset is proposed to be the crucial calibration cue in magnetic compass orientation in birds (Muheim *et al.*, 2006b) but the shift in orientation shown in (Holland *et al.*, 2010) despite a disrupted pattern of polarization argues against this cue being necessary for calibration in bats. This further suggests that it was the suns position that was the crucial cue in the calibration of the magnetic field. Here we attempt to directly test this hypothesis by rotating the position of the sun using a mirror, to see if the bats recalibrate a magnetic compass in the same way as when the magnetic field is rotated at sunset. We also report further analysis of the holding containers used to expose the bats to sunset to quantify the exact nature of the light that the bats had access to.

4.2.3 Methods

(a) Subjects

16 female greater mouse-eared bats (post-lactating or nuliparous adults only) were captured at Orlova Chuka cave, northern Bulgaria (N 43° 35.595' E 025°57.611'), on the night of 25/07/2010. They were brought to Tabachka Bat Research Station (N 43° 36.631'; E 025° 58.366') and were housed for one night under the same conditions as reported in (Holland *et al.*, 2010).

(b) Experimental treatment

On 27/07/10 the bats were transported to the treatment site (N 43°36.453' E 025°58.061') by car one hour before sunset. The bats were transported in cloth capture bags and had no view of the sun either before or during transportation. The treatment site had an unrestricted view of the horizon. Bats were randomly assigned into two equal groups, and were placed in individual Perspex jars with ventilation holes in the bottom. Still in the car, the jars were placed in an opaque plastic box (50 x 30 x 33 cm) which was open at one end. Boxes were closed with a lid and carried from the car to the final position, where the lid was removed. Two bats were placed on the bottom of the box and a shelf was placed above them with another two bats on this. There were 2 "control" boxes and 2 "experimental" boxes. The handler was blind to the treatment condition. The control boxes were placed one on top of the other facing the setting sun at 20:20 h, 26 minutes before civil sunset. The experimental boxes were placed in front of a mirror (200 x

120 cm) which was angled so that it gave a view of the reflected sunset such that it appeared to be shifted 90° clockwise relative to natural sunset (figure 4.2 and 4.3). The box containing the bats was placed such that it left their view restricted only to the mirror. From within the jars in the box mirror bats as well as control bats had about 90° horizontal field of view and only restricted view of the sky above, with a maximum elevation angle of 45°. The bats were left in the boxes at the treatment site until 22:10 when no sign of post sunset glow was visible. Bats were removed from the treatment site by placing a lid over the open side of the box and then placing the box in a vehicle. The bats were removed from their jars inside the vehicle and placed once again in cloth capture bags ready for transport to the release site (N 43° 045.173' E 26° 10.748' 211 m), 24.31 km from the bats' cave with a home direction of 223°. Previous experiments at this site produced different mean orientation directions with different experimental treatments (Holland *et al.*, 2010). Thus we could be certain that a homing response was not merely coincidental with an attraction to some other factor close to this release site. Capture of bats and experiments were conducted under license of the responsible Bulgarian authorities (MOEW Sofia and RIOSV Ruse; permits No. 193/01.04.2009 and No. 205/29.05.2009)

(c) Tracking procedure

To increase homing motivation, the bats were fed > 4 g mealworms and water just prior to release. The release started after 00:00 h. Each bat had a VHF radio transmitter (164 MHz, LB2N, 0.42g, Holohil, Carp, Ontario, Canada) attached to its back using skin glue (Manfred Sauer GMBH Hautkleber, Lobbach, Germany). Bats were released individually and their radio departure bearing was collected using the same procedure as reported in (Holland *et al.*, 2006), the exception that the observer stood on the roof of a Landrover Discovery in this case and the person releasing the bats and taking the vanishing bearings was blind to the treatment condition. Two automatic receivers (Sparrow Systems inc. Champagne-Urbana, Illinois) were placed at the cave prior to the releases and removed on 29/07/10. One was placed in the hall where the Myotis colony typically roosts and a second at the cave entrance. They detected the earliest arrival of the bat registered as an increase in recorded signal strength above the background noise level, and this was used to calculate the homing times of the bats.

(d) Polarized light

The jars are the same as used in (Holland *et al.*, 2006, 2010). Their material support pleochroism but is not polarizing itself. The pleochroism can affect the light only if it has been polarized previously. Typically the sun's polarized light appears at angles of more than 45° from the sun. The experiment was designed that for all bats the view of more than ±45° horizontally and +45° vertically was covered, so that the bats could not see the region of the naturally polarized light. Neither the sun's polarized light can enter, nor the jars can polarize the light. This supports that no polarized or else modified light could get to the bat's eyes, and prevents the experiment to be biased by polarized light.

4.2.4 Results

Sunset calibration

Figure 4.4 shows the vanishing bearings of the control and experimental groups. The control group was significantly oriented (mean vector, 211°, r = 0.765, Rayleigh test, Z = 4.678, p = 0.005, V test, V = 0.743, p < 0.0001), and the home direction (225°) was included in the 95% confidence interval (confidence interval test, p>0.05). The experimental group was more scattered and only marginally significant by Rayleigh test (mean vector, 188°, r = 0.59, Rayleigh test, Z = 2.783, p = 0.057), but significantly oriented by the V test with the home direction as the expected direction (V = 0.47, p = 0.03). However, there was no difference in distribution between groups (Watsons U^2 test, $U^2 = 0.058$, $p > 0.5$), nor in the variance around the mean (variance test, U = 16, p = 0.103). There was no difference in homing success between the two groups (Chi^2 test, $\chi^2 = 5$, p = 0.5). For those bats that homed (4 controls, 5 experimental bats), homing times did not differ between groups (controls, median = 259.5 min. experimentals, median = 275 min. Mann-Whitney U-test, U = 6, p = 0.327).

4.2.5 Conclusions

(a) Sunset calibration

If the bats were using the sun's position at sunset to calibrate the magnetic field for compass use, then the 90° shift of the sun's position clockwise should have made the bats calibrate the magnetic field by presuming that it was

aligned pointing to the West, and thus result in a clockwise rotation of their perception of North relative to actual magnetic North (figure 4.1c and 4.2). We would have expected a clockwise rotation of the experimental group's mean bearing at the release site if this was the case, but no evidence for this was obtained. If anything, the experimental group suggested a slight deflection counter clockwise of controls but this remains speculative, since there was no statistical difference between groups. This experiment thus does not provide support for the hypothesis that calibration of the magnetic field is by the sunset position. It is possible that the bats did not recognize the "mirrored" sun as a real cue and decided not to recalibrate on this night but rely on a previous night's calibration. However, it should be noted that in birds rotations of sun's position, or light from it, using mirrors or reflective surfaces, have been successful in producing rotations in orientation (Kramer, 1953; Phillips and Waldvogel, 1982). It is also possible that some stress in the treatment caused the bats not to calibrate the magnetic field on this occasion. This cannot be ruled out but, although not exactly the same experimental setup, similar stresses were involved in the previous experiments on insectivorous bats that indicated calibration of the magnetic field by sunset cues (Holland *et al.*, 2006, 2010). However, unlike in the previous experiments which indicated sunset calibration (Holland *et al.*, 2006, 2010), the bats had a restricted view of the horizon in the mirror, and a limited view of the sky above them. It is possible this alerted the bats that the sun was not a reliable cue.

(b) Polarized light

The holding containers indicated that these were non polarizing, thus the bats would be unable to sense any polarization pattern produced by the sunset. This supports the conclusion of our previous experiment (Holland *et al.*, 2010) that bats can calibrate the magnetic field without access to this cue. It would, however be interesting to perform experiments similar to those in (Muheim *et al.*, 2006b) in which the pattern of polarization is shifted at sunset, to test whether the polarization pattern can be used if available.

Our results suggest that the interaction between sunset cues and the magnetic field, and possibly other as yet unidentified cues is more flexible than previously supposed. What role sunset cues play in calibration of the compass system of bats must be confirmed by further experiments.

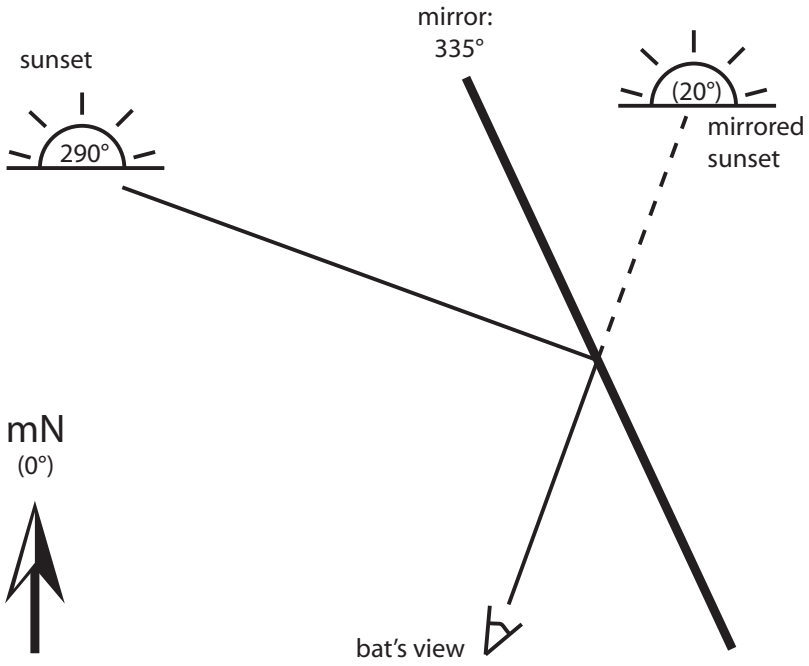

Figure 4.2: Schematic experimental setup for shifting the sunset by 90°.

Figure 4.3: Setup for exposure of bats to a mirrored sunset. The bats are placed in boxes in front of a mirror which deflects the sun rays such that the sunset position appears to be shifted by 90° cw. Their field of view is restricted to the mirror. Due to the breadth of the mirror, the bats have a full view of the (mirrored) sunset and of the (mirrored) post-sunset glow. Thus, the sunset is perceived by the bats at 20° (from mN), whereas the real sun sets at 290°. This setup is expected to affect the calibration, and in consequence also the homing direction (see angle β in figure 4.1)

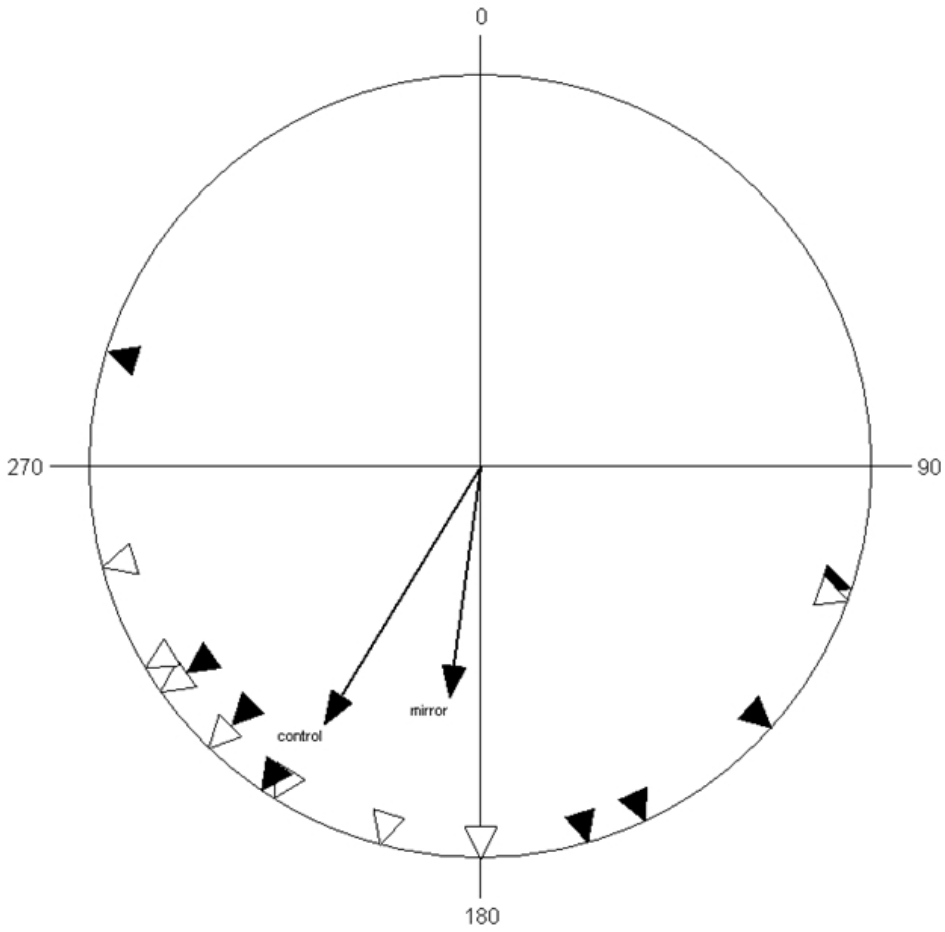

Figure 4.4: Circular diagram of the vanishing bearings of control (open symbols) and experimental (filled symbols) groups. Mean vectors are shown by the arrows and vector lengths are indicated by the length of the arrow relative to the circle (edge of circle = 1). Home direction is indicated by the arrow on the edge of the circle.

4.3 Affecting homing of greater mouse-eared bats by shifting the magnetic field and by treating with RF magnetic fields

The experiments in this chapter 4.2 were designed and conducted by Eder, S. H. K., Holland R.A., Borrisov I., Hubancheva A., Baier L., B.M. Siemers B.M. and M. Winklhofer. The study was funded by Max Planck Society and Human Frontiers Science Program (RGP 28/2007).

4.3.1 Introduction

As described in Chapter 4.1 testing for the magnetic sense in bats can be performed either by shifting visually the sunset, or by shifting the ambient magnetic field during sunset calibration (by using a pair of Helmholtz-coils).

In this experiment the motivation was to first reproduce the findings of Holland *et al.* (2010) with a shifted magnetic field, and then to test for the type of magnetic sense, whether it is based on magnetite or on radical pairs. If the magnetic sense is mediated by radical pairs, it may be disturbed by a radio-frequency magnetic field (RF-field) in the 1 - 10 MHz range. In contrary a magnetite based magnetoreceptor should not be disturbed when the RF-field is on. To study the effect on recalibration of the internal compass of the bats we shifted the ambient magnetic field by 90°. If the RF-field affects the magnetoreceptor, the bats may be confused and do not recalibrate during sunset. We would expect them to be oriented similarly to those which were un-treated and not exposed to a 90° shifted field (i.e. which were just in the normal ambient magnetic field). If they are not affected by the RF-field they should home as the 90° shifted group. Thus in this experiments we have three groups of bats exposed to different treatments. First, the group of untreated bats kept in sham coils during the sunset calibration (control-group); second, the group which is treated with the shifted magnetic field by 90° cw during sunset calibration (DC-group); and third, the group which experiences a 90° shifted magnetic field and additionally treated with an RF-field (RF+DC-group).

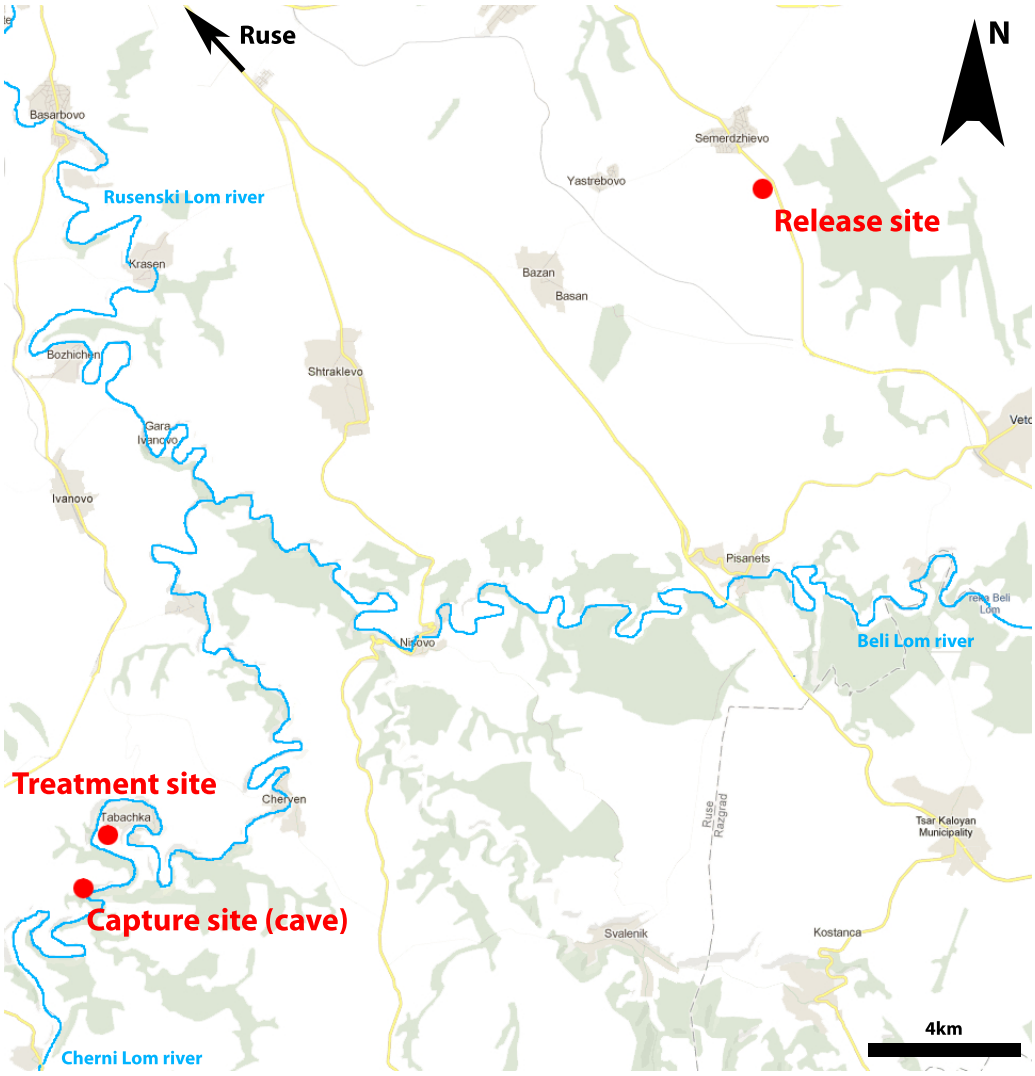

Figure 4.5: Map showing the sites of capture, treatment and release of bats. The control group, without magnetic treatment, is expected to fly towards Southwest from release site to home to their cave, or as Holland *et al.* (2010) showed towards South to reach the close by *Beli Lom* river.

4.3.2 Methods

Six identical coil-setups (with each 2 jars for bats) were placed next to each other, separated by 3 m each. Each setup consists of a pair of oriented Helmholtz coils and an RF-coil mounted concentric to the DC-coils. The coils were oriented with their North-axis 135° clockwise to geomagnetic

North. The DC-field strength was adjusted such that the resulting field in the center of the coils pointed 90° (i.e. towards East), measured with a compass. Due to the geometry the resulting magnetic field has the same field strength as the natural geomagnetic field, and therefore does not affect the natural geomagnetic inclination angle of the location.

The RF coil had a similar diameter as the Helmholtz DC-coil, and were mounted midway between the two coils of the Helmholtz pair. The RF-coils are fed using a Wavetec frequency generator (WT144) and an impedance matched coax cable (Aircell 7, 50 Ω). It is not known at what frequency a possible radical-pair receptor in bats can be disturbed most effectively, and therefore we swept the RF frequency from 1 to 5 MHz, which includes the Larmor frequency of 1.315 MHz at the local ambient magnetic field strength of the area. The RF-field strength was adjusted to 142 nT at 1.315 MHz. Due to the resonance behavior of the RF-Coil, the field strength was strongest at 4.7 MHz (470 nT). These values are sufficient to disturb a radical pair mechanism as shown by Ritz *et al.* (2004) and Thalau *et al.* (2005, 2006). The residual field strength in the sham coils and DC-coils was below detection limit of our oscilloscope (below 4 nT; Picoscope 4224 with Rohde&Schwarz 6 cm loop-B-field-probe) for any frequency excited, thus below 10 nT, not sufficient to disturb the radical pair mechanism as shown by Ritz *et al.* (2009).

The experiment has been performed double blind. The first person handled the bats, which includes placing them in the jars before the sunset calibration, taking them out of the jars afterward, and feeding them before release. This person did not know what specific magnetic treatment each bat was, or will be, exposed to. The second person did have a protocol of which of the coils (DC or RF+DC) will be fed by the supplies. The protocol further implies a random generated routine which defines the order of bats (numbered at their bags), the place of exposure (the coil and position in the coil), and further the order of release. The six coil-setups were identical and all of them were connected to wires. The person with the protocol of the experiment connected the wires to the supplies under a cover, in order to activate only selected coils. This person did never touch a bat, and could not influence the treatment or behavior of the bats. The third person did release the bats and track them (as described in Chapter 4.2) after the order of the protocol. This person did not know which specific magnetic field condition each bat had been exposed to before. The bats were collected before dawn of the experimental day when returning to their cave. Each day we caught 12 bats, which were either post-lactating or non-lactating, and are exposed

to the sunset two in each of the six coil-setups. The experiment at 21.7.2010 has been repeated twice (23.7.10 and 24.7.10).

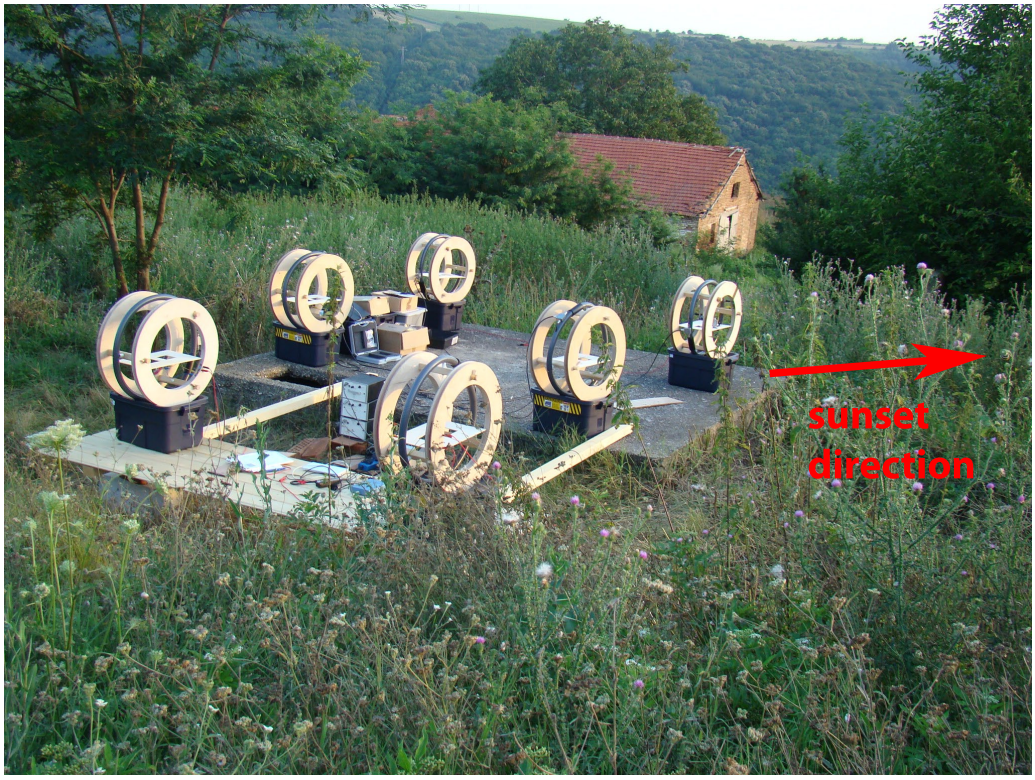

Figure 4.6: Experimental treatment setup: 6 pairs of Helmholtz coils equipped with RF-coils. At each experimental day two coils were not connected (control group), two coils were connected to a DC source in order to shift the magnetic field by 90◦ (DC group) and two coils were connected to DC- and RF-source (RF+DC group).

4.3.3 Results

The vanishing bearings of the bats (see table 4.1 and in figure 4.7) appear to be rather dispersed. Correspondingly short are the calculated mean vectors of each group (see table 4.2). With all vector length of $R < 0.3$ none of the groups flew over the three experimental days in a significant mean-direction (Assuming significance at $p < 0.1$ with $n = 12$ the corresponding vector length is $R > 0.437$, after Gaile and Burt, 1980).

By looking at the three experimental days as individual experiments, the R-values increase. However, significance at $n = 4$ can only be assumed for values of $R > 0.74$ which is not the case for most of the results.

The data plots with the bearing of the bats (figure 4.7) look as if there are different modes involved. Two modes could be imagined opposite to each other at the same axis. Testing for an axial mean, by doubling the angles, showed a better significance for the control-group, and especially for the RF+DC-group (see table 4.4). The DC-group instead decreased its R-value.

	21st				23rd				24th			
Control	2	215	170	160	6	13	264	202	208	116	148	
DC	22	55	172	270	222	96	114	129	300	220	216	207
RF+DC	70	76	110	144	286	283	272	133	293	26	292	204

Table 4.1: Vanishing bearings of the bats (in angular degrees, clockwise positive eastward from geomagnetic North)

	Control	DC	RF+DC
Bearing:	182°	183°	274°
Vector length:	R=0.27	R=0.28	R=0.05

Table 4.2: Mean vectors of vanishing bearings.

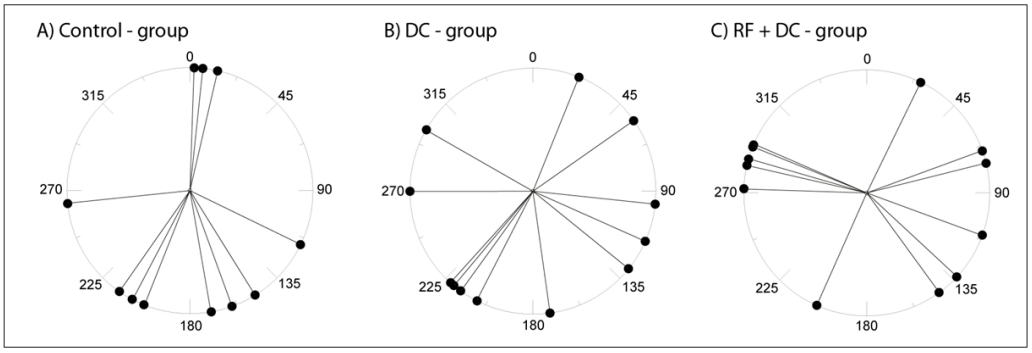

Figure 4.7: Vanishing bearings on a unit circle (0° is magnetic North). A) Control-group without treatment; B) DC-group, treatment with a magnetic field shifted by 90° cw; C) RF+DC-group, treatment with a magnetic field shifted by 90° cw and simultaneous RF-magnetic-field.

Day	Control		DC		RF+DC	
21st:	180°	R=0.44	33°	R=0.15	99°	R=0.87
23rd:	312°	R=0.35	133°	R=0.69	266°	R=0.55
24th:	173°	R=0.79	232°	R=0.81	292°	R=0.49

Table 4.3: Mean vectors of vanishing bearings of the groups in each experimental day.

	Control	DC	RF+DC
Bearing:	184° / 4°	145° / 325°	192° / 12°
Vector length:	R=0.46	R=0.20	R=0.47

Table 4.4: Mean vectors of the bearings taken over all experimental days, assuming an axial (not polar) magnetic behavior. It is calculated by taking the mean over the double angles.

4.3.4 Discussion

Since the direction of the bat-cave is Southwest of the release site, we would expect the control-group to fly off into this direction (∼200°). Yet, in the experiments performed one year earlier (Holland *et al.*, 2010) the bats were observed to head towards the South rather than Southwest. Perhaps they first get to the river close by (Rusenski Lom River), which is their known hunting ground that also provides several caves to hide. From there they can home in back to the cave. The DC-group was expected to fly towards the East, since their calibration was shifted by 90° (see figure 4.1). The RF+DC-group, assuming a magnetite sensor, ideally should be indistinguishable from the DC-group, while assuming a radical pair sensor they should not be able to recalibrate, and therefore use their previous calibration without treatment, and find the right direction (South).

In the ideal case the group mean directions should have a vector length R close to unity, i.e. little dispersion among the individuals of the group. The R values are less than 0.3 (see table 4.2), which is not significant. Taking a closer look at the data we can identify multiple modes in each group. The control group appears bimodal, where most of the bats go South, as expected, and only a group of 3 bats were heading off North. We can divide the DC-group into a mode of Southwest and a mode of East flying bats. The RF+DC-group splits in an East and a West heading group. This multi-modal behavior can be explained by dividing the bats into groups either

with different motivations to fly home, or with different urge to recalibrate with the sunset of treatment.

The motivation to home may be influenced by many factors, such as the (i) wind and weather conditions, (ii) the timing of the release (how many hours after the sunset), (iii) the status of feeding, or also (iv) the presence of predators (such as owls). (v) The urge to recalibrate the internal compass with the sunset of treatment may depend on the number of days that have passed since the last calibration had been performed.

The bats were released after midnight (ii), as in the experiment of 2009 (Holland *et al.*, 2010). Also the status of feeding (iii), which influences the decision to home or to go for another feeding excursion, was equivalent. The bats were fed on average with 5g of mehlworms until their satisfaction, right before release. The presence of predators (iv) cannot be controlled in this field-experiment, however we did not notice any at the release site. Most notably, the wind and weather conditions (i) did significantly differ, according to the experimenters B. Siemers and R. Holland. In 2009 the experiments were conducted 2 weeks earlier in July, when it was dryer and thunderstorm activity was much less. During our experimental days there was a lot of moisture in the air and a thundery atmosphere, although it did not thunderstorm or rain at the treatment- or release-sites. The wind in both experiments was between still and moderate. (The weather during the mirror experiment of chapter 4.2 was dry with much lower thunderstorm activity.) The thundery atmosphere in our experiment could indeed have affected the decision of the bats to find the closest hideout, not getting into the thunderstorm during homing. (v) The urge to recalibrate may be dependent upon the time the bats have spent in captivity. Although it is not known every how many nights they recalibrate, it is conceivable that they recalibrate whenever possible, i.e., when the sunset is not obscured by clouds. In our experiment they have been caught just before dawn when returning to the cave, and released several hours later (between 1 and 4 am at night). In the 2009 experiment, however, the bats have been kept and fed for an additional day when sunset was obscured by clouds at the intended day of release, enhancing their motivation to calibrate their compass on the next day and thus the chances of affecting them by the altered magnetic field. In contrast, the bats of the 2010 experiment (which were released within 8 hours after capture), may well have had a calibration from the night before, and therefore may have remained unaffected by the altered magnetic field conditions. This would cause a divergence of data into two groups, as it is visible e.g. in the DC-group. All but one of them headed towards a southern

or eastern direction, which may indicate that some have been recalibrating under the DC-treatment (going East), and others have not (going South). However, the data of the control-group and of the RF+DC-group do not support this theory.

Interestingly, when looking at each day separately (see table 4.3), the vector lengths are larger compared to the mean vector lengths over the whole three-day span. This of course due to the decrease of samples, but maybe also due to day variations in the motivation of the bats according to outer influences, such as the mentioned points (i) to (v). The group being best oriented in terms of R-value was the RF+DC of the first experimental day (21st). Even though the DC-group had a low R value its direction corresponds to the predicted homing direction, and the RF+DC-group would have homed significantly ($R = 0.87$) in the eastern direction. This is as predicted for a magnetite based magnetoreceptor, insensitive to RF magnetic fields. However, the lack of a negative control and the small number of samples through a single experimental day ($n = 4$) does not allow a clear conclusion to be drawn, to confirm the magnetite based theory.

The experimental day with best R-values through all groups is the 24th. Here the control-group is oriented towards South, while the mean of the DC-group is shifted by 59° clockwise. The RF+DC group (not significant) is shifted by 119° clockwise. From theory, and according to the experiments of Holland *et al.* (2010), the DC-group should be sifted 90° counterclockwise, which is not the case here. This wrongly oriented but significant positive control (DC-group) indicates a bias in the experiment. Since the experiment is almost equally performed as the experiment of Holland *et al.* (2010) there must have been the problem of motivation for homing, as mentioned by the points (i) to (v).

Theoretically, it is possible that bats have magnetoreceptors that are specialized to find the axial direction of the magnetic field lines, but are not able to detect the North direction of them, just like migratory songbirds tested in the lab (Wiltschko and Wiltschko, 1972), and similarly in salmon (Quinn and Brannon, 1982). For the case of an axial sensor the direction of the control-group in our experiment shows significantly the homing-axis (184°) and the RF+DC-group shows significantly the same axis (only 8° cw shifted). This result would agree with the a radical pair magnetoreceptor designed for detecting only axial directions. However, the lack of a significant positive control (DC-group, $R = 0.20$) does not allow the conclusion that bats use a radical pair based magnetic sense.

4.3.5 Conclusions

For the first time, RF experiments in the field have been conducted to test for the involvement of a radical-pair based magnetoreceptor mechanism in the magnetic compass sense. A rigorously double blind experimental protocol has been implemented in order to avoid the possible influence of the experimenter on the outcome. However, unlike the year before and despite the experimental effort, our test animals – greater mouse-eared bats (*Myotis Myotis*) – did not show clear orientations, neither in the testing- nor in the control-groups. Also the analysis of sub-groups and the testing for axial orientation did not show clear results. To explain the fact that the control-bats did not fly significantly in a homing direction, we have to assume that the motivation of the bats to home was not urgently given. The motivation can be influenced by many factors. We assume that the main reason for diverging motivations among individuals were unstable weather conditions. These could have well affected the decision-making process of the bats in favor of hiding in trees or caves close by instead of homing. Moreover, in contrast to the previous experiment, the bats were not kept over two nights in captivity, which could have affected the urge to recalibrate at the treatment sunset.

Therefore, the results suggest that more experiments are needed to find the keys to the motivation of homing.

4.4 Polarization patterns of the bat-jars

The experiments in sections 4.2 and 4.3 opened the question of whether the jars in which bats were exposed to at sunset had a polarization effect, which would influence the calibration of the bats compass at sunset. Birds have been suggested to be able to detect skylight polarization (Muheim *et al.*, 2006b) and use it for orientation. Skylight is significantly polarized in directions at 90° degrees from the sun direction, which results in a band of polarized light across the sky. At sunset this band would be at maximum polarization from North over Zenith to South, while the sun is at the Western horizon. It is the orientation of the polarization band that could serve birds as one cue for orientation (Muheim *et al.*, 2006b).

Holland *et al.* (2010) described the jars to be birefringent. Here we investigated one of theses jars with a polarization microscope (Leitz Orthoplan) and also non-microscopically with polarization optics (two polarization-filters and a white-light source). One polarization filter polarizes the incoming light. The other polarization filter, also referred to as analyzer, can be used to detect the rotation of the polarization plane after transmission of pre-polarized light through a sample.

Without sample, the intensity of the detected light changes from high to low when changing the orientation of the analyzer relative to the polarizer from parallel to perpendicular (figure 4.8a), with extinction at exact perpendicular orientation (crossed Nichols). With the jar sample between polarizer and analyzer, a complex polarization pattern is observed: The intensity is low with crossed Nichols and high under parallel orientation, but between these two extremes we detect blue and red patterns (figure 4.8b).

The measurement without polarizer but with the sample and the analyzer showed that the sample does not polarize light. At any angle of the analyzer, the light had the same bright intensity, so that the jars are non-polarizing (figure 4.8c)

Therefore, the first conclusion is that the jars do not polarize light (compare with figure 4.8c). Thus, there is no bias due to a polarization vision of bats.

Secondly, if bats have polarization vision, and use the band of polarized light instead of the sunset sun-position, they would possibly detect this band (extending from North over Zenith to South) as without the jars. By turning their head, they would not only see it becoming light and dark, but also blue and red in between (compare with figure 4.8b). Since *Myotis* in general are

rather color-blind (Suthers, 1970) the red/blue shift of polarized light is likely to be not detectable for bats, or might appear as a dark/light variation. In any case they would recognize the position of the band correctly and would be able to determine the correct direction of sunset. This is valid for the magnetic field shift experiment in chapter 4.3. However, for the sunset-shift-experiment in chapter 4.2 it indeed would be confusing for the bats to observe the sunset in the North instead of the West when a visible band of polarization were to indicate the sunset in another direction. In the mirror experiment we constrained the bat's view to the mirror and to no more than 45° horizontally and vertically from the sunset position. In the range of 0° to 45° from the sun direction no polarization is detectable. The area of 90° from the sun where the polarization appears at its maximum was not visible for the bats in the sunset-shift-experiment.

We conclude that the pleochroism of the jars is unlikely to have affected the experiments, neither the ones with shifted magnetic field nor with shifted sunset. What is more, to our knowledge it has not been demonstrated conclusively that mammals can detect the polarization of light at all. This is consistent with the findings of the 2009 experiment (Holland *et al.*, 2010), where the bats had unlimited view while sitting in the same jars as used here.

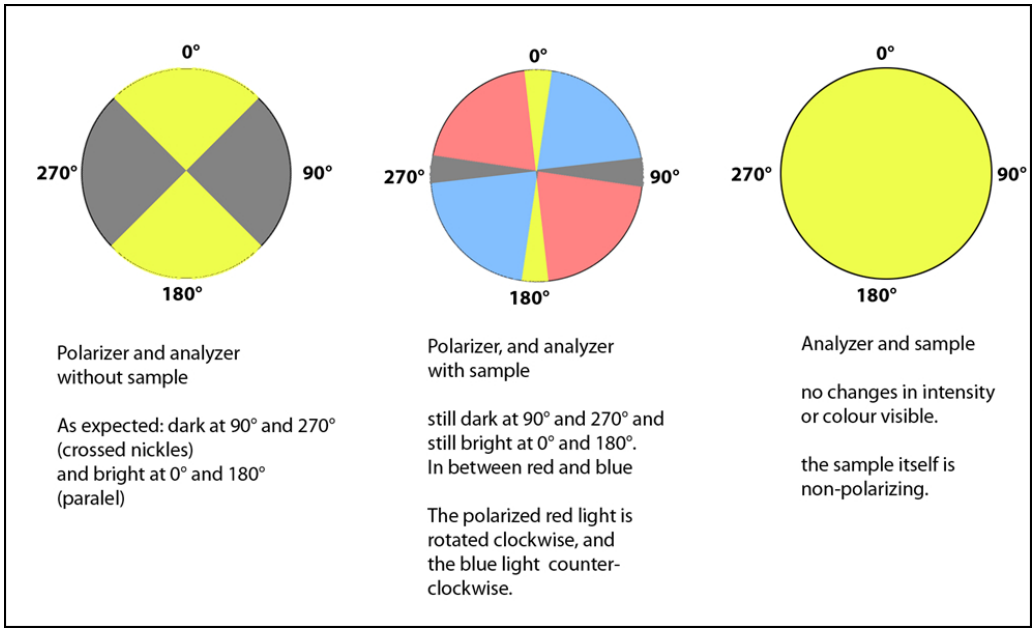

Figure 4.8: Polarization patterns of the bat jars.

5

Magnetic particles in ant antennae.

5.1 Introduction

It has been shown that ants, in particular migratory species such as *Pachycondyla marginata* use the Earth's magnetic field for orientation (Acosta-Avalos *et al.*, 2001). Various tests showed that the most promising part for magnetoreception in ants are the antennae (Acosta-Avalos *et al.*, 1999; Wajnberg *et al.*, 2000, 2004). In a transmission electron microscopy (TEM) study, Oliveira *et al.* (2010) were finally able to find iron-rich crystals in the Johnston's organ in antennae of *Pachycondyla marginata*, and identified by selected area electron diffraction (SAED) the strongly magnetic minerals magnetite and maghemite as well as the relatively weakly magnetic ones goethite and haematite. In principle the magnetic moments of the magnetic crystals in the Earth's magnetic field can produce a mechanical moment that can be transmitted into a neuronal signal via a mechanosensitive structure (Kirschvink and Gould, 1981; Shcherbakov and Winklhofer, 1999; Davila *et al.*, 2003, 2005; Ferreira *et al.*, 2005). The Johnston's organ, which is a mechanosensitive structure, has been suggested to work as a graviceptor or an acceleration receptor (for hearing or flight control) (Sandeman, 1976). With the recent finding of magnetic minerals, the Johnston's organ could serve also as a magnetoreceptor (Oliveira *et al.*, 2010). However, the characteristic magnetic properties of these iron-mineral

deposits have not been determined yet and it remains unclear whether or not the structure meets the basic requirements for magnetoreception. Therefore, the aim of this study is to characterize the magnetism of the deposits. For this purpose we apply magnetic force microscopy (MFM) to the ultrathin section samples examined with TEM before by Oliveira *et al.* (2010) (see figure 5.1).

The MFM technique is a modification of atomic force microscopy in which a magnetic cantilever tip is used to probe magnetic stray fields from the sample scanned (Hartmann *et al.*, 1991). It allows one to resolve magnetic structures at length scales of well below 100 nm. MFM has been successfully applied to visualize magnetic dipoles due to remanent magnetization of magnetosomes in magnetotactic bacteria and in trout (Proksch *et al.*, 1995; Diebel *et al.*, 2000; Suzuki *et al.*, 1998; Gojzewski *et al.*, 2012).

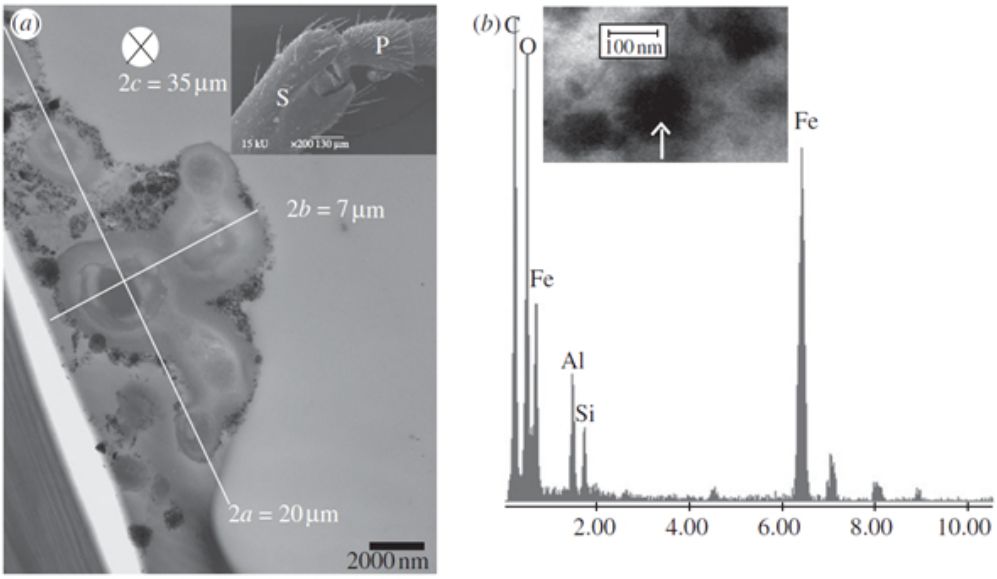

Figure 5.1: from Oliveira *et al.* (2010) fig 5. (a) TEM image of an ultrathin section of the Johnstons organ in ant antennae. The round cell-like structures are surrounded by electron-opaque granules. Inset shows the joint region from which transverse ultrathin sections were made. (b) EDX spectrum (electron dispersive X-ray spectroscopy) of one of the electron-opaque granules, showing an iron-peak. Inset: arrow indicates the area where the EDX was taken.

5.2 Methods

The TEM grids with thin sections on it were observed in an inverted light microscope (Axio observer, Zeiss, Germany), equipped with an Atomic Force Microscopy (AFM) setup (NanoWizard®II, JPK Instruments AG, Germany). At first the AFM was adjusted in intermittent contact mode, where the cantilever is oscillating at its free resonance frequency (∼100kHz) while scanning across the sample. Interactions between the surface atoms and the tip attenuate the oscillation amplitude. Short-ranged Van-der-Waals forces dominate the tip-surface-interaction when the tip is close to the surface. The closer the distance to the surface, the stronger is the attenuation. The height of the cantilever then is dynamically adjusted to a constant level of attenuation, representing a defined separation from the surface topography. The recorded height of the cantilever then represents a topographic map of the sample surface. The amplitude of the cantilever oscillation is a measure of the interaction between the cantilever tip and the surface atoms, and can be seen as the residual height that has not been resolved by the dynamically adjusted cantilever height. To avoid scanning artifacts, the scan parameters were set in a such a way that the cantilever keeps contact with the surface, using the surface-force sensitive oscillation amplitude for control.

We used a cantilever with a non-magnetic tip (NSC15, Mikromasch, Estonia) for AFM and a cantilever with magnetically coated tip for MFM (SC-10-M, SmartTip, Netherlands; magnetized in the field of a strong permanentmagnet). The magnetic tip interacts not only with atomic forces, but also with magnetic forces, resulting in a magnetically modulated surface topography. A map of magnetic forces can be obtained in two different ways: (i) by taking the difference between AFM and MFM derived topography, (ii) by using the "hover-mode" (also referred to as "lift-mode"), in which the MFM cantilever is scanning a line to measure the topographic relief (trace). On the way back over the same line (retrace), the previously recorded topography plus a certain adjustable lift height d defines the retrace height (figure 5.3 a and b). In a constant distance to the surface of for example 10 nm, Van-der-Waals forces are negligible, but the magnetic dipole-forces, decreasing less strongly, are still present (figure 5.3 c).

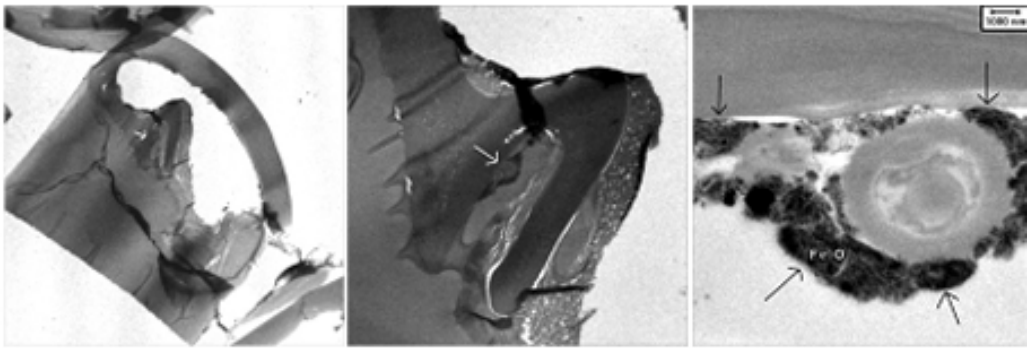

Figure 5.2: (courtesy of Dr. M. Hanzlik) Left: (300x300μm) thin section of ant antenna. White arrow indicates the structure where iron rich crystals were found. Center: (90x90μm) Zoom into the thin section. White arrow as before. Right: (11x11μm) TEM image of cell-like organic structure surrounded with dark granules (black arrows), which were found to be rich in iron and oxygen.

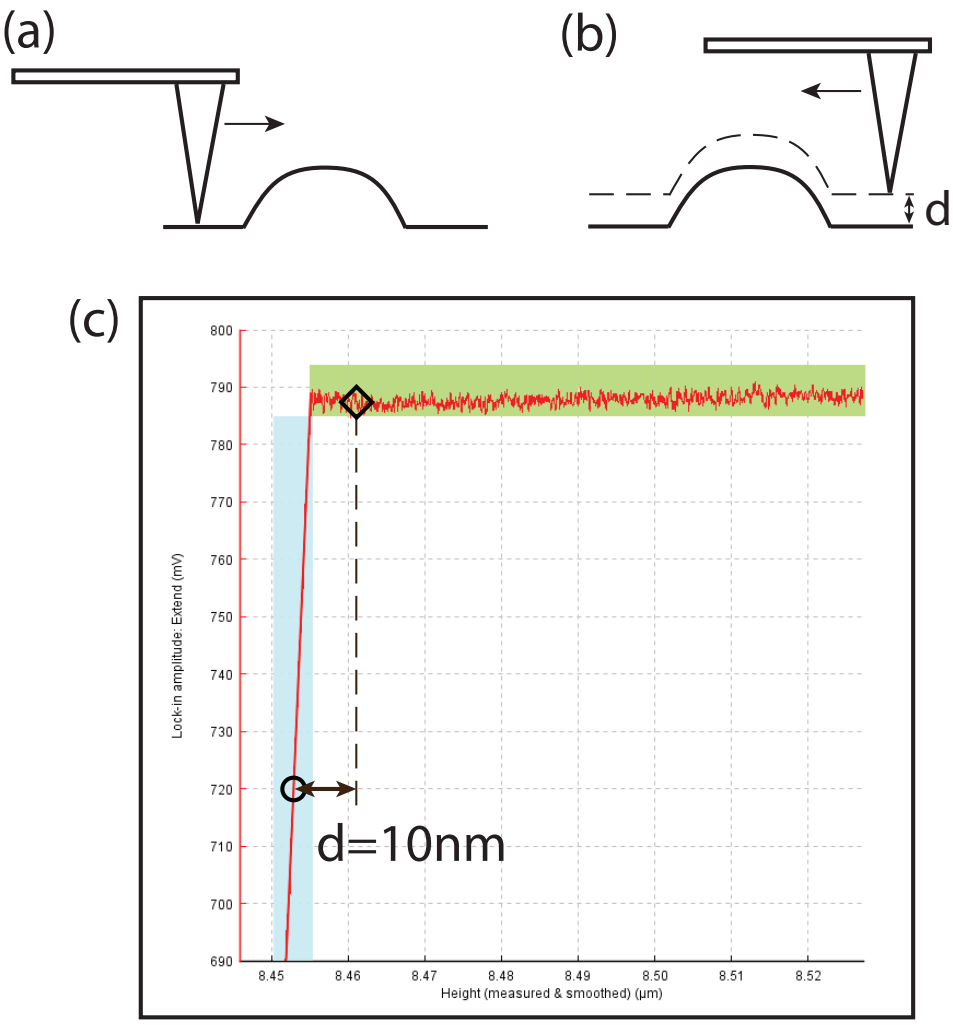

Figure 5.3: Illustration of hover mode: (a) Trace: Cantilever senses the topographic relief ($z(x, y)$) in *intermittent contact mode*. (b) Retrace: Cantilever is lifted by a distance d over the previously measured relief and the oscillation parameters are recorded at height $d + z(x, y)$. (c) Example force diagram (attenuation vs. distance) on embedding polymer material (Epon): Cyan area indicates the region of the red graph where short-ranged forces dominate, which define the effective surface topography. Green area indicates the region of the graph where the MFM cantilever is approximately in free oscillation and sensitive to magnetic forces if present. While the trace is adjusted to a certain attenuation (circle) well in the cyan area, the retrace is lifted to $d = 10$ nm, and therefore is well in the green area (diamond).

5.3 Results and Discussion

5.3.1 AFM vs. MFM topography:

Figure 5.2 shows the overview of the thin-section. The same sample and area within this section was scanned with an AFM tip, and then with an MFM tip (cf. figure 5.4 top and bottom). If there is signal from a magnetic dipole of a remanence bearing particle, it would appear as an additional feature overprinting the AFM-derived topography.

The MFM-derived maps turn out to be very similar in structure to the topography maps derived from AFM scans. In the area of the electron-opaque granules we were able to identify some features in the MFM-derived map that appear not or differently in the AFM-derived one (cf. figures 5.4(a) with 5.4(b)). Most of these differences can be attributed to the different color scales, which were used to cover the differently pronounced topographies derived by MFM and AFM. However, given the large number of features on the AFM map, the few extra features in the MFM map do not appear significant. Thus there are no clearly detectable magnetic dipoles expressed.

The key difference between the AFM and MFM scans is the amplitude of the topography. Some examples of height differences between AFM and MFM-derived topographies are given in figure 5.5.

The calculated height difference (red boxes in figure 5.5) between two points (white arrowheads in figure 5.5) demonstrates that the MFM heights are generally amplified relative to the AFM heights. This difference appears most pronounced at rough features (i.e. the granules). This effect can be reproducibly observed in the direct comparison of cross-sectional profiles taken over the same section in the sample with AFM and MFM respectively (see figure 5.6).

Here it has to be mentioned that the AFM and MFM profiles are derived from two separate measurements, including the change and re-adjustment of the cantilever. Therefore, the positions of the cross-sections may not coincide perfectly, which could give false positives. However, the profiles were positioned to cover the highest amplitudes of the granules present in the selected region, in both AFM and MFM. Although the corresponding AFM and MFM profiles are not exactly equal to each other, the variations along these profiles are still very similar in shape, but they reproducibly show the MFM height amplified. By and large, the differences are more of a quantitative (scale) than a qualitative nature.

The mentioned difference in topographic amplitude between AFM and MFM may be explained (i) either by induced magnetization in the granules, (ii) or by the different response characteristics of the MFM vs. AFM cantilevers to surface roughness.

(i) If the granules are made of a material of high magnetic susceptibility (such as iron or magnetite in the superparamagnetic or multidomain state), then the hard-magnetic coated tip induces a magnetization in the material which in turn produces a magnetic gradient field that attenuates the oscillation of the cantilever. This additional magnetic force modulates the topography derived from interatomic (Van-der-Waals) forces. The force-feedback mechanism of the AFM-device adjusts the cantilever height above the surface to the level where the sum of all forces acting on the cantilever is equal to force that defines the reference level of attenuation. The resulting height in MFM then is different from the AFM-derived height due only to atomic forces. Therefore, the additional height can be an effect of induced magnetization in the granules.

(ii) The observed height difference can also be explained by the surface roughness of the granules. AFM and MFM cantilevers differ in their geometrical and physical properties (length, weight, stiffness of the cantilever and shape and coating of the tip). These differences affect the resonance frequency of the oscillating cantilever and therefore also the response behavior to changes in topography. In other words, the height in any AFM measurement in intermittent contact mode generally depends on the cantilever response behavior to roughness of the sample surface. The height therefore is a fictive measure that needs to be calibrated by a suitable standard.

At this point, we cannot assign the amplified MFM topography to either induced magnetization or to different response characteristics to surface roughness. Either way, there is no clear manifestation of magnetic dipoles due to magnetic remanence in the sample examined.

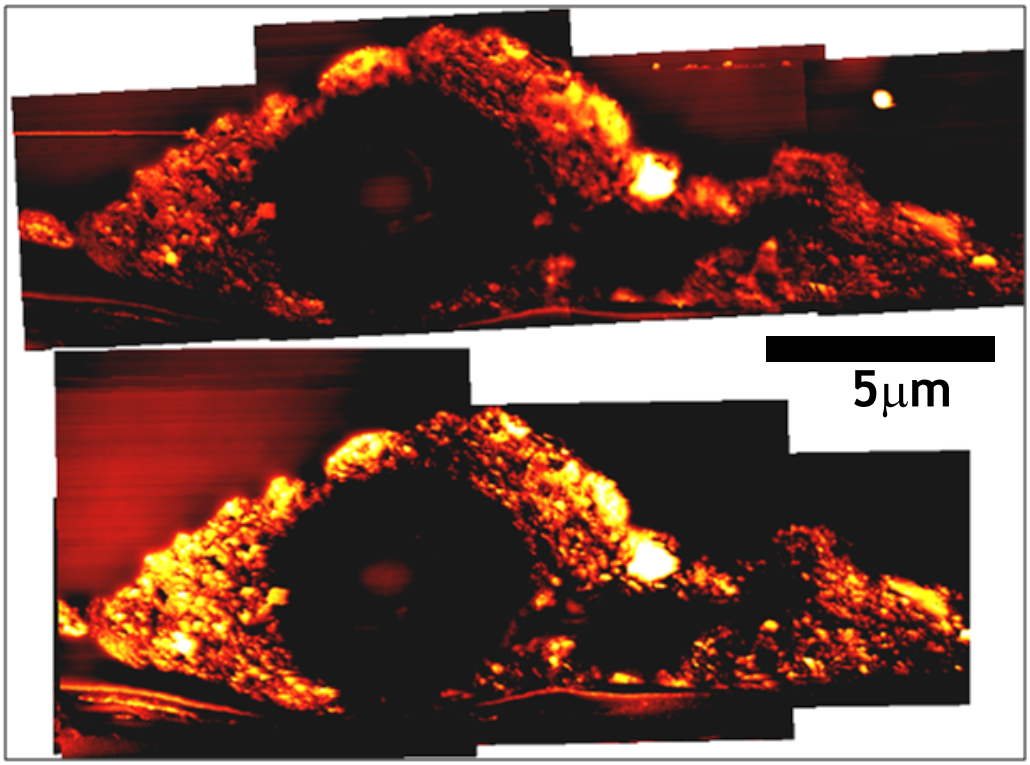

Figure 5.4: The same area as observed in figure 5.2. Top: under AFM. Bottom: with MFM cantilever. The topography is relatively strong. No significant difference in structures between AFM and MFM is visible, which suggests that the MFM image is dominated by topography and not magnetics.

Figure 5.5: Cross-sectional profiles through the sample illustrate different heights of features between AFM (left column) and MFM (right coumn). a, b, c, d and e each represent a doublet of profiles (AFM and MFM) along the blue line through the sample. White arrowheads show the measurement points for the calculated differential height (in red box).

Figure 5.5

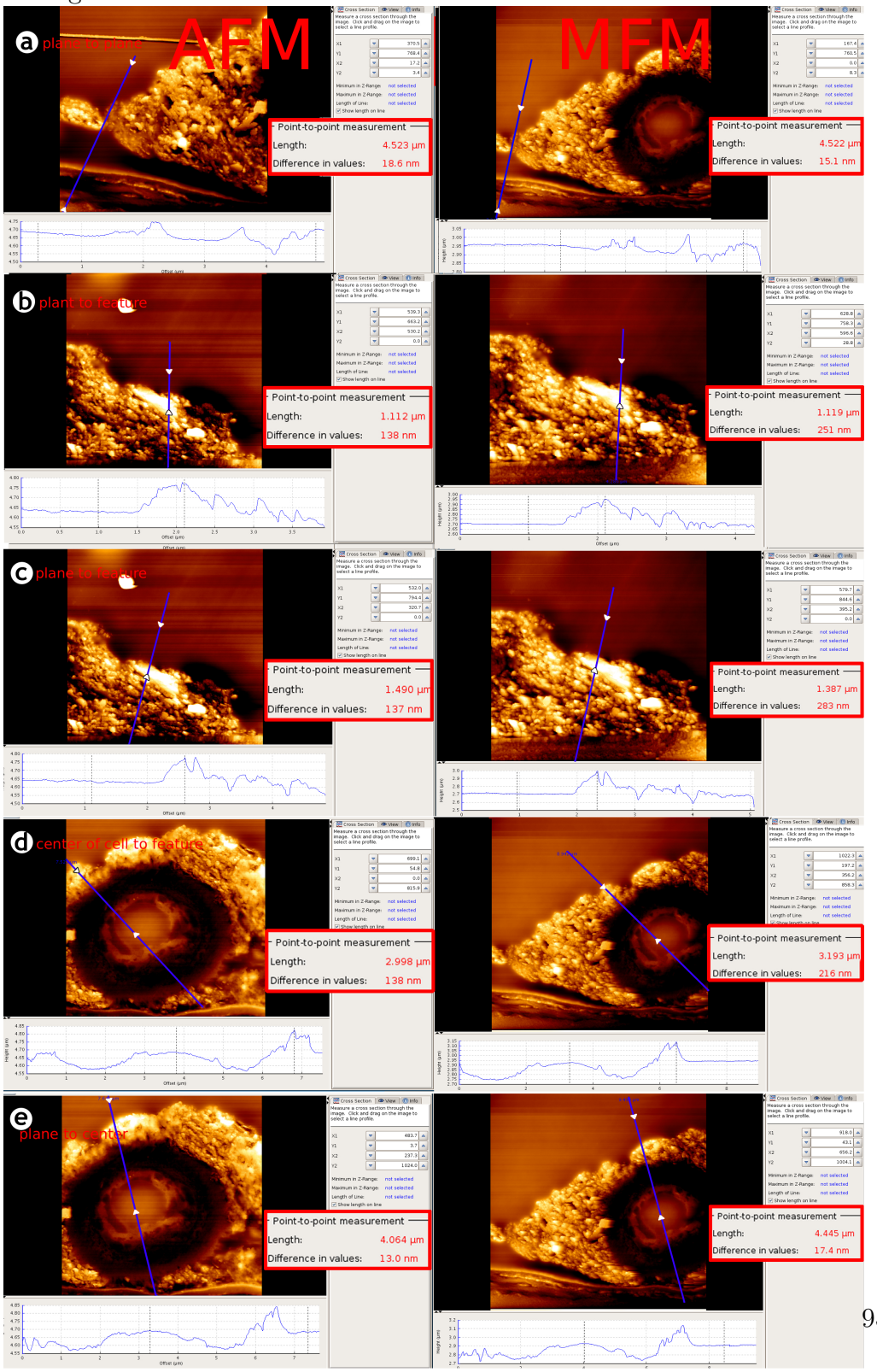
AFM
MFM
a plane to plane
Point-to-point measurement
Length: 4.523 µm
Difference in values: 18.6 nm
Point-to-point measurement
Length: 4.522 µm
Difference in values: 15.1 nm
b plant to feature
Point-to-point measurement
Length: 1.112 µm
Difference in values: 138 nm
Point-to-point measurement
Length: 1.119 µm
Difference in values: 251 nm
c plane to feature
Point-to-point measurement
Length: 1.490 µm
Difference in values: 137 nm
Point-to-point measurement
Length: 1.387 µm
Difference in values: 283 nm
d center of cell to feature
Point-to-point measurement
Length: 2.998 µm
Difference in values: 138 nm
Point-to-point measurement
Length: 3.193 µm
Difference in values: 216 nm
e plane to center
Point-to-point measurement
Length: 4.064 µm
Difference in values: 13.0 nm
Point-to-point measurement
Length: 4.445 µm
Difference in values: 17.4 nm

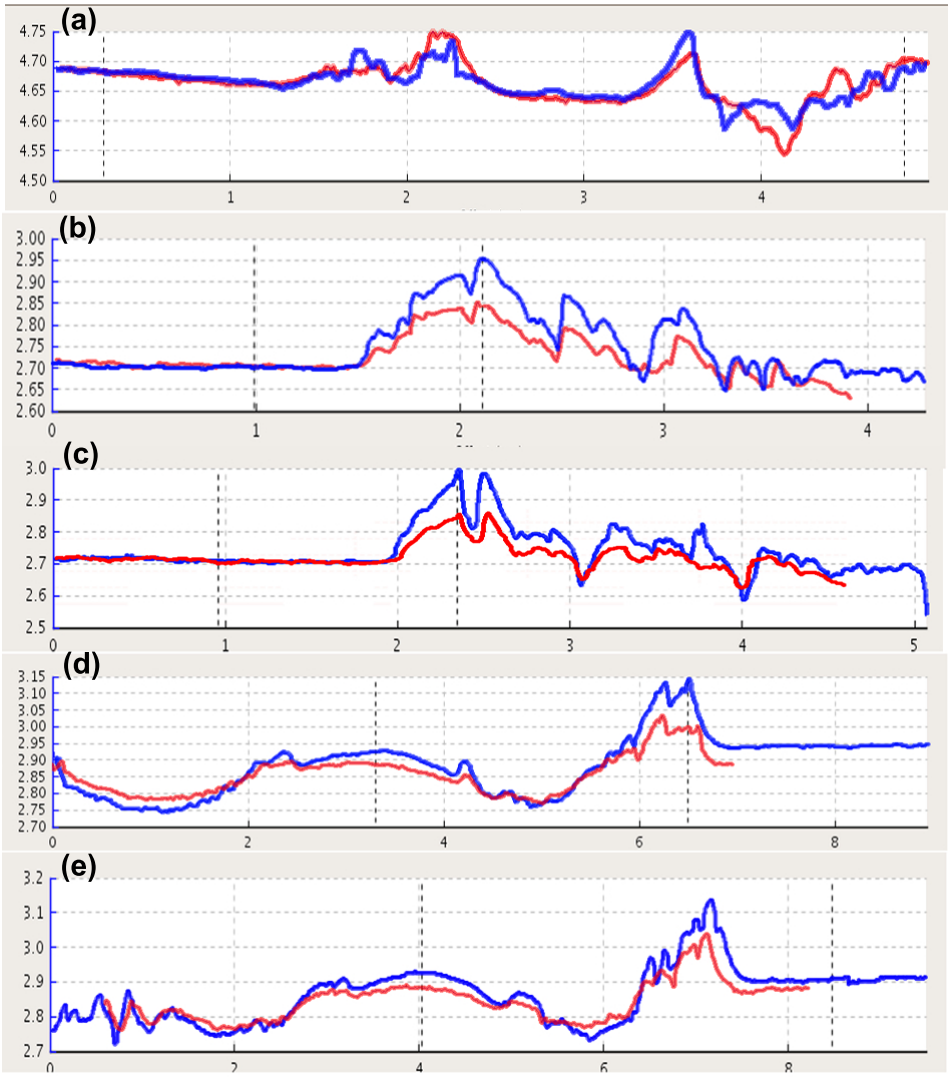

Figure 5.6: The AFM (red) ad MFM (blue) derived height variations of the cross-sections (figure 5.5) in comparison. By and large, the difference between AFM and MFM is in terms of scale, but not in terms of features.

5.3.2 MFM hover mode:

As positive control we choose a standard computer hardrive, which has distinct magnetized domains representing stored single bits. Figure 5.7a shows the trace height, a representation of the surface topography. In the retrace the magnetic bits become visible in the amplitude map (amplitude of oscillation; figure 5.7c), and even more clearly in the phase map (phase of the oscillation; figure 5.7d). Residual structures of the trace (height and amplitude; figure 5.7a and b) are not visible in the retrace.

The magnetic information is well visible in the retrace maps, but not obviously visible in the trace maps. This shows that even tough the magnetic signal is relatively weak compared to the topography, the hover method nevertheless turns out to be sensitive enough to resolve it.

As a negative control we use those areas on the antennae section that do not show dark granules in the TEM image, for example: the round cellular structures that are surrounded by the granules, or the area above the granules, consisting of polymers from the embedding material (Epon), as well as the area at the bottom of the scan, which represents different organic structures, such as skin or chitin. From these iron-free structures we do not expect any magnetic signals.

The sample scanned in hover mode (figure 5.8) is a selected area of the sample shown in figure 5.4. The trace height reproduces the strong topography. The trace amplitude represents the residual topography and looks like a high-pass filtered image of the original topography. The retrace was performed at a hover distance of 20 nm above the trace height, which is theoretically well above the reach of short-range (e.g., Van-der-Waals) forces. The retrace phase (figure 5.8d and 5.9c), which is most sensitive to magnetic forces (for positive control see figure 5.7d), bears a weak signal, which however is strongly correlated with the topography. Therefore, we hypothesize that if the topography is so strong that it prints through into the retrace, it critically disturbs the detection of potentially present magnetic forces.

Although the MFM trace height contains the topographic information plus the magnetic information, the topographic signal potentially dominates (see also figure 5.7a). The retrace amplitude, which has been recorded 20 nm above the trace height, should not carry topographic information. Therefore, if the trace height is subtracted as a linear component from the retrace amplitude, the difference should be of magnetic origin. The calculated difference (figure 5.9d), shows some spots of the colors red or

dark blue (note the changed color scale). These regions co-localize with white or black regions in the trace amplitude map without smoothing (figure 5.8b) and represent areas with the steepest slopes on the surface. At very steep slopes the tip can lose contact to the surface; likewise the side of the pyramidal tip may interact with the upsloping sample surface instead of the tip interacting with the surface atoms immediately beneath it. Such events produce artifacts in all measured parameters of the hover mode (cf. to figures 5.8c, and 5.8d). The other signal in figure 5.9d in the colors turquoise to yellow all co-localize with topography, regardless of whether derived from the granules or from the iron-free material. Therefore, we assume that there are no magnetic dipoles in significant numbers or strength.

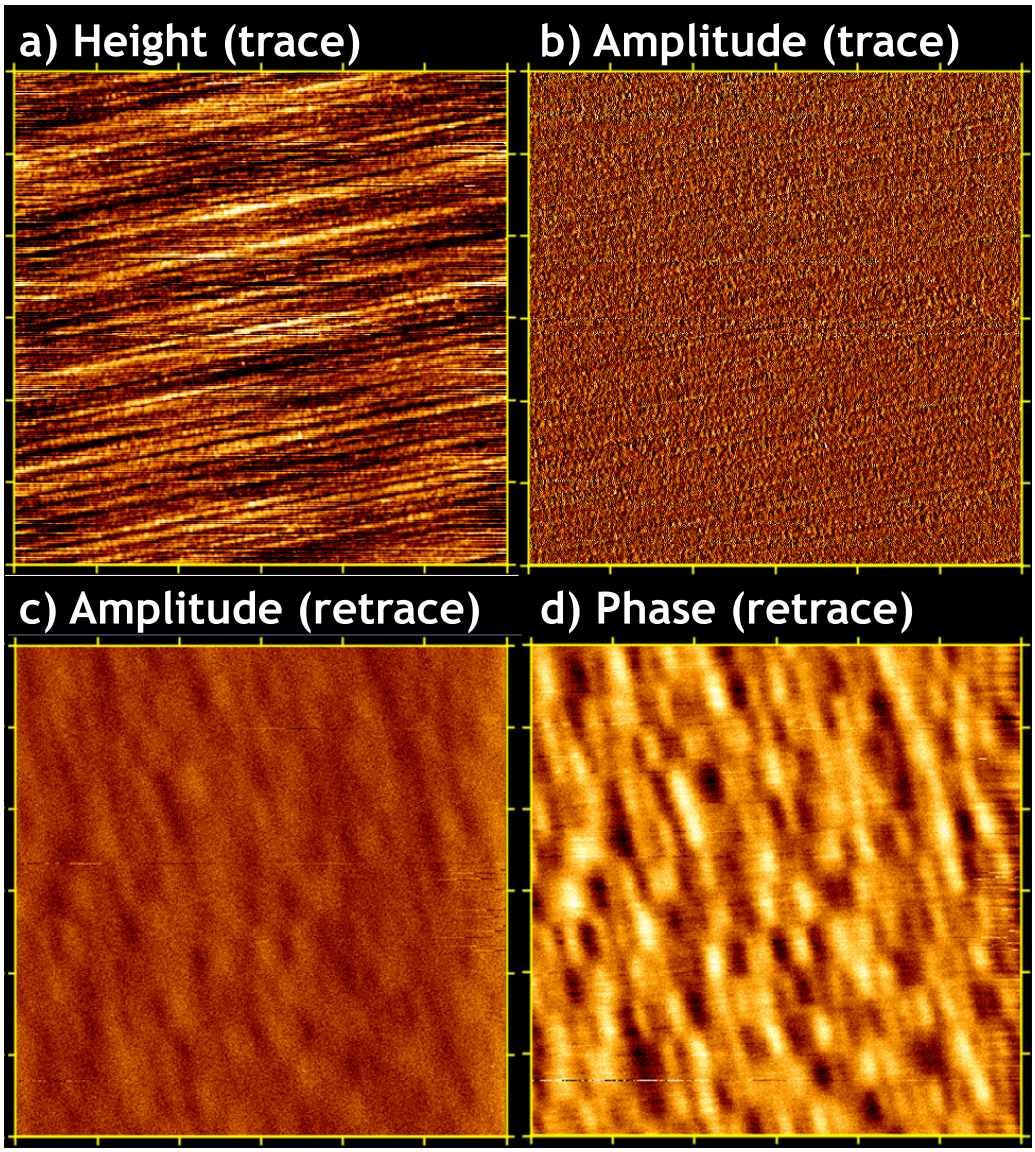

Figure 5.7: MFM hover mode scan on a computer harddrive: The trace of the scan shows the topography in the height (a), and the oscillation amplitude in (b). Only surface features are visible, and no magnetic forces are detectable. In the retrace oscillation amplitude (c) and retrace oscillation phase (d) of the scan the cantilever hovers with 10 nm distance over the trace height. Surface features are no longer visible and magnetic interactions become apparent. The retrace phase (d), showing clearly a bit pattern, appears most sensitive to the magnetic forces.

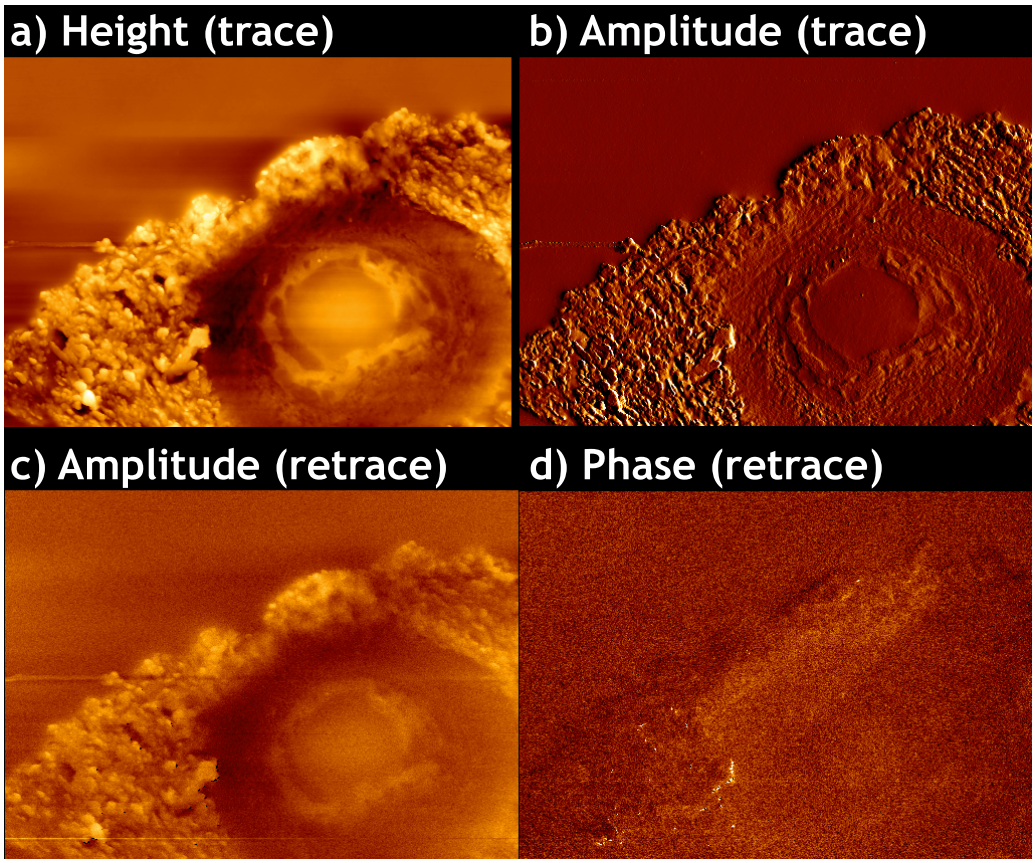

Figure 5.8: MFM hover mode scan on a selected region (8.3x6.35μm) of the sample shown in figure 5.4: (a) trace height of the sample. (b) trace amplitude shows a derivative-like filter of the topography residual that could not be adjusted by the height drive of the cantilever. The white and black spots show the region of strongest surface slopes, where the cantilever lost the intermittent contact. (c) retrace amplitude, performed on a hover distance of 20 nm, is dominated by topographic effects. (d) retrace phase bears a relatively weak signal.

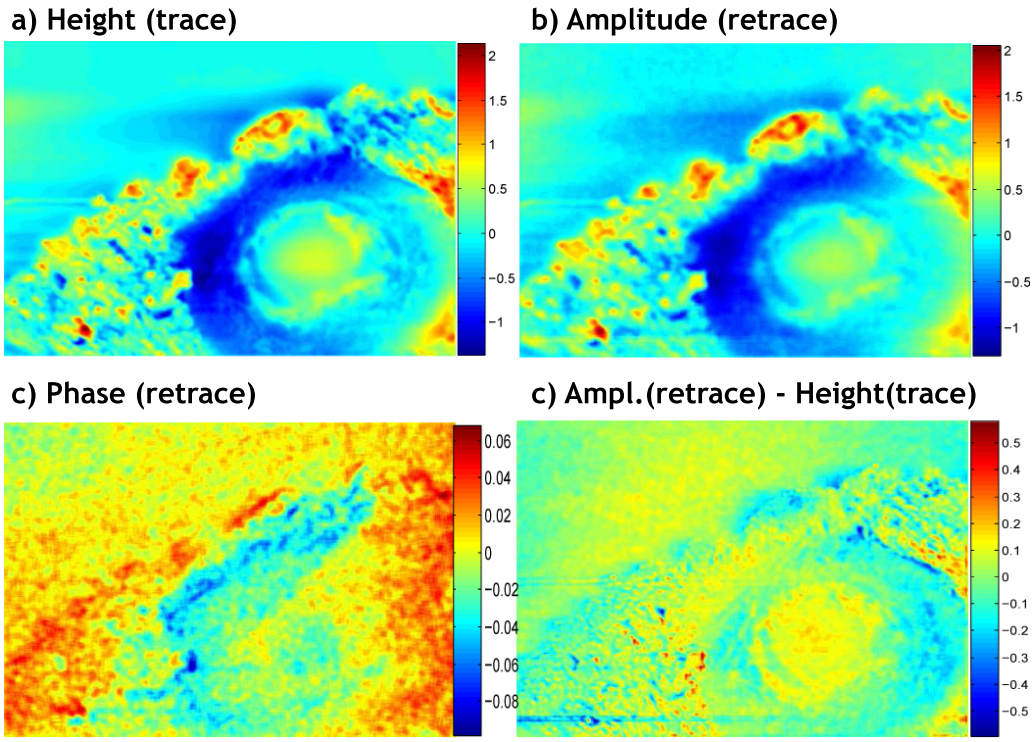

Figure 5.9: Post-processed data of figure 5.8 (with Matlab): (a) trace height, detrended and smoothened; (b) retrace amplitude, smoothened and rescaled; (c) retrace phase, inverted and rescaled; (d) retrace amplitude minus trace height (b minus a). (a) and (b) do not bear significant differences. The maximum differences (red and blue spots in the map of differences: c) can be attributed to contact loss at slopes (cf. figure 5.8b). The signals in the color levels yellow to turquoise co-localize with topography features equally well inside and outside the regions of possible magnetism, as do the signals on the retrace phase map (c). No features that indicate magnetism are detectable, except sporadically.

5.4 Conclusions

In the samples we were not able to identify with certainty features containing remanent magnetization, except sporadically. The absence of a clear magnetic signal in the MFM imaging despite the presence of magnetite/maghemite, as confirmed by Oliveira *et al.* (2010) with SAED, can be explained by the effect of the overwhelming topography, which reduces the relative sensitivity of the MFM tip to magnetic signals. A comparison between the biological thin sections and the hard drive shows that the typical grain size is comparable, whereas the topography differs

by up to two orders in magnitude (harddrive ∼1 nm; thin section 50 to 200 nm). In future a calibration should be done on especially prepared samples with known content of magnetic material as a function of surface roughness (which could be achieved by focused ion-beam ablation). This would provide a practical criterion for the maximum surface roughness that can be studied without loosing sensitivity for the magnetic information.

Another approach would be to expose the sample to a moderate but homogeneous magnetic field (i.e. 10 Oe) while doing MFM scans. A magnetic signal appears when there is induced magnetization involved with the granules, If so, it should express magnetic poles as additional structures overprinting the topography map.

A technique that would be insensitive to surface roughness of the order of 100 nm would be scanning SQUID magnetometry (e.g. Baudenbacher *et al.*, 2002), where a SQUID sensor measures the magnetic flux density about 100 μm above the sample surface. However, due to this long distance, this measurement technique does not have the spatial resolution to map in detail the magnetization distribution in a sample with 10 μm linear dimensions. Yet, it might at least be sensitive to pick up the magnetic stray field produced by the overall structure, relative to the background. In terms of magnetic moment sensitivity, a scanning SQUID magnetometer is of the order of 10 fAm^2, which corresponds to the cellular magnetic dipole moment of candidate magnetoreceptor cells in trout olfactory tissue (see chapter 2).

A technique which is not sensitive to surface roughness and yet has a spatial resolution of 30 nm would be scanning transmission X-ray microscopy (STXM) in combination with X-ray magnetic circular dichroism (XMCD) to selectively probe the magnetization state of an element like iron (Lam *et al.*, 2010). However, while this synchrotron based technique is capable of resolving single-domain magnetite carrying magnetic remanence, it is not suitable to identify superparamagnetic particles, which produce no XMCD signal.

We did not detect permanent magnetic material in the sample due to the overwhelming topography, which seriously diminishes the sensitivity to magnetic features. From a theoretical point of view, it is possible that permanent magnetic particles are present, but arranged in a "magnetically silent" configuration (see figure 5.10b), where the dipole fields cancel each other at the surface, leaving fields of higher order (e.g., quadrupolar), which

diminish more rapidly with distance compared to dipolar fields and hence are harder to detect in the presence of a strong topographic signal. Likewise, another "magnetically silent" configuration would be a permanent magnetic particle shielded by surrounding material of large magnetic susceptibility (see figure 5.10c). Both models would explain why we did not find evidence for magnetic forces, even though strong magnetic material such as magnetite or maghemite had been detected in the scanned sections before by TEM analysis (Oliveira *et al.*, 2010). Following this thought, the total remanent magnetic moment of the arrangement of granules could well amount to zero. This possibility is also consistent with the observation that the magnetic material is incorporated from the environment (soil) and not biomineralized by the host organism. Without biological control on biomineralization, it is hard to imagine how to build ordered magnetic structures (like a magnetosome chain) with a high remanence state. Thus, if the structure studied is part of a magnetoreceptor, then it would be based on induced magnetization. The magnetic susceptibility is the key parameter in the mathematical model by Oliveira *et al.* (2010), but remains to be measured before a definitive conclusion can be drawn. Independent of its possible magnetic function, the ant's Johnston's organ when used as a graviceptor or acceleration receptor benefits from the relatively dense iron rich crystals deposits, increasing the inertia of the membrane and thus improving the sense of acceleration, as proposed by Winklhofer and Kirschvink (2010).

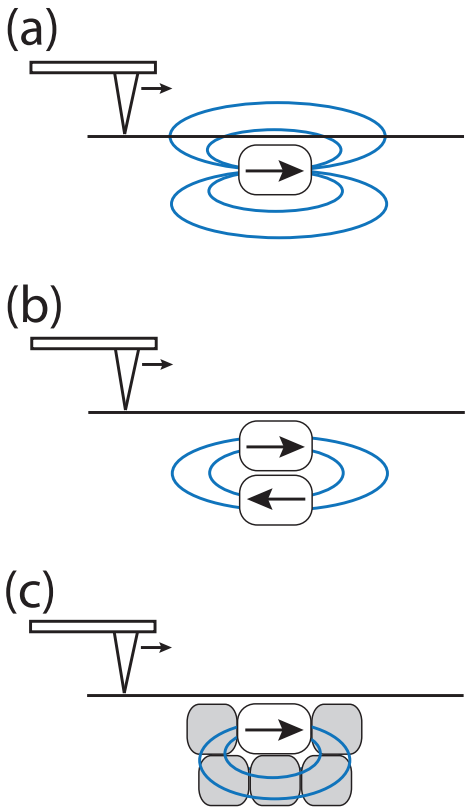

Figure 5.10: Examples for "magnetically silent" configurations (b, c). (a) From a single magnetic dipole (remanent magnetic particle) the fieldlines (blue) project well through the surface, and produce a magnetic gradient field that can be detected by MFM. (b) Two magnetic particles whose remanence magnetization vectors are opposite to one another form a nearly closed flux loop, allowing only a small fraction of fieldlines to escape beyond the surface. In consequence, the gradient field at the surface is strongly diminished and hard to detect. (c) The remanent magnetic particle is embedded with granules of a high magnetic permeability (gray), which form a closed flux loop and appears as "magnetically silent".

A

Appendix: Confocal-microscope and laser specifications

Walker *et al.* (1997) used confocal microscopy for detecting crystals in organic tissue, which in reflectance mode appear as bright spots. The key advantage of confocal imaging is to suppress unwanted light from optical layers above or below the very confocal plane that is being sampled and therefore to provide a defined axial resolution (depth resolution), given by

$$z_{min} = \frac{2n\lambda}{NA^2}\,, \tag{A.1}$$

where n is the refractive index of the object medium, λ is the wavelength of the light, and NA is the numerical aperture of the objective (Inoue, 2006). The upright confocal laser scanning microscope (LSM) we run (Zeiss LSM 330) was initially customized for materials science applications and equipped with a an internal 633 nm HeNe laser. However, when it comes to imaging cells, fluorescents markers have to be excited, which usually require short wavelengths (e.g., excitation wavelength for FM1-43 as membrane stain is less than 550 nm). To overcome this limitation, an Argon multiline laser was implemented in the confocal setup to provide variable excitation wavelengths between 458 nm and 515 nm. For this purpose, a support for the laser tube and a filter wheel had to be designed, which will be described below in

detail. Another limitation of the available LSM setup was the inability to be operated in transmitted light mode. Biological cells have a poor contrast in reflected light and can be better imaged in transmitted light. This necessitated redesigning the construction of the microscope platform to enable transmitted light imaging, at least in widefield. Furthermore, the design should allow an optical trap setup (inverted setup) to be adapted to the upright LSM from underneath. With an optical trap, individual cells can be selectively moved or pinned, depending on the application.

A.1 Laser specifications

For the laser setup we kept the internal HeNe 633 nm laser, and added an external Argon multi-line laser (JDS 2214-ML25), which generates several laser lines to choose from, i.e., 458, 476, 488, 497, 502, 515 nm with laser power up to 25 mW. The DJS laser (2.2 kW, 110V, 50-60Hz) was connected through a highly efficient 3kW ring-core transformer to the power outlet, fused at 16A.

The laser lines can be selected with optical filters in a filter wheel (see figure A.1), which blocks out the other wavelengths than the one chosen. For exciting the fluorescent stain FM 1-43, the laser line 458 nm is working best, which is filtered out by a shortpass (see figure A.2). The 488 nm line (separated with a bandpass filter; see figure A.3) can be used as a high power laser line for high resolution imaging. Although the transmission of this filter is only 30%, the loss in intensity is compensated by the power of this 488 nm line, because it is the most-dominant line of the Argon laser. The 515 nm line, as the longest wavelength line of the Ar laser, can be easily isolated with a longpass filter or any other filter that cuts off sharply between 502 and 515 nm (see figure A.4). This green light line can for example excite autofluorescence of cytochrome c (Spiro and Streaks, 1972), or may be used for various fluorescent stains.

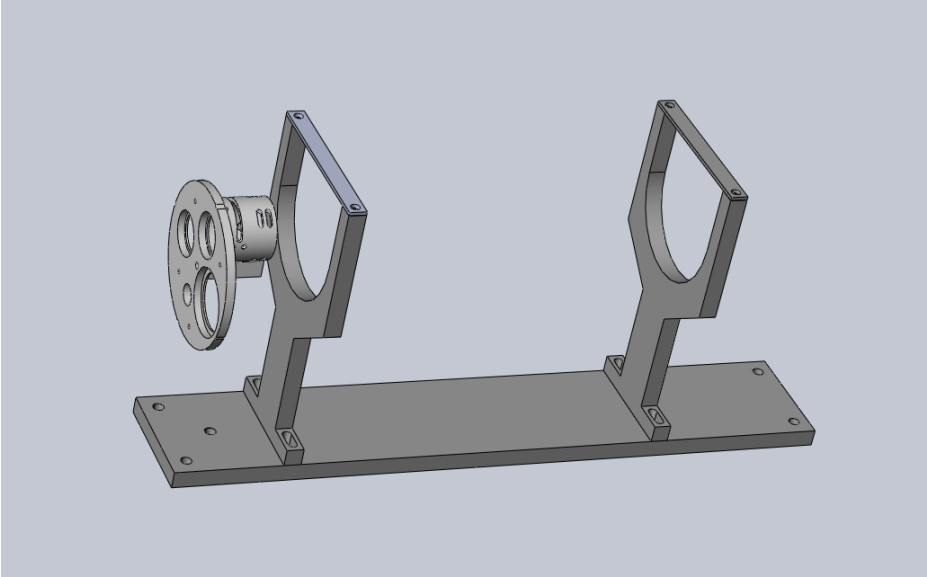

Figure A.1: The mount for the JDS Argon Laser and the filter-wheel with slots in different sizes.

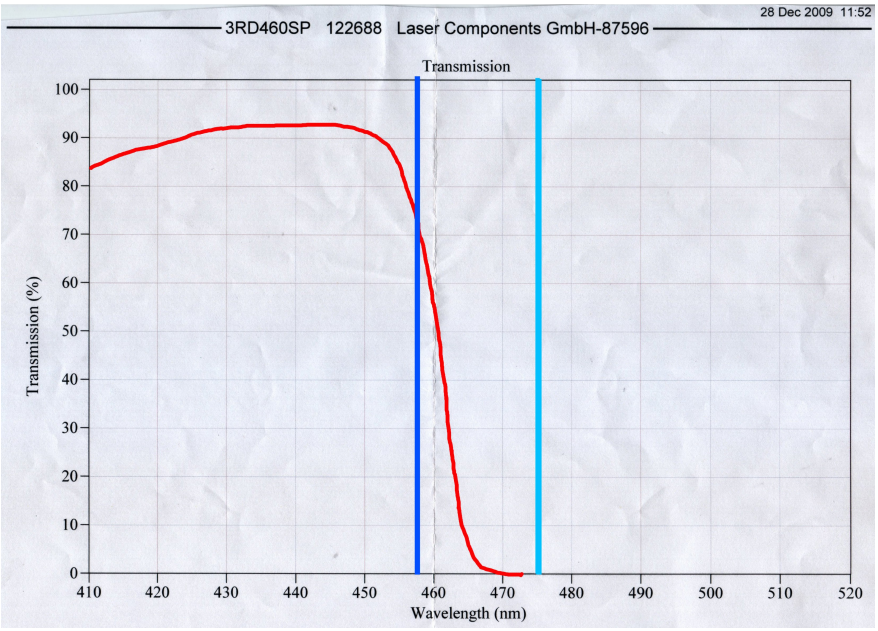

Figure A.2: Transmission spectrum of the 458nm line filter (SP 460)

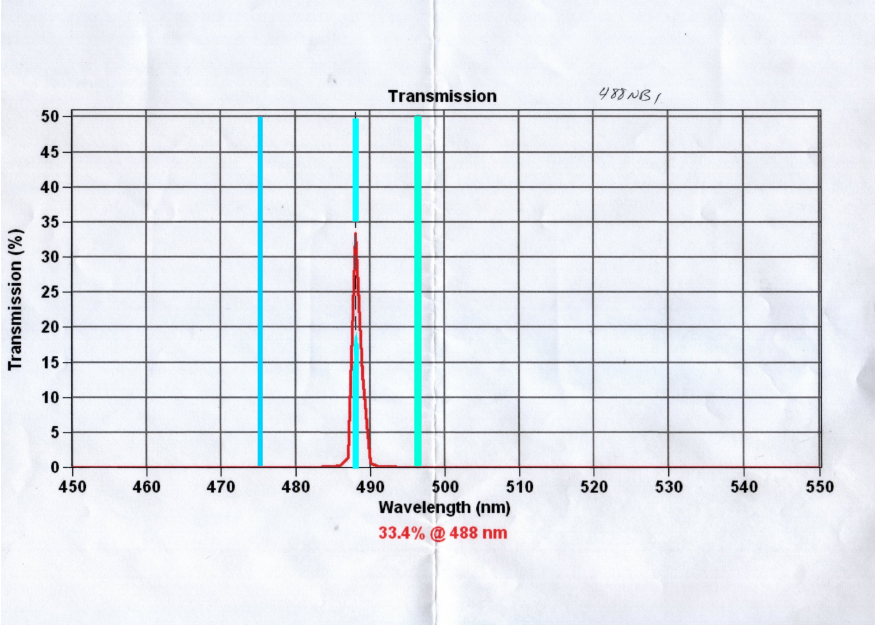

Figure A.3: Transmission spectrum of the 488nm line filter (BP 488/1)

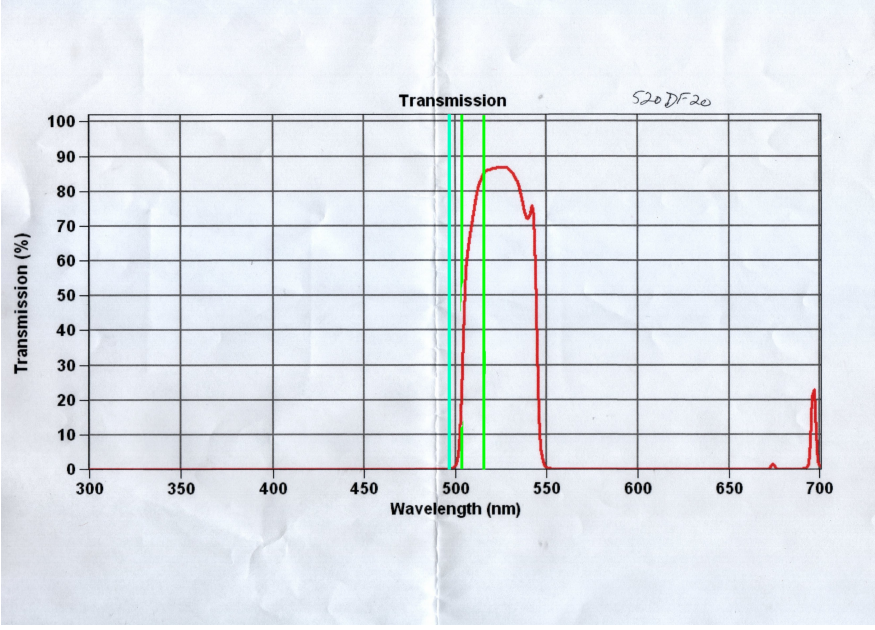

Figure A.4: Transmission spectrum of the 515nm line filter (BP 520/20)

A.2 The optical trap setup

The optical trap is a strong laser, focused by a high magnification and high NA objective lens (here: Zeiss 63x NA=0.9). At the focal point, the laser beam is densely bundled and forms a "waist", which produces an electric field gradient that is directed toward the focal point. A dielectric particle (e.g., a micron-sized glass bead) is forced to move along the gradient to the focal point, where it can be held (Ashkin, 1997). By moving the laser spot, the particle can be dragged. By attaching a dielectric bead to a biological object, that object can be manipulated. This effect can be used to isolate single cells, but also to study mechanical properties and forces at the microscale.

On the constructed platform the LSM and its motorized stage are mounted separately. One field on the platform is provided to accommodate either the transmitted light source or the optical trap system (see figure A.6). The design is such that the optical axis of the LSM (see figure A.5) extends through the hole in the stage directly into the optical axis of the trap. Optionally the trap can be substituted with a light source for transmitted light imaging.

To enable all these modifications we designed the platform using (non-magnetic) alloy beams of a modular construction system (item©; see figure A.6). When needed, the flexibility of this system allows one to easily rearrange the optics on the platform for new experimental setups.

For the main frame we used 80x80mm profiles (figure A.7a) which are statically rather over-sized, but in order to avoid vibrations in the platform they are justified. An option for further damping of noise is to fill the internal of the alloy profiles with spray-foam. The sub-frame carrying the microscope, stage, trap, external laser and the laser-hood have smaller dimensions (50x50mm, see figure A.6b).

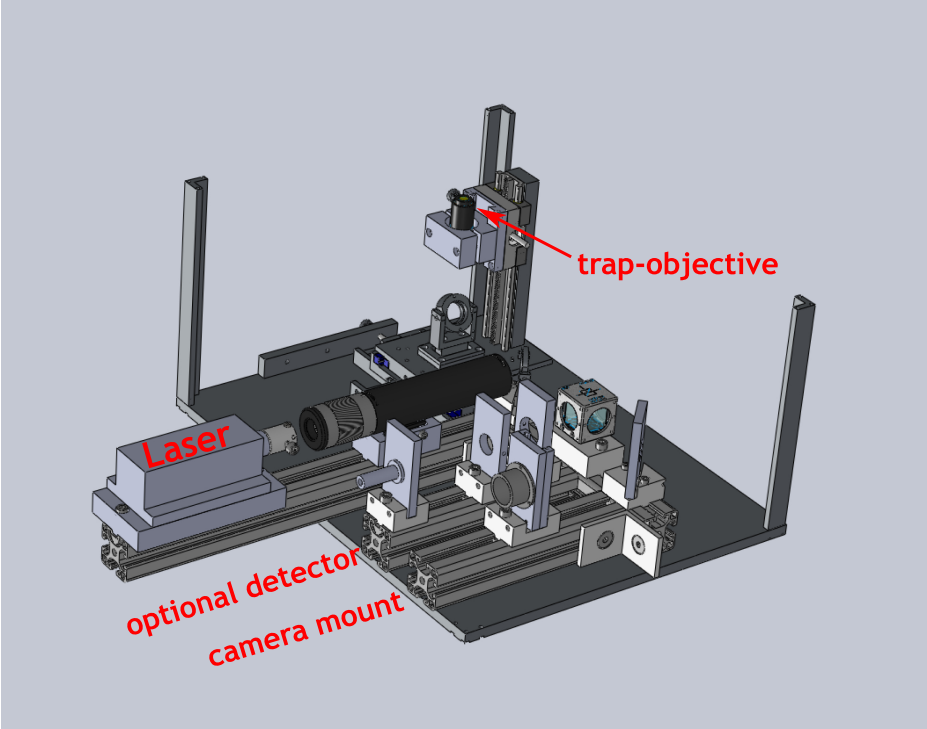

Figure A.5: (courtesy of Gigler, A. and Sekhavati, F.) Optical trap. The trap objective at the tower can be placed from underneath the microscope stage to the optical axis of the confocal microscope.

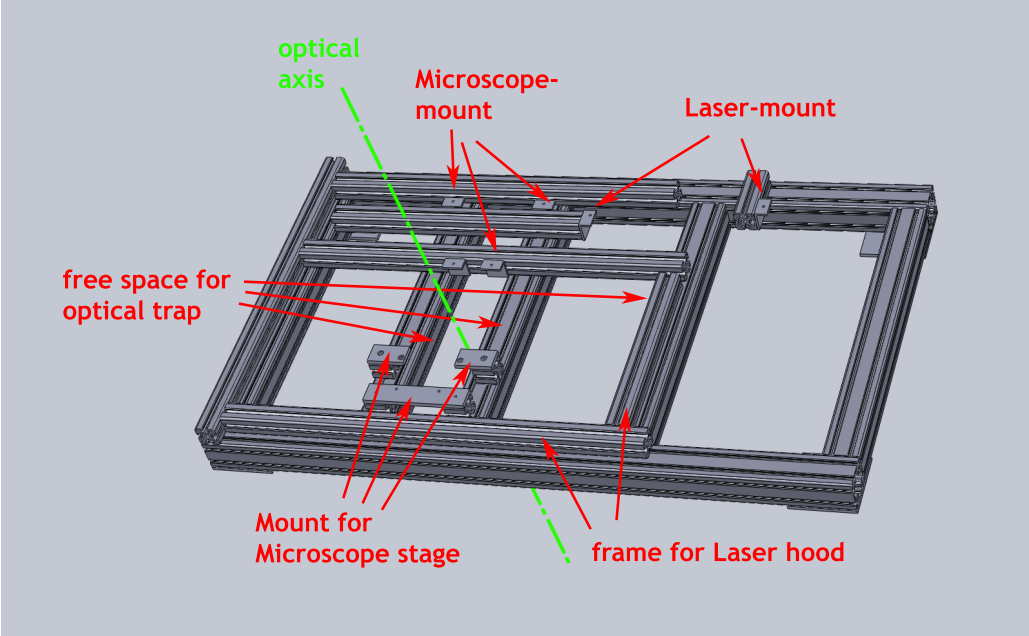

Figure A.6: The platform provides stable mounts for the confocal microscope and all its peripheral equipment. It also provides space to host the optical trap at the optical axis of the microscope

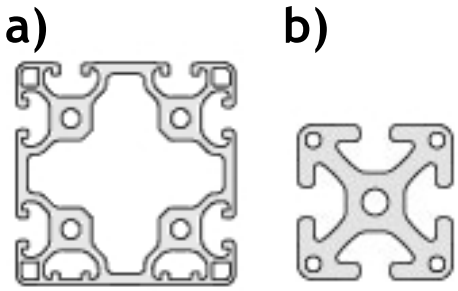

Figure A.7: adapted from item24.de: alloy profiles used for the platform: a. 80x80mm (No 0.0.547.52) is the "light" edition, which provides plenty of space inside, which can be filled with foam for vibration damping. b. 50x50mm (No 0.0.624.52) used as rest of the Laser-hood.

B

Appendix: The Magnetoscopes

When looking for and studying magnetic cells under the microscope it is necessary to control the magnetic field that the cells are exposed to. We adapted the rotating magnetic field design ("Bacteriodrome") that Petersen *et al.* (1992) introduced in the study of magnetic bacteria, with the aim to keep these motile microorganisms in the field of view by making them swim in closed trajectories (e.g., circles).

In this work, the rotating magnetic field technique was applied for the first time to search and study potential magnetoreceptor cells. The applied magnetic field forces the magnetic inclusions in such magnetoreceptor cells to align with the field, therefore the rotating field causes the cells to rotate. Rotating objects are easy to identify under the microscope, once they are in the field of view. Scanning the sample on the glass slide will consequently find the magnetic objects in the sample. This makes the Magnetoscope a powerful tool for finding potential magnetoreceptor cells.

In the course of the project we devised a new kind of magnetoscope that has a spinning magnetic finger too produce strong rotating magnetic fields, sufficient to mechanically activate motion of relatively large biological objects containing magnetic inclusions. In this application we expected cells of the size of $\sim$ 8 to 20 μm, however the magnetic moment of the inclusions were unknown.

B.1 Magnetoscope 1

The first design uses a magnetic gradient finger rotating over the sample with its rotational axis parallel to the optical axis (see figure B.1) of the microscope (Zeiss, ICM-405M). At the gradient finger of high magnetic susceptibility material (Weicheisen), a rare earth based permanent magnet was placed at the outer end (in our case a cylinder of 20 mm diameter and 10 mm height from supermagnete.de). This provides a strong magnetic field at the sample-side of the finger, which is dependent on the strength of the permanent magnet. Multiple magnets can be attached. All supports and mechanics are made of non-magnetic materials, such as plastics or rubber, in order to avoid magnetic interactions with the field or deformation of the fields shape.

The strong field at the sample is able to orient large objects. Even junks of tissue of roughly 100 μm in size having a magnetic cell inside could be moved by the interaction with the field. The gradient finger has a non-homogeneous magnetic field with gradients at the sample-side. Even though the field at $\sim$ 5mm distanced tip of the finger was strong, the gradient of was not strong enough to drag objects in the solution. The advantage of this design is that also relatively weak magnetic objects responded. The disadvantage is that the strong fields potentially erase the natural magnetic state of the magnetic object. For example magnetic inclusions in cells can get re-magnetized (biasing further magnetic measurements) or perturbed in their arrangement (e.g. collapsing magnetosome chains). In the worst case we find false positives, by inducing magnetization in magnetic materials that have no strong magnetism in weak fields.

Figure B.1: Magnetoscope 1.

B.2 Magnetoscope 2

The second design of the magnetoscope was very similar to the first (see figure B.2). Instead of a belt driving a friction-type bearing where the magnetic finger and the magnets are mount, here a glass-ball-bearing is situated around the condenser of the microscope (Zeiss, Axiovert 135). At the outer ring of the bearing the Magnetic finger is mount. This setup runs smoother and generates less vibrations than the first version with the driving belt. A realization of this ball bearing based magnetoscope has been implemented in Dr. D. Keays's lab at the IMP in Vienna.

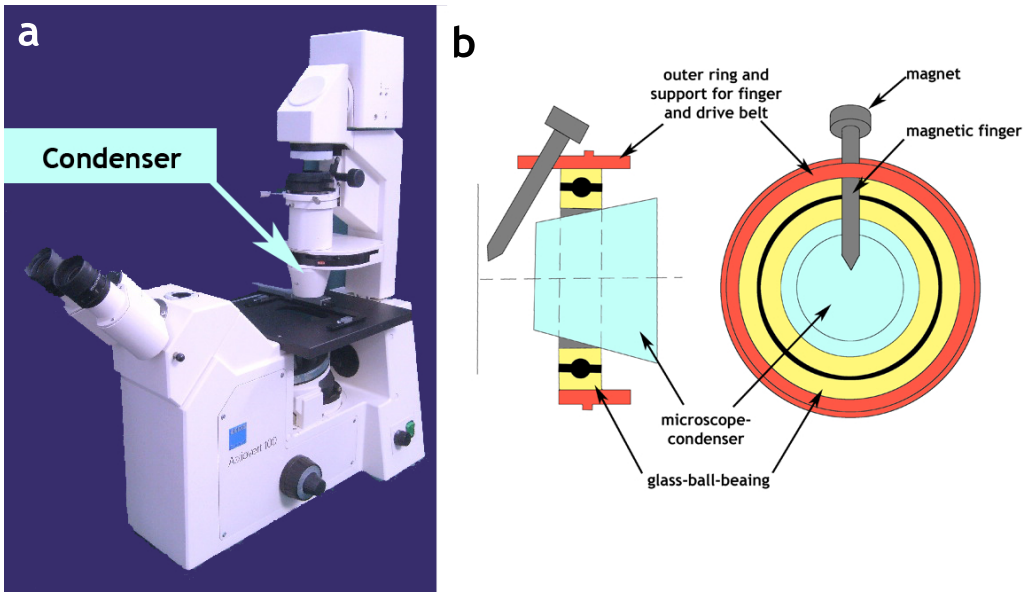

Figure B.2: Magnetoscope 2

B.3 Magnetoscope 3

The third design of the magnetoscope does not contain any mechanically moving parts, but has two pairs of coils similar to Helmholtz coils which are designed such that they generate a homogeneous magnetic field at the center of the specimen mount of the microscope table (figure B.4). Applying a current with a sine-wave shape to one pair of coils, and synchronously another sine-wave current with a phase-shift of 90 degrees to the second pair of coils, produces a homogeneous rotating field. The magnetic objects swimming in the buffer will align to a direction defined by the superimposed magnetic fields of the two pairs of coils. The strength of the magnetic field can be fully controlled by the input current in the coils. The speed of rotation is controlled by the frequency of the sine waves. Adjusting the phase-shift of $+90°$ or $-90°$ will define the rotational direction (cw or ccw). An arbitrary waveform generator (USB connected to a computer; M631 from ETC) with two synchronized channels generates the sine-wave driving voltages. These signals then are amplified by power amplifiers (Keopco BOP-50-20; one for each channel), and fed each one pair of coils. The coils in each pair of coils are equivalent to each other (dimensions and windings) and are connected in series to provide the same current.

The coils were designed to continuously reach a peak amplitude of ±20 Gauss without overheating, and over a short period of time ±30 Gauss peak amplitude. The dimensions of the coils are constrained by the geometry of the microscope to 30x18.4 cm for the y-field-coils with a distance of 19 cm in between and to 32.5x30.0 cm for the x-field-coils with a distance of 18 cm in between (all measures are the inner dimensions of the rectangular coils).

In single wires a moderate current density of up to 5 A/mm^2 is does not overheat. According to VDE-0100, wires in buildings are allowed to carry 16A in a 1 mm^2 wire as maximum (16 A/mm^2). Those single wires densely packed, as they are in a coil, have a reduced surface over which the wire can cool down by heat flux. Therefore from experience, wires in coils with the here expected dimensions, can take a current density of roughly 3 A/mm^2 without critical overheating. The wire used for the coils is of copper, coated with varnish resisting 180°C without melting. Overheating would burn the varnish and ends up in shortcuts between the loops in the coil.

The current density mentioned, is assumed to be a constant current. In our case we apply sine-wave shaped current. The Sine-wave amplitude is 1.41 times ($= \sqrt{2}$) larger than the activation current (Wirkstrom) over a period of sine. The sine-current amplitude can be adjusted to a maximum of 4.23 A/mm^2 (=3.0 A/mm^2*1.41).

To estimate the maximum B-Field that can be achieved with the coils, we use the following relatively simple analytical model, assuming round coils and a diameter that covers the same surface as the corresponding rectangular coils.

$$H = \frac{Ir^2N}{2(b^2 + r^2)^{3/2}} \tag{B.1}$$

with I the current, r the assumed radius of the coil, N the number of windings and b the distance from a coil along its axis.

This gives the field strength at a specific point with a distance to one coil, where the point sits the axis at the center of the coil. Assuming the specific point being in the center of two equal coils the superposition of the magnetic fields can be computed as following:

$$H = \frac{Ir^2N}{((e/2)^2 + r^2)^{3/2}} \tag{B.2}$$

with e the distance between the coils.

In our case, to reach 20 Gauss, a peak current of 4.4 Ampere on 90 loops are necessary. When using a copper wire with 1.1 mm diameter this

results in an average current density of 2.84 A/mm^2. For 30 Gauss we obtain a peak current of 6.6 Ampere and an average density of 4.25 A/mm^2. Therefore, over a long timescale using a 20 Gauss rotating field does not overheat the coils. Over periods of a few minutes a 30 Gauss field is also harmless, according to the results of this model. After building the coils and calibrating them, the model with its assumptions got verified empirically.

To estimate the homogeneity of the magnetic field around the sample, here we used the *"Wolfram Matematica"* with the plugin *"SquareHelmholtz-Coils.cdf"*. This Software shows magnetic field distributions depending on the dimensions of the coils. Since our coils are rectangular but not square as assumed by the model, each of the two dimensions (coil-width and coil-height) of the X-field-coils and the Y-field coils have to be analyzed separately. The component in figure B.3a(right) represents the distribution of $B_y(z)$, while B_y is the Y-projection of the B-field vector. Figure B.3c(right) represents the distribution of $B_x(z)$, with B_x the X-projection of the B-field vector. The components fig.B.3c(left) and fig.B.3d(left) represent the distribution of $B_x(x)$, fig.B.3b(right) of $B_y(x)$. Finally, the components fig.B.3a(left) and fig.B.3b(left) represent the distribution of $B_y(y)$, fig.B.3d (right) of $B_x(y)$. For the case that more than one component is representing a distribution, a superimposition of the components represents it. This assumption may not be valid for analyzing the absolute value of the corresponding B-fields, but is well valid for the displaying homogeneity of the B-field distributions.

The analysis (figure B.3) shows that the field is around the center of the coils is a homogeneous field extending to roughly 10 cm away from the center. The extension of homogeneous fields is theoretically only necessary in the field of view, which is depending on the magnification of the objective, but is in any case less than 1 mm. Plenty of space around this area is homogeneous, which supports that also rest of the sample (typically a drop; not bigger than 5 mm in x and y) outside the field of view is exposed to the same homogeneous field, only. In the direction of the optical axis, the sample is typically is not thicker than 1 mm, but according to the geometry of the microscope the sample is not situated in the center of the z-direction, but 2.5 cm higher. Also there the field shows homogeneity. The only dimension that shows less homogeneous space is the width component of the Y-field coil (figure B.3 row b). Only right at the center ($\sim \pm 2$ cm) the magnetic field does not change significantly. Due to the geometry of the microscope the sample is situated exactly in the horizontal middle of these coils. Therefore,

the area in the field of view (less than 1 mm) centered in the coils can as well be considered as gradient-free.

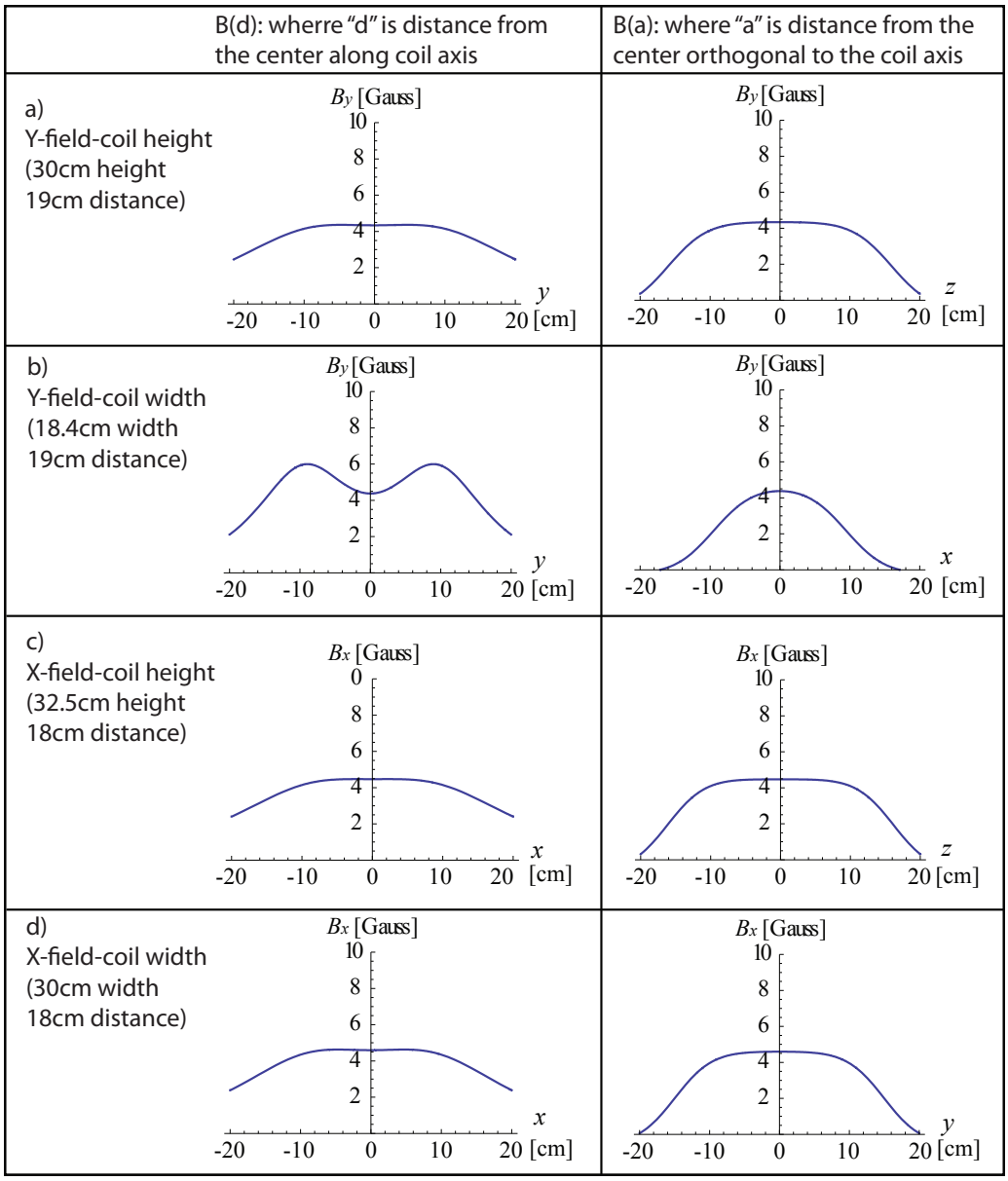

Figure B.3: *"Wolfram Mathematica"* B-field distributions of the coils. Since our coils are rectangular but not square, as assumed in this model, it is necessary to analyze the dimensions of the coils (coil-height and coil-width) separately. *B(d)* (left row) represents the B-field as a function of the distance d from the center, along the axis of the coils. *B(a)* (right column) represents the B-field as a function of the distance a from the center orthogonal to the coil axis. In the graphs the variables d and a are replaced by the coordinates x, y or z corresponding the orientation of each abscissa.

Figure B.4: Magnetoscope 3 with two pairs of Helmholtz coils

B.4 Conclusion:

The Magnetoscope 1 and 2 are a powerful tool, designed for the purpose of identifying magnetic objects in solutions. Even though we do not have a full control on the field strength nor a homogeneous field is generated, it is a simple mechanic device, easy to be adopted to inverse microscopes (inverse microscopes provide the space over the sample for this device). The relatively strong fields can re-magnetize the samples, or even destroy the internal structure e.g. magnetosome-chain-collapse. Further studies on these samples therefore may be biased, when testing for the magnetic moment or the internal structure of the objects. However, they still can be tested for different biological studies, such as for biological staining or also for DNA analysis.

The Magnetoscope 3 has the advantage of homogeneous fields, and of having the full control on the magnetic field strength as well as on the frequency. The 4-quadrant amplifiers and the waveform generators are expensive equipments, but they pay in having further experimental advantages: apart from identifying the objects under a rotating magnetic field, it is also possible to characterize the nature of magnetism in the objects. As described in chapter 2 the Magnetoscope is able to measure the magnetic moment of the objects. Measuring series of magnetic moments on an same object with different ambient magnetic field strengths it is possible to distinguish between induced or permanent magnetization. Driving only one pair of coils with a rectangular current (switching from positive to the same value in negative, and back) a U-turn-test can be performed. The U-turn test will flip all permanent magnetized objects, but will not rotate the induced magnetized objects.

References

Acosta-Avalos, D., Wajnberg, E., Oliveira, P. S., Leal, I., Farina, M., and Esquivel, D. M. S. (1999). Isolation of magnetic nanoparticles from *Pachycondyla marginata* ants. *J. Exp. Biol.*, **202**, 2687–2692. (document), 5.1

Acosta-Avalos, D., Esquivel, D. M. S., Wajnberg, E., Lins de Barros, H. G. P., Oliveira, P. S., and Leal, I. (2001). Seasonal patterns in the orientation system of the migratory ant *Pachycondyla marginata*. *Naturwissenschaften*, **88**, 343–346. (doi:10.1007/s001140100245). (document), 5.1

Adair, R. K. (2000). Static and low-frequency magnetic field effects: Health risks and therapies. *Rep. Prog. Phys.*, **63**, 415–454. 2.4

Adar, F. (1978). Resonance raman spectra of ferric cytochrome c. A probe of low-lying electronic levels of the iron ion. *J. Phys. Chem.*, **82**(2), 230–234. 3.5

Albert, J. S. and Crampton, W. G. R. (2005). Electroreception and electrogenesis. In D. Evans (ed.), *The Physiology of Fishes*, pp. 429–470. CRC, New York. 3rd Ed. 1.2, 2.2

Ashkin, A. (1997). Optical trapping and manipulation of neutral particles using lasers. *Proc. Natl. Acad. Sci. USA*, **94**(10), 4853–4860. A.2

Baudenbacher, F. J., Peters, N. T., and Wikswo, J. P. (2002). High resolution low-temperature superconductivity superconducting quantum interference device microscope for imaging magnetic fields of samples at room temperatures. *Rev. Sci. Instrum.*, **73**(3), 1247–1254. 5.4

Bazylinski, D. A., Schlezinger, D. R., Howes, B. H., Frankel, R. B., and Epstein, S. S. (2000). Occurrence and distribution

of diverse populations of magnetic protists in a chemically stratified coastal salt pond. *Chem. Geol.*, **169**(3–4), 319–328. (doi:10.1016/S0009-2541(00)00211-4). 3.2

Beason, R. C. and Semm, P. (1996). Does the avian ophthalmic nerve carry magnetic navigational information? *J. Exp. Biol.*, **199**, 1241–1244. 1

Begall, S., Cerveny, J., Neef, J., Vojtech, O., and Burda, H. (2008). Magnetic alignment in grazing and resting cattle and deer. *Proc. Natl. Acad. Sci. USA*, **105**, 13451–13455. (document), 1, 2.4

Bingman, V. P., Budzynski, C. A., and Voggenhuber, A. (2003). Migratory systems as adaptive responses to spatial and temporal variability in orientation stimuli. In P. Berthold, E. Gwinner, and E. Sonnenschein (eds.), *Avian Migration*, pp. 457–470. Springer, Berlin. 4.1

Boles, L. C. and Lohmann, K. J. (2003). True navigation and magnetic maps in spiny lobsters. *Nature*, **421**, 60–63. 1

Bourdoiseau, J.-A., Jeannin, M., Rémazeilles, C., Sabot, R., and Refait, P. (2011). The transformation of mackinawite into greigite studied by raman spectroscopy. *J. Raman Spectrosc.*, **42**, 496–504. doi: 10.1002/jrs.2729. 3.3

Brem, F., Hirt, A. M., Winklhofer, M., Frei, K., Yonekawa, Y., Wieser, H. G., and Dobson, J. (2006). Magnetic iron compounds in the human brain: a comparison of tumour and hippocampal tissue. *J. R. Soc. Interface*, **3**(11), 833–841. (doi: 10.1098/rsif.2006.0133). 3.2

Brown, H. and Ilyinsky, O. (1978). The ampullae of Lorenzini in the magnetic field. *J. Comp. Physiol.*, **126**, 333–341. 1, 1.2

Burda, H., Begall, S., Cerveny, J., Neef, J., and Němec, P. (2009). Extremely low-frequency electromagnetic fields disrupt magnetic alignment of ruminants. *Proc. Natl. Acad. Sci. USA*, **106**, 5708–5713. (document), 2.4

Cadiou, H. and McNaughton, P. A. (2010). Avian magnetite-based magnetoreception: a physiologist's perspective. *J. R. Soc. Interface*, **7**, S193–S205. (doi: 10.1098/rsif.2009.0423.focus). 1

Chang, L., Roberts, A. P., Muxworthy, A. R., Tang, Y., Chen, Q., Rowan, C. J., Liu, Q., and Pruner, P. (2007). Magnetic characteristics of synthetic pseudo-single-domain and multi-domain greigite (Fe_3S_4). *Geophys. Res. Lett.*, **34**, 1–6. (doi:10.1029/2007GL032114). 3.3

Chen, S. C., Kuo, P. C., Hsu, S. L., Lin, G. P., Ou, S. L., and Sun, T. H. (2009). Granular Co_3Pt thin films with perpendicular hard magnetic properties for perpendicular magnetic recording media. *IEEE Trans. Magn.*, **45**(5), 2280–2283. 3.4

Chew, G. L. and Brown, G. E. (1989). Orientation of rainbow trout (*Salmo gairdneri*) in normal and null magnetic fields. *Canad. J. Zool.*, **67**(3), 641–643. (http://spectrum.library.concordia.ca/6736/). 1.1

Cintolesi, F., Ritz, T., Kay, C. W. M., Timmel, C. R., and Hore, P. J. (2003). Anisotropic recombination of an immobilized photoinduced radical pair in a 50μT magnetic field: a model avian photomagnetoreceptor. *Chem. Phys.*, **294**(3), 385–399. (DOI: 10.1016/S0301-0104(03)00320-3). 1.2

Cochran, W. W., Mouritsen, H., and Wikelski, M. (2004). Migratory songbirds recalibrate their magnetic compass daily from twilight cues. *Science*, **304**, 405–408. 1.1, 4.1

Cornilsen, B. C. (1984). Solid state vibrational spectra of calcium pyrophosphate dihydrate. *J. Mol. Struct.*, **117**, 1–9. 3.4

Dahl, C. and Prange, A. (2006). Bacterial sulfur globules: Occurrence, structure and metabolism. In J. M. Shively (ed.), *Inclusions in Prokaryotes, Microbiology Monographs*, pp. 21–51. Springer, Berlin. (doi: 10.1007/3-540-33774-1-2). 3.2

Davila, A. F., Fleissner, G., Winklhofer, M., and Petersen, N. (2003). A new model for a magnetoreceptor in homing pigeons based on interacting clusters of superparamagnetic magnetite. *Phys. Chem. Earth*, **28**, 647–652. (doi:10.1016/S1474-7065(03)00118-9). 5.1

Davila, A. F., Winklhofer, M., Shcherbakov, V. P., and Petersen, N. (2005). Magnetic pulse affects a putative magnetoreceptor mechanism. *Biophys. J.*, **89**, 56–63. (doi:10.1529/biophysj.104.049346). 5.1

De Gelder, J., De Gussem, K., Vandenabeele, P., and Moens, L. (2007). Reference database of Raman spectra of biological molecules. *J. Raman Spectrosc.*, **38**, 1133–1147. 3.4

de Jager, H.-J. and Heyns, A. M. (1998). Kinetics of acid-catalyzed hydrolysis of a polyphosphate in water. *J. Phys. Chem. A*, **102**, 2838–2841. 3.4

Dennis, T. E., Rayner, M. J., and Walker, M. M. (2007). Evidence that pigeons orient to geomagnetic intensity during homing. *Proc. R. Soc. B.*, **274**(1614), 1153–1158. (doi: 10.1098/rspb.2007.3768). 1

Diebel, C. E., Proksch, R., Green, C. R., Neilson, P., and Walker, M. M. (2000). Magnetite defines a vertebrate magnetoreceptor. *Nature*, **406**, 299–302. (document), 1.3, 1, 2, 1.4, 2.2, 2.4, 3.2, 5.1

Docampo, R. (2006). Acidocalcisomes and polyphosphate granule. In J. M. Shively (ed.), *Inclusions in Prokaryotes*, pp. 53–70. Springer, Berlin. (doi: 10.1007/7171-003). 3.2, 3.4, 3.5

Eckert, B. and Steudel, R. (2003). Molecular spectra of sulfur molecules and solid sulfur allotropes. *Top. Curr. Chem.*, **231**, 31–98. 3.2, 3.4

Eder, S. H. K., Cadiou, H., Muhamad, A., McNaughton, P. A., Kirschvink, J. L., and Winklhofer, M. (2012). Magnetic characterization of isolated candidate vertebrate magnetoreceptor cells. *Proc. Natl. Acad. Sci. USA*, **109**(30), 12022–12027. (doi: 10.1073/pnas.1205653109). 3.2

Emlen, S. T. (1967). Migratory orientation in Indigo Bunting Passerina Cyanea .I. Evidence for use of celestial cues. *Auk*, **84**(3), 309–318. 4.1

Erglis, K., Wen, Q., Ose, V., Zeltins, A., Sharipo, A., Janmey, P. A., and Cēbers, A. (2007). Dynamics of magnetotactic bacteria in a rotating magnetic field. *Biophys. J.*, **93**(4), 1402–1412. 2.4, 2.7.1

Esquivel, D. M. S. and Lins de Barros, H. G. P. (1986). Motion of magnetotactic microorganisms. *J. Exp. Biol.*, **121**, 153–163. 2.4

Faivre, D. and Schüler, D. (2008). Magnetotactic bacteria and magnetosomes. *Chem. Rev.*, **108**, 4875–4898. 3.2

Faria, D. L. A. D. and Vena, S. (1997). Raman microspectroscopy of some iron oxides and oxyhydroxides. *J. Raman Spectrosc.*, **28**(4), 873–878. incompleta Journa l. 3.3

Farina, M., Esquivel, D. M. S., and De Barros, H. G. P. (1990). Magnetic iron-sulphur crystals from a magnetotactic microorganism. *Nature*, **343**, 256–258. (document), 3.2, 3.5

Ferreira, J., Cernicchiaro, G., Winklhofer, M., Dutra, H., Oliveira, P. S., Esquivel, D. M. S., and Wajnberg, E. (2005). Comparative magnetic measurements on social insects. *J. Magn. Magn. Mater.*, **289**, 442–444. (doi:10.1016/j.jmmm.2004.11.124). 5.1

Frank, C. J., McCreery, R. L., and Redd, D. C. (1995). Raman spectroscopy of normal and diseased human breast tissues. *Analyt. Chem.*, **67**, 777–783. 3.4

Frankel, R. B., Blakemore, R. P., and Wolfe, R. S. (1979). Magnetite in freshwater magnetotactic bacteria. *Science*, **203**, 1355–6. (document), 1, 1.4, 1.4, 2.4, 3.2

Friedmann, E. I., Wierzchos, J., Ascaso, C., and Winklhofer, M. (2001). Chains of magnetite crystals in the meteorite ALH84001: evidence of biological origin. *Proc. Natl. Acad. Sci. USA*, **98**, 2176–2181. 3.4

Gaber, B. P., Yager, P., and Peticolas, W. L. (1978). Deuterated phospholipids as nonperturbing components for Raman studies of biomembranes. *Biophys. J.*, **22**, 191–207. 3.4

Gaile, G. L. and Burt, J. E. (1980). *Directional Statistics*. Geo Abstracts. (ISBN: 0–86094–032–2). 4.3.3

Gegear, R. J., Foley, L. E., Casselman, A., and Reppert, S. M. (2010). Animal cryptochromes mediate magnetoreception by an unconventional photochemical mechanism. *Nature*, **463**, 804–807. 1

Gojzewski, H., Makowski, M., Hashim, A., Kopcanscy, P., Tomori, Z., and Timko, M. (2012). Magnetosomes on surface: An imaging study approach. *Scanning Vol*, **34**, 159–169. 5.1

Green, C. R., Holloway, H., and Walker, M. M. (2001). Detection of submicroscopic magnetite particles using reflectance mode confocal laser scanning microscopy. *Cell. Biol. Int.*, **25**, 985–990. 2.5

Hanesch, M. (2009). Raman spectroscopy of iron oxides and (oxy)hydroxides at low laser power and possible applications in environmental magnetic studies. *Geophys. J. Int.*, **177**, 941–948. 3.3

Hanzlik, M., Winklhofer, M., and Petersen, N. (1996). Spatial arrangement of chains of magnetosomes in magnetotactic bacteria. *Earth Planet. Sci. Lett.*, **145**, 125–134. 2.4, 3.2, 3.4, 3.5

Hanzlik, M., Heunemann, C., Holtkamp-Rötzler, E., Winklhofer, M., Petersen, N., and Fleissner, G. (2000). Superparamagnetic magnetite in the upper beak tissue of homing pigeons. *BioMetals*, **13**(4), 325–331. (doi:10.1023/A:1009214526685). 3.2

Hanzlik, M., Winklhofer, M., and Petersen, N. (2002). Pulsed-field-remanence measurements on individual magnetotactic bacteria. *J. Magn. Magn. Mater.*, **248**, 258–267. (document), 2.4, 3.2, 3.4

Harada, Y., Taniguchi, M., Namatame, H., and Iida, A. (2001). Magnetic materials in otoliths of bird and fish lagena and their function. *Acta Otolaryngol.*, **121**, 590–595. 2.4

Hart, V., Kušta, T., Němec, P., Bláhová, V., Ježek, M., Nováková, P., Begall, S., Červený, J., Hanzal, V., Malkemper, E. P., Štípek, K., Vole, C., and Burda, H. (2012). Magnetic alignment in carps: Evidence from the Czech Christmas fish market. *PLoS ONE*, **7**(12), e51100. (doi: 10.1371/journal.pone.0051100). 1

Hartmann, U., Göddenhenrich, T., and Heiden, C. (1991). Magnetic force microscopy: Current status and future trends. *J. Magnet. Magn. Mater.*, **101**, 263–270. 5.1

Hellinger, J. and Hoffmann, K. P. (2009). Magnetic field perception in the rainbow trout, *Oncorhynchus mykiss*. *J. Comp. Physiol. A*, **195**, 873–879. 1.1, 2.2

Hellinger, J. and Hoffmann, K. P. (2012). Magnetic field perception in the rainbow trout *Oncorynchus mykiss*: magnetite mediated, light dependent or both? *J Comp Physiol A*, **198**(8), 593–605. 1.1

Heyers, D., Zapka, M., Hoffmeister, M., Wild, J. M., and Mouritsen, M. (2010). Magnetic field changes activate the trigeminal brainstem complex in a migratory bird. *Proc. Natl. Acad. Sci. USA*,

107(20), 9394–9399. (doi: 10.1073/pnas.0907068107). (document), 1, 2.4

Himmel, D., Maurin, L. C., Gros, O., and Mansot, J.-L. (2009). Raman microspectrometry sulfur detection and characterization in the marine ectosymbiotic nematode *Eubostrichus dianae* (*Desmodoridae, Stilbonematidae*). *Biol. Cell*, **101**, 43–54. 3.2

Holland, R. A. ans Thorup, K., Vonhof, M. J., Cochran, W. W., and Wikelski, M. (2006). Bat orientation using Earth's magnetic field. *Nature*, **444**, 702. 4.1, 4.2.2, 4.2.3, 4.2.3, 4.2.5

Holland, R. A., Borissov, I., and Siemers, B. M. (2010). A nocturnal mammal, the greater mouse-eared bat calibrates a magnetic compass by the sun. *Proc. Natl. Acad. Sci. USA*, **107**, 6941–6945. (document), 4.1, 4.2.2, 4.2.3, 4.2.3, 4.2.3, 4.2.5, 4.2.5, 4.3.1, 4.5, 4.3.4, 4.4

Inoue, S. (2006). Foundations of confocal microscopy scanned imaging in light microscopy. In J. Pawley (ed.), *Handbook of Biological Confocal Microscopy*. Springer, New York. 3rd ed. A

Isambert, A. I., Menguy, N., Larquet, E. L., Guyot, F. G., and Valet, J.-P. V. (2007). Transmission electron microscopy study of magnetites in a freshwater population of magnetotactic bacteria. *Am. Mineral.*, **92**, 621–630. 3.2

Jeffrey, G. B. (1922). The motion of ellipsoidal particles immersed in a viscous fluid. *Proc. R. Soc. Lond. A*, **102**, 161–179. 2.7.2

Jogler, C., Niebler, M., Lin, W., Kube, M., Wanner, G., Kolinko, S., Stief, P., Beck, A. J., De Beer, D., Petersen, N., Pan, Y., Amann, R., Reinhardt, R., and Schüler, D. (2010). Cultivation-independent characterization of 'Candidatus Magnetobacterium bavaricum' via ultrastructural, geochemical, ecological and metagenomic methods. *Environ. Microbiol.*, **12**, 2466–2478. (doi: 10.1111/j.1462-2920.2010.02220.x). 3.2

Jogler, C., Wanner, G., Kolinko, S., Niebler, N., Amann, R., Petersen, N., Kube, M., Reinhardt, R., and Schüer, D. (2011). Conservation of proteobacterial magnetosome genes and structures in an uncultivated member of the deep-branching nitrospira phylum. *Proc. Natl.*

Acad. Sci. USA, **108**, 1134–1139. (doi: 10.1073/pnas.1012694108). 2.4, 3.2, 3.4

Kalmijn, A. J. (1981). Biophysics of geomagnetic field detection. *IEEE Trans. Magn.*, **17**, 1113–1124. 1, 1.2, 2.4

Keim, C. N., Martins, J. L., Abreu, F., Rosado, A. S., de Barros, H. L., Borojevic, R., Lins, U., and Farina, M. (2004). Multicellular life cycle of magnetotactic prokaryotes. *FEMS Microbiol. Lett.*, **240**, 203–208. (DOI:10.1016/j.femsle.2004.09.035). 2.3.1

Keim, C. N., Solorzano, G., Farina, M., and Lins, U. (2005). Intracellular inclusions of uncultured magnetotactic bacteria. *Int. Microbiol.*, **8**, 111–117. 3.2

Kirschvink, J. L. (1992a). Comment on constraints on biological effects of weak extremely-low-frequency electromagnetic fields. *Phys. Rev. A*, **46**, 2178–2186. 2.2, 2.4

Kirschvink, J. L. (1992b). Uniform magnetic fields and double-wrapped coil systems: Improved techniques for the design of bioelectromagnetic experiments. *Bioelectromagn.*, **13**(5), 401–411. (doi: 10.1002/bem.2250130507). (document), 1.2

Kirschvink, J. L. and Gould, J. L. (1981). Biogenic magnetite as a basis for magnetic field detection in animals. *BioSystems*, **13**, 181–201. 1, 2.2, 5.1

Kirschvink, J. L. and Hagadorn, J. W. (2000). A grand unified theory of biomineralization. In E. Bäuerlein (ed.), *The Biomineralisation of Nano- and Micro-Structures*, Chapter 10, pp. 139–150. Wiley-VCH Verlag GmbH, Weinheim, Germany. 1.4

Kirschvink, J. L. and Kobayashi-Kirschvink, A. (1991). Is geomagnetic sensitivity real? replication of the walker-bitterman magnetic conditioning experiment in honey bees. *Amer. Zool.*, **31**(1), 169–185. (doi: 10.1093/icb/31.1.169). 1.2

Kirschvink, J. L. and Lowenstam, H. A. (1979). Mineralization and magnetization of chiton teeth: Paleomagnetic, sedimentologic, and biological implications of organic magnetite. *Earth Planet. Sci. Lett.*, **44**, 193–204. 3.2

Kirschvink, J. L., Walker, M. M., Chang, S. B. R., Dizon, A. E., and Peterson, K. A. (1985a). Chains of single domain magnetite particles in the chinook salmon (*Oncorhynchus tshaytscha*). *J. Comp. Physiol. A*, **157**, 375–381. 2.3.3

Kirschvink, J. L., Jones, D. S., and MacFadden, B. J. (1985b). *Magnetite biomineralization and magnetoreception in organisms; a new biomagnetism*, Ausgabe 5 von *Topics in geobiology*. Plenum Publ., New York, NY, United States. 1

Kirschvink, J. L., Padmanabha, S., Boyce, C. K., and Oglesby, J. (1997). Measurement of the threshold sensitivity of honeybees to weak, extremely low frequency magnetic fields. *J. Exp. Biol.*, **200**, 1363–1368. 2.4

Kirschvink, J. L., Winklhofer, M., and Walker, M. M. (2010). Biophysics of magnetic orientation: Strengthening the interface between theory and experimental design. *J. R. Soc. Interface*, **7**(Suppl 2), S179–S191. 1.1, 1.3, 2.4

Kishkinev, D., Mouritsen, H., and Mora, C. (2012). An attempt to develop an operant conditioning paradigm to test for magnetic discrimination behavior in a migratory songbird. *J. Ornithol.*, **153**, 1165–1177. (doi: 10.1007/s10336-012-0847-x). 1.1

Komeili, A. (2012). Molecular mechanisms of compartmentalization and biomineralization in magnetotactic bacteria. *FEMS Microbiol. Rev.*, **36**, 232–255. 3.2

Kramer, G. (1953). Wird die Sonnenhöhe bei der Heimfinde Orientierung verwertet? *J. Ornithol.*, **94**, 201–219. (document), 4.1, 4.2.5

Lam, K. P., Hitchcock, A. P., Obst, M., Lawrence, J. R., Swerhone, G. D. W., Leppard, G. G., Tyliszczak, T., Karunakaran, C., Wang, J., Kaznatcheev, K., Bazylinski, D. A., and Lins, U. (2010). Characterizing magnetism of individual magnetosomes by X-ray magnetic circular dichroism in a scanning transmission X-ray microscope. *Chem. Geol.*, **270**, 110–116. 3.2, 5.4

Lee, A. P., Webb, J., Macey, D., Van Bronswijk, W., Savarese, A. R., and De Witt, G. C. (1998). In-situ Raman spectroscopic studies

of the teeth of the chiton *Acanthopleura hirtosa*. *J. Biol. Inorg. Chem.*, **3**(6), 614–619. (doi:10.1007/s007750050274). 3.2

Lefevre, C. T., Frankel, R. B., Abreu, F., Lins, U., and Bazylinski, D. A. (2011). Culture-independent characterization of a novel, uncultivated magnetotactic member of the Nitrospirae phylum. *Environ. Microbiol.*, **13**, 538–549. 3.2

Leonhardt, R. and Fabian, K. (2007). Paleomagnetic reconstruction of the global geomagnetic field evolution during the matuyama/brunhes transition: Iterative bayesian inversion and independent verification. *Earth Planet. Sci. Lett.*, **253**, 172–195. (doi: 10.1016/j.epsl.2006.10.025). 1

Li, J., Pan, Y., Liu, Q., Yu-Zhang, K., Menguy, N., Che, R., Qin, H., Wei Lin, W., Wu, W., Petersen, N., and Yang, X. (2010). Biomineralization, crystallography and magnetic properties of bullet-shaped magnetite magnetosomes in giant rod magnetotactic bacteria. *Earth Planet. Sci. Lett.*, **293**, 368–376. 3.2

Li, Y.-S., Church, J. S., and Woodhead, A. L. (2012). Infrared and Raman spectroscopic studies on iron oxide magnetic nano-particles and their surface modifications. *J. Magn. Magn. Mater.*, **324**, 1543–1550. 3.3

Lins, U. and Farina, M. (2004). Magnetosome chain arrangement and stability in magnetotactic cocci. *Antonie van Leeuwenhoek*, **85**, 335–341. 3.2

Lohmann, J. K., Putman, N. F., and Lohmann, C. M. (2008). Geomagnetic imprinting: a unifying hypothesis of long-distance migration natal homing in salmon and sea turtles. *Proc. Natl. Acad. Sci. USA*, **205**, 19096–19101. 2.4

Lohmann, K. J. (2010). Magnetic-field perception. *Nature*, **464**, 1140–1142. (document), 1, 2.2

Lowenstam, H. A. (1962). Magnetite in denticle capping in recent chitons (*Polyplacophora*). *Bull. Geol. Soc. Am.*, **73**, 435–438. (document), 1, 1.4, 1.4, 3.2

Lübbe, M., Gigler, A. M., Stark, R. W., and Moritz, W. (2010). Identification of iron oxide phases in thin films grown on $Al_2O_3(0001)$ by Raman spectroscopy and X-ray diffraction. *Surf. Sci.*, **604**, 679–685. 3.3

MacMillan, W. D. (1958). *The Theory of the Potential*, Chapter 37. Dover, New York. 2.7.2

Majed, N. and Gu, A. Z. (2010). Application of Raman microscopy for simultaneous and quantitative evaluation of multiple intracellular polymers dynamics functionally relevant to enhanced biological phosphorus removal processes. *Environ. Sci. Technol.*, **44**, 8601–8608. 3.4

Majed, N., Matthäus, C., Diem, M., and Gu, A. Z. (2009). Evaluation of intracellular polyphosphate dynamics in enhanced biological phosphorus removal process using Raman microscopy. *Environ. Sci. Technol.*, **43**, 5436–5342. 3.4

Mann, S. (2001). *Biomineralization: Principles and Concepts in Bioinorganic Materials Chemistry*. Oxford University Press. (ISBN-10: 0198508824). 1.4

Mann, S., Sparks, N. H. C., Walker, M. M., and Kirschvink, J. L. (1988). Ultrastructure, morphology and organization of biogenic magnetite from sockeye salmon, *Oncorhynchus nerka*: Implications for magnetoreception. *J. Exp. Biol.*, **140**, 35–49. 2.4

Mann, S., Sparks, N. H. C., Frankel, R. B., Bazylinski, D. A., and Jannasch, H. W. (1990). Biomineralization of ferrimagnetic greigite (Fe_3S_4) and iron pyrite (FeS_2) in a magnetotactic bacterium. *Nature*, **343**, 258–261. (document), 3.2, 3.5

Moore, A., Freake, S. M., and Thomas, I. M. (1990). Magnetic particles in the lateral line of the Atlantic salmon(*Salmo salar L.*). *Phil. Trans. R. Soc. Lond. B*, **329**, 11–15. 1.3, 2.3.3, 2.4

Mora, C. V., Davison, M., Wild, J. M., and Walker, M. M. (2004). Magnetoreception and its trigeminal mediation in the homing pigeon. *Nature*, **432**, 508–511. (doi:10.1038/nature03077). 1, 1.1

Mouritsen, H., Janssen-Bienhold, U., Liedvogel, M., Feenders, G., Stalleicken, J., Dirks, P., and Weiler, R. (2004). Cryptochromes and activity markers co-localize in bird retina during magnetic orientation. *Proc. Natl. Acad. Sci. USA*, **101**, 14294–14299. 1.2

Muheim, R., Moore, F. R., and Phillips, J. B. (2006a). Calibration of magnetic and celestial compass cues in migratory birds - a review of cue-conflict experiments. *J. Exp. Biol.*, **209**(1), 2–17. (document), 1.1, 4.1

Muheim, R., Phillips, J. B., and Akesson, S. (2006b). Polarized light cues underlie compass calibration in migratory songbirds. *Science*, **313**(5788), 837–839. 4.1, 4.2.2, 4.2.5, 4.4

Němec, P., Altmann, J., Marhold, S., Burda, H., and Oelschläger, H. H. A. (2001). Neuroanatomy of magnetoreception: The superior colliculus involved in magnetic orientation in a mammal. *Science*, **294**(5541), 366–368. (doi: 10.1126/science.1063351). 1, 1

Okabayashi, H., Yoshida, T., Ikeda, T., Matsuura, H., and Kitagawa, T. (1982). Metaphosphite (PO_2^-) symmetric-stretching raman line and molecular-aggregation states of barium dialkyl phosphates. *J. Am. Chem. Soc.*, **104**, 5399–5402. 3.4

Okada, M., Smith, N. I., Palonpon, A. F., Endo, H., Kawata, S., Sodeoka, M., and Fujita, K. (2012). Label-free raman observation of cytochrome c dynamics during apoptosis. *Proc. Natl. Acad. Sci. USA*, **109**(1), 28–32. 3.5

Oliveira, J. F., Wajnberg, E., de Souza Esquivel, D. M., Weinkauf, S., Winklhofer, M., and Hanzlik, M. (2010). Ant antennae: are they sites for magnetoreception? *J. R. Soc. Interface*, **7**(42), 143–152. (doi:10.1098/rsif.2009.0102). (document), 1.3, 5.1, 5.1, 5.4

Osborn, J. A. (1945). Demagnetizing factors of the general ellipsoid. *Phys. Rev.*, **67**, 351–357. 2.7.2

Pan, Y., Petersen, N., Davila, A., and Zhang, L. (2005). The detection of bacterial magnetite in recent sediments of lake Chiemsee (southern Germany). *Earth Planet. Sci. Lett.*, **232**, 109–123. 3.2

Pan, Y., Lin, W., Li, J., Wu, W., Tian, L., Deng, C., Liu, Q., Zhu, R., Winklhofer, M., and Petersen, N. (2010). Reduced efficiency of magnetotaxis in magnetotactic coccoid bacteria in higher than geomagnetic fields. *Biophys. J.*, **97**, 986–991. 2.4

Papi, F. (1992). *Animal Homing*. Chapman and Hall, London. 4.1

Pasteris, J., Freeman, J. J., Goffredi, S. K., and Buck, K. R. (2001). Raman spectroscopic and laser scanning confocal microscopic analysis of sulfur in living sulfur-precipitating marine bacteria. *Chem. Geol.*, **180**, 3–18. 3.2, 3.3, 3.4

Paulin, M. G. (1995). Electroreception and the compass sense of sharks. *J. Theor. Biol.*, **174**, 325–339. 2.2

Peters, R. C., Eeuwes, L., and Bretschneider, F. (2007). On the electrodetection threshold of aquatic vertebrates with ampullary or mucous gland electroreceptor organs. *Biol. Rev.*, **82**(361-73). 2.2

Petersen, N., Weiss, D. G., and Vali, H. (1992). Magnetic bacteria in lake sediments. In F. Lowes, D. W. Collinson, J. Parry, S. Runcorn, D. Tozer, and A. Soward (eds.), *Geomagnetism and Paleomagnetism*, pp. 231–241. Kluwer. ISBN: 079230084X. B

Phillips, J. B. and Borland, S. C. (1992). Behavioral evidence for the use of a light-dependent magnetoreception mechanism by a vertebrate. *Nature*, **359**, 142–144. 1, 1.1

Phillips, J. B. and Waldvogel, J. A. (1982). Reflected light cues generate the short-term deflector loft effect. In F. Papi and H. G. Wallraff (eds.), *Avian navigation*, pp. 190–202. Springer, Berlin. 4.1, 4.2.5

Pickering, I. J., George, G. N., Yu, E. Y., Brune, D. C., Tuschak, C., Overmann, J., Beatty, J. T., and Prince, R. C. (2001). Analysis of sulfur biochemistry of sulfur bacteria using X-ray absorption spectroscopy. *Biochem.*, **40**(27), 8138–8145. (doi: 10.1021/bi0105532). 3.2

Posfai, M., Buseck, P. R., Bazylinski, D. A., and Frankel, R. B. (1998). Iron sulfides from magnetotactic bacteria; structure, composition, and phase transitions. *Am. Mineral.*, **83**, 1469–1481. (document), 3.2

Prange, A., Chauvistre, R., Modrow, H., Hormes, J., Trueper, H. G., and Dahl, C. (2002). Quantitative speciation of sulfur in bacterial sulfur globules: X-ray absorption spectroscopy reveals at least three different species of sulfur. *Microbiol.*, **148**(1), 267–276. 3.2, 3.4

Preston, C. M. and Adams, W. A. (1979). A laser Raman spectroscopic study of aqueous orthophosphate salts. *J. Phys. Chem.*, **83**(7), 814–821. doi: 10.1021/j100470a011. 3.4

Proksch, R. B., Moskowitz, B. M., Dahlberg, E. D., Schaeffer, T., Bazylinski, D. A., and Frankel, R. B. (1995). Magnetic force microscopy of the submicron magnetic assembly in a magnetotactic bacterium. *Appl. Phys. Lett.*, **66**, 2582–2584. 3.2, 5.1

Quinn, T. P. (1980). Evidence for celestial and magnetic compass orientation in lake migrating sockeye salmon fry. *J. Comp. Physiol. A*, **137**, 243–248. 1.1, 2.2

Quinn, T. P. and Brannon, E. L. (1982). The use of celestial and magnetic cues by orienting sockeye salmon smolts. *J. Comp. Physiol. A*, **147**, 547–552. 1.1, 4.3.4

Quintana, C., Cowley, J. M., and Marhic, C. (2004). Electron nanodiffraction and high-resolution electron microscopy studies of the structure and composition of physiological and pathological ferritin. *J. Struct. Biol.*, **147**, 166–178. 3.2

Ritz, T., Adem, S., and Schulten, K. (2000). A model for photoreceptor-based magnetoreception in birds. *Biophys. J.*, **78**, 707–718. 1.2

Ritz, T., Thalau, P., Phillips, J., Wiltschko, R., and Wiltschko, W. (2004). Resonance effects indicate a radical-pair mechanism for avian magnetic compass. *Nature*, **429**, 177–180. (doi:10.1038/nature02534). 1.2, 4.3.2

Ritz, T., Wiltschko, R., Hore, P. J., Rodgers, C. T., Stapput, K., Thalau, P., Timmel, C. R., and Wiltschko, W. (2009). Magnetic compass of birds is based on a molecule with optimal directional sensitivity. *Biophys. J.*, **96**, 3451–3457. (doi:10.1016/j.bpj.2008.11.072). (document), 1.2, 4.3.2

Ritz, T., Ahmad, M., Mouritsen, H., Wiltschko, R., and Wiltschko, W. (2010). Photoreceptor-based magnetoreception: Optimal design of receptor molecules, cells, and neuronal processing. *J. R. Soc. Interface*, **7**(Suppl 2), S135–146. 1.2, 2.2

Rodgers, C. T. and Hore, P. J. (2009). Chemical magnetoreception in birds: The radical pair mechanism. *Proc. Natl. Acad. Sci. USA*, **106**, 353–360. 1.2, 2.2

Sandberg, R., Backman, J., Moore, F. R., and Lohmus, M. (2000). Magnetic information calibrates celestial cues during migration. *Anim. Behav.*, **60**, 907–907. (ISBN-10: 3-540-43408-9). 4.1

Sandeman, D. C. (1976). *Structure and function of proprioceptors in the invertebrates*. Chapman and Hall, London, UK. (ISBN-10: 041212890X). 1.3, 5.1

Schachtschneider, J. H. and Snyder, R. G. (1963). Vibrational analysis of the n-paraffines - ii. Normal co-ordinate calculations. *Spectrochim. Acta A*, **19**, 117–168. 3.4

Schulten, K., Swenberg, C. W., and Weller, A. (1978). A biomagnetic sensory mechanism based on magnetic field modulated coherent electron spin motion. *Z. Phys. Chem. NF*, **111**, 1–5. (document), 1, 1.2, 2.2

Scott, D. W., McCullough, J., and Kruse, F. (1964). Vibrational assignment and force constants of S_8 from a normal-coordinate treatment. *J. Mol. Spectrosc.*, **13**, 313–320. 3.4

Shcherbakov, D., Winklhofer, M., Petersen, N., Steidle, J., Hilbig, R., and Blum, M. (2005). Magnetosensation in zebrafish. *Curr. Biol.*, **15**, 161–162. 1.1, 2.2

Shcherbakov, V. P. and Winklhofer, M. (1999). The osmotic magnetometer: a new model for magnetite-based magnetoreceptors in animals. *Eur. Biophys. J.*, **28**, 380–392. (doi:10.1007/s002490050222). 5.1

Shcherbakov, V. P. and Winklhofer, M. (2004). Bending of magnetic filaments under a magnetic field. *Phys. Rev. E*, **70**(6), 061803–1–9. (10.1103/PhysRevE.70.061803). 2.7.5

Shcherbakov, V. P., Winklhofer, M., Hanzlik, M., and Petersen, N. (1997). Elastic stability of chains of magnetosomes in magnetic bacteria. *Eur. Biophys. J.*, **26**, 319–326. 2.4

Shebanova, O. N. and Lazor, P. (2003a). Raman spectroscopic study of magnetite (Fe_3O_4): a new assignment for the vibrational spectrum. *J. Sol. State Chem.*, **174**, 424–430. 3.3, 3.4

Shebanova, O. N. and Lazor, P. (2003b). Raman study of magnetite (Fe_3O_4): laser-induced thermal effects and oxidation. *J. Raman Spectrosc.*, **34**, 845–852. 1.4, 3.3, 3.5

Spiro, T. G. and Streaks, T. C. (1972). Resonance Raman spectra of hemoglobin and cytochrome c: Inverse polarization and vibronic scattering. *Proc. Nat. Acad. Sci. USA*, **69**(9), 2622–2626. 3.5, A.1

Spring, S., Amann, R., Ludwig, W., Schleifer, K. H., van Gemerden, H., and Petersen, N. (1993). Dominating role of an unusual magnetotactic bacterium in the microaerobic zone of a freshwater sediment. *Appl. Env. Microbiol.*, **59**, 2397–403. (document), 3.2, 3.5

Steinberger, B., Petersen, N., Petermann, H., and Weiss, D. (1994). Movement of magnetic bacteria in time-varying magnetic fields. *J. Fluid Mech.*, **213**, 189–211. 2.4, 2.5

Stoner, E. C. (1945). The demagnetizing factors for ellipsoids. *Phil. Mag. Ser. 7*, **36**(263), 803–821. 2.7.2

Stoner, E. C. and Wohlfarth, E. P. (1948). A mechanism of magnetic hysteresis in heterogeneous alloys. *Proc. R. Soc. Lond. A*, **240**, 599–642. 2.7.5

Suthers, R. A. (1970). Vision, olfaction, taste. In W. A. Wimsatt (ed.), *Biology of Bats*, pp. 265–304. Acad. Prass, New York. 4.4

Suzuki, H., Tanaka, T., Sasaki, T., Nakamura, N., Matsunaga, T., and Mashiko, S. (1998). High-resolution magnetic force microscope images of a magnetic particle chain extracted from magnetic bacteria AMB-1. *Jap. J. Appl. Phys.*, **37**, 1343–1345. 3.2, 5.1

Takebe, A., Furutani, T., Wada, T., Koinuma, M., Kubo, Y., Okano, K., and Okano, T. (2012). Zebrafish respond to the geomagnetic field by bimodal and group-dependent orientation. *Sci. Rep.*, **2**(727). (doi: 10.1038/srep00727). 1.1

Tarduno, J. A., Cottrell, R. D., Watkeys, M. K., Hofmann, A., Doubrovine, P. V., Mamajek, E. E., Liu, D., Sibeck, D. G., Neukirch, L. P., and Usui, Y. (2010). Geodynamo, solar wind, and magnetopause 3.4 to 3.45 billion years ago. *Science*, **327**(5970), 1238–1240. (doi: 10.1126/science.1183445). (document), 1

Taylor, P. B. (1986). Experimental evidence for geomagnetic orientation in juvenile salmon, *Oncorhynchus tschawytscha Walbaum*. *J. Fish Biol.*, **28**, 607–623. 1.1, 2.2

Thalau, P., Ritz, T., Stapput, K., Wiltschko, R., and Wiltschko, W. (2005). Magnetic compass orientation of migratory birds in the presence of a 1.315 MHz oscillating field. *Naturwissenschaften*, **92**, 86–90. (DOI 10.1007/s00114-004-0595-8). 1.2, 4.3.2

Thalau, P., Ritz, T., Burda, H., Wegner, R., and Wiltschko, R. (2006). The magnetic compass mechanisms of birds and rodents are based on different physical principles. *J. R. Soc. Interface*, **3**, 583–587. 1.2, 4.3.2

Torres de Araujo, F. F., Pires, M. A., Frankel, R. B., and Bicudo, C. E. (1986). Magnetite and magnetotaxis in algae. *Biophys. J.*, **50**, 376–378. 3.2

Treiber, C. D., Salzer, M. C., Riegler, J., Edelman, N., Sugar, C., Breuss, M., Pichler, P., Cadiou, H., Saunders, M., Lythgoe, M., Shaw, J., and Keays, D. A. (2012). Clusters of iron-rich cells in the upper beak of pigeons are macrophages and not magnetosensitive neurons. *Nature*, **484**, 367–371. 2.4

Vali, H., Förster, O., Amarantidis, G., and Petersen, N. (1987). Magnetotactic bacteria and their magnetofossils in sediments. *Earth Planet. Sci. Lett.*, **86**, 389–400. 3.2

Vanderstraeten, J. and Gillis, P. (2010). Theoretical evaluation of magnetoreception of power-frequency fields. *Bioelectromagnetics*, **31**, 371–379. 2.4

Wajnberg, E., Acosta-Avalos, D., El-Jaick, L. J., Abracado, L., Coelho, J. L. A., Bazukis, A. F., Morais, P. C., and Esquivel, D. M. S. (2000). Electron paramagnetic resonance study of the migratory ant *Pachycondyla marginata* abdomens. *Biophys. J.*, **78**, 1018–1023. (doi:10.1016/S0006-3495(00)76660-4). (document), 5.1

Wajnberg, E., Cernicchiaro, G. R., and Esquivel, D. M. S. (2004). Antennae: the strongest magnetic part of the migratory ant. *Biometals*, **17**, 467–470. (doi:10.1023/B:BIOM.0000029443.93732.62). (document), 5.1

Walcott, C., Gould, J., and Kirschvink, J. L. (1979). Pigeons have magnets. *Science*, **205**, 1027–1029. 1.4, 3.2

Walker, M. M. (1984). Learned magnetic field discrimination in the yellowfin tuna, *Thunnus albacares*. *J. Comp. Physiol. A*, pp. 673–679. 1.1

Walker, M. M. and Bittermann, M. E. (1989). Attached magnets impair magnetic field discrimination in honeybees. *J. Exp. Biol.*, **141**, 447–451. 1.2

Walker, M. M., Kirschvink, J. L., Chang, S. B., and Dizon, A. E. (1984). A candidate magnetic sense organ in the yellowfin tuna, *Thunnus albacares*. *Science*, **224**, 751–753. 1, 2.2, 3.2

Walker, M. M., Quinn, T. P., Kirschvink, J. L., and Groot, C. (1988). Production of single-domain magnetite throughout life by sockeye salmon, *Oncorhynchus nerka*. *J. Exp. Biol.*, **140**, 51–63. 2.3.3, 2.4

Walker, M. M., Diebel, C. E., Haugh, C. V., Pankhurst, P. M., Montgomery, J. C., and Green, C. R. (1997). Structure and function of the vertebrate magnetic sense. *Nature*, **390**, 371–376. (document), 1, 1.1, 1.3, 1.2, 1.3, 1, 1.4, 2.2, 2.4, 2.5, 3.2, A

Walker, M. M., Dennis, T. E., and Kirschvink, J. L. (2002). The magnetic sense and its use in long-distance navigation by animals. *Current Opinion in Neurobiology*, **12**, 735–744. (document), 1.2, 1.4

Watanabe, S., Yamanaka, M., Sakai, A., Sawada, K., and Iwasa, T. (2009). Laser raman spectroscopic study of magnetite formation in magnetotactic bacteria. *J. Japan Inst. Metals*, **73**, 334–339. 3.2

Wenger, R. E., Begall, S., and Burda, H. (2006). Magnetic compass in the cornea: Local anesthesia impairs orientation in mammal. *J Exp Biol*, **209**, 4747–4750. (doi:10.1242/jeb.02573). 2.4

Williams, A. and Edwards, H. (1994). Raman spectra of human keratotic biopolymers: skin, callus, hair and nail. *J. Raman Spectrosc.*, **25**, 95–98. 3.4

Wiltschko, R. and Wiltschko, W. (1995). *Magnetic Orientation in animal*. Springer, Berlin, Germany. 1

Wiltschko, R. and Wiltschko, W. (2006). Magnetoreception. *Bio Essays*, **28**, 157–168. 4.1

Wiltschko, W. and Wiltschko, R. (1972). Magnetic compass of european robins. *Science*, **176**, 62–64. 1, 1, 1.1, 4.1, 4.3.4

Wiltschko, W. and Wiltschko, R. (1975). The interaction of stars and magnetic field in the orientation system of night migrating birds. i. autumn experiments with european warblers (*Gen. Sylvia*). *Z. Tierpsychol*, **37**(4), 337–355. 4.1

Wiltschko, W. and Wiltschko, R. (2005). Magnetic orientation and magnetoreception in birds and other animals. *Journal of Comparative Physiology A*, **191**, 675–693. 1, 2.2

Winklhofer, M. (2010). Magnetoreception. *J. R. Soc. Interface*, **7**, 131–134. (doi: 10.1098/rsif.2010.0010.focus). 1.1

Winklhofer, M. and Kirschvink, J. L. (2010). A quantitative assessment of torque-transducer models for magnetoreception. *J. R. Soc. Interface*, **7**(Suppl 2), S273–289. 1.3, 2.2, 2.4, 5.4

Winklhofer, M., Abracado, L. G., Davila, A. F., Keim, C. N., and Lins de Barros, H. G. P. (2007). Magnetic optimization in a multicellular magnetotactic organism. *Biophys. J.*, **92**, 661–670. 2.4

Woell, S., Windoffer, R., and Leube, R. E. (2005). Dissection of keratin dynamics: Different contributions of the actin and microtubule systems. *Eur. J. Cell. Biol.*, **84**, 311–328. 2.5

Wu, L. Q. and Dickman, J. D. (2011). Magnetoreception in an avian brain in part mediated by inner ear lagena. *Curr. Biol.*, **21**(5), 418–423. 1, 1.3, 2.4

Wu, L. Q. and Dickman, J. D. (2012). Neural correlates of a magnetic sense. *Science*, **336**, 1054–1057. 1, 1.3, 2.4

Zapka, M., Heyers, D., Hein, C. M., Engels, S., Schneider, N.-L., Hans, J., Weiler, S., Dreyer, D., Kishkinev, D., Wild, J. M., and Mouritsen, H. (2009). Visual but not trigeminal mediation of magnetic compass information in a migratory birds. *Nature*, **461**, 1274–1277. (doi:10.1038/nature08528). 1

Acknowledgments

An dieser Stelle möchte ich mich bei allen bedanken, die mir bei der Erstellung dieser Doktorarbeit geholfen haben.

In allererster Linie gehört mein besonderer Dank PD Dr. Michael Winklhofer für seine Unterstützung und Betreuung. Erst durch ihn bin ich auf dieses spannende Feld der Wissenschaft gestoßen. Mit seinem wertvollen Wissen konnte er meinen Horizont in mannigfaltige Richtungen erweitern. Die vielen wissenschaftlichen Diskussionen mit ihm waren Quell zahlreicher Ideen. Ohne ihn wäre eine Arbeit in dieser Form nicht möglich gewesen.

Auch danke ich Prof. Hervé Cadiou, der mir die Techniken und Grundlagen der Biologie nicht nur mit enormer Kompetenz, sondern auch mit viel Witz und Humor näher brachte.

Des weiteren danke ich Prof. Guntram Jordan, Dr. Alexander Gigler und Dr. Marianne Hanzlik für ihre Zeit und Mühe mit der wir gemeinsam meine Proben analysierten (MFM, Raman- und Elektronenmikroskopie).

Prof. Gil Westmeyer möchte herzlich dafür danken, dass er mich in den letzten Zügen der Erstellung dieser Arbeit mit Rat und Tat unterstützt hat.

Auch bedanke ich mich bei Prof. Nikolai Petersen für seine unvoreingenommenen und hilfreichen Einschätzungen und Anregungen.

Prof. Joe Kirschvink danke ich für seine positiven Impulse, mit denen er zu internationaler Zusammenarbeit anregte, und für seine Gastfreundschaft während meines Aufenthalts am CalTech Pasedena.

Ich danke Dr. Richard Holland und PD Dr. Björn Siemers, dass sie mich bei den spannenden Feldversuchen an Fledermäusen einbezogen haben. An dieser Stelle möchte ich Björn Siemers gedenken, der leider im Mai 2012 verstarb. Er bereicherte mich durch sein Wissen und seine Freundschaft.

Ich danke auch für die finanzielle Unterstützung durch Human Frontier Science Org. (HFSP Grant RGP 28/2007).

Schließlich möchte ich mich noch bei meiner Familie bedanken, die mich während dieser Arbeit stets unterstützte. Besonderer Dank gebührt hierbei meiner lieben Bibi für ihre Geduld und liebevolle Unterstützung.